Spectroscopy of Binuclear Dioxygen Complexes

Edward I. Solomon,* Felix Tuczek,† David E. Root, and Carl A. Brown

Department of Chemistry, Stanford University, Stanford, California 94305

Received September 14, 1993 (Revised Manuscript Received January 17, 1994)

Contents

I. Introduction

Spectroscopic studies have been performed on a wide range of metal–dioxygen complexes particularly those containing porphyrin ligands.[1,2] This review focuses on three classes of non-heme dioxygen–metal complexes in which peroxide is bound to binuclear Cu(II), Co(III), and Fe(III) sites. Along with hemoglobin and myoglobin, hemocyanin and hemerythrin comprise the known biological dioxygen-binding proteins. In contrast to hemoglobin and myoglobin, the charge-transfer regions of the absorption spectra of hemocyanin and hemerythrin, which will be the central focus of this review, are not obscured by intense porphyrin-based electronic transitions, allowing detailed spectral study. Deoxyhemocyanin has a binuclear cuprous active site that reversibly binds dioxygen as peroxide[3] as determined from the O–O stretching frequency in the resonance Raman spectrum.[4–6] The two coppers are oxidized to the cupric level upon binding O_2, as confirmed by X-ray absorption edge data.[7–9] The crystal structure of oxyhemocyanin from *Limulus polyphemus* has recently been solved,[10] (Figure 1A) and, along with a binuclear cupric model complex,[11] exhibits the first side-on (or μ-η^2:η^2) peroxo-bridging geometry observed in transition metal chemistry. An important goal in the study of this site has been to understand how the electronic structure of the side-on peroxo-bridged structure relates to that of end-on peroxo-bridged systems which are more commonly observed in transition metal chemistry. Deoxyhemerythrin has a binuclear ferrous site which is known to bind dioxygen as hydroperoxide[12] on the basis of resonance Raman data.[13] Both iron ions are oxidized to the ferric level and, as determined by both spectroscopy[14] and crystallography,[15] are connected by an oxo bridge. The Fe^{III}–O–Fe^{III} unit exhibits distinctive spectral features[16,17] indicating a novel electronic structure associated with the oxo bridge which can strongly influence the properties of this site and its interaction with dioxygen. The hydroperoxide binds end-on to one iron[15,18] and appears to hydrogen bond to the oxo bridge (Figure 1B).[13] Although there are no binuclear cobalt sites of direct biological relevance, two Co(II) ions have been substituted into the apo (i.e., metal free) sites in both hemocyanin[19] and hemerythrin,[20] and the former appears to bind O_2 at high pH resulting in a peroxo–Co^{III}_2 complex. Of further general interest is the variety of peroxo bridging geometries observed for binuclear Co(III) complexes,[21] in particular the *trans-* and *cis-*μ-1,2 end-on structures on Figure 1, parts C and D. These complexes provide a model for understanding how the electronic structure changes with differences in peroxo bridging mode and how this affects the O_2 reactivity of the complex.

All the complexes in Figure 1 exhibit distinctive spectral features compared to their non-peroxide bound, two electron oxidized (i.e., met) site analogues. Their ground states show no EPR signal or paramagnetic susceptibility due to either antiferromagnetic coupling (*vide infra*) or, for Co(III), the low spin d^6 configuration of the complex. Their electronic absorption spectra, however, show intense features which are *peroxide → metal charge-transfer transitions which provide a sensitive probe of the peroxo–metal bond.*[2,22] Peroxide has a doubly degenerate π^* set of valence orbitals which are involved in bonding to the metal. The energies and intensities of the charge-transfer transitions from these valence orbitals to the metal center define the peroxide σ and π bonding interactions as described below. For the sites of Figure 1, the peroxide → metal charge transfer transitions are at low energy (i.e., in the UV/visible region) and are intense. This indicates that these sites are highly covalent and that the electronic structure of the peroxo–metal bond greatly contributes to the binding and activation of dioxygen by these sites.

The major focus of this review is to develop an understanding of the peroxide → metal charge-transfer transitions in the complexes in Figure 1 and related systems. The CT absorption spectrum, including its temperature dependence, and the polarizations of bands in single crystals, combined with circular dichroism (CD), magnetic CD (MCD), and resonance Raman excitation profiles provide complementary probes of these transitions and experimentally define electronic structure. These spectral studies are correlated to broken symmetry–self-consistent field–Xα–scattered wave (BS-SCF-Xα-SW) calculations describing the bonding in these complexes. These calculations[23,24]

† Present address: Anorganische Chemie, Universität Mainz, 55099 Mainz Germany.

0009-2665/94/0794-0827$14.00/0 © 1994 American Chemical Society

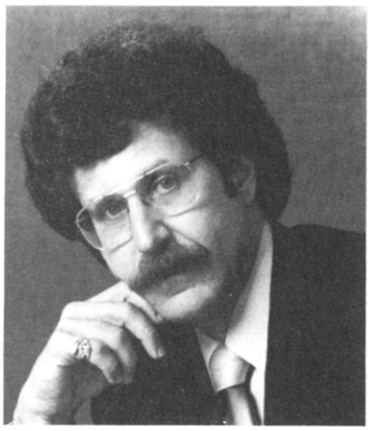

Edward I. Solomon is presently the Monroe E. Spaght Professor of Chemistry at Stanford University where he has been since 1982 and was previously a Professor at the Massachusetts Institute of Technology. Professor Solomon received his Ph.D. for research directed by Professor Donald S. McClure at Princeton University and then was a postdoctoral fellow working first with Professor C. J. Ballhausen at the H. C. Ørsted Institute at the University of Copenhagen and then with Professor Harry Gray at the California Institute of Technology. He is an associate editor of Inorganic Chemistry and a member of the editorial board of *Chemical Reviews*, *Inorganic Biochemistry*, and *Chemtracts*; he has been the first Glen Seaborg, Taiwan National Science Council, Xerox, O. K. Rice, Reilly, Frontiers, and World Bank lecturer and an Invited Professor at the University of Paris, Xiamen University, China, La Plata University, Argentina, and Tokyo Institute of Technology. He received the 1990 Deans Award for Distinguished Teaching at Stanford. His research interests include physical-inorganic chemistry, bioinorganic chemistry, and surface science with emphasis on the detailed spectroscopic study of transition metal ion electronic structure.

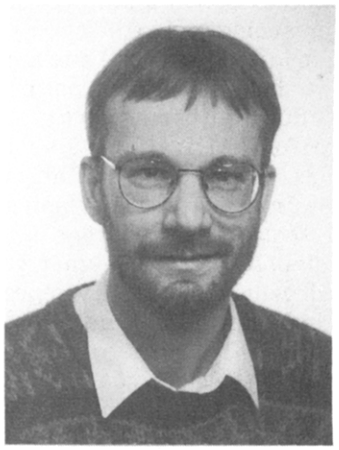

Felix Tuczek was born in Marburg/Lahn, Germany, in 1958. He was a student at Johannes Gutenberg Universität Mainz and got his Diploma in Chemistry in 1984. In 1989, he got his Ph.D. with Prof. P. Gütlich at the Department of Inorganic Chemistry at Mainz. As a DFG postdoctoral fellow, he worked from 1989 to 1991 with Prof. Ed Solomon at Stanford University. In 1991, he returned to Mainz and since then has been working on his habilitation. His research activities are in the field of physical inorganic and bioinorganic chemistry and include Mössbauer spectroscopy (also in emission) on simple inorganic systems as well as spectroscopic (UV–vis, Raman, Mössbauer) and theoretical studies on the electronic structure of transition metal dimers of biological interest. His current interests are centered around small molecule activation by transition metal complexes.

allow for localization of the unpaired electrons on each metal in the dimer, as is appropriate for antiferromagnetically coupled binuclear Cu(II) and Fe(III) systems. Together these experiments and calculations define the electronic structure of the sites in Figure 1 and evaluate electronic structure contributions to reversible O_2 binding and activation.

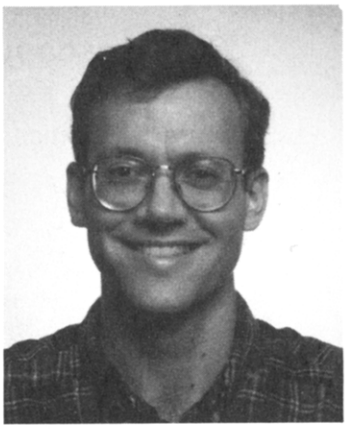

Carl A. Brown was born in Greenwood, SC, in 1966. He received his B.S. in Chemistry from Furman University in 1988 and did undergraduate research under the direction of Dr. Jane Joseph. He is currently working toward the completion of his Ph.D. requirements in the research group of Professor Edward I. Solomon. His current research interests are the spectroscopy and electronic structure of non-heme iron enzymes.

David E. Root was born in Lewisburg, PA, in 1967. He received his B.A. in Chemistry from Swarthmore College in 1990 where he did research with Professor Thomas Stephenson. He is now a Ph.D. candidate in the research group of Professor Edward I. Solomon. His research interests include the spectroscopy of copper complexes and proteins which bind and activate dioxygen.

In section II we focus on Cu(II) complexes with end-on and side-on bound peroxide where only the highest energy half-occupied d orbital is available for bonding. In these systems, the peroxide bridges the two Cu(II) ions leading to antiferromagnetic coupling in the ground state, which can be described by the phenomenological Hamiltonion, $H = -2J\mathbf{S}_1\cdot\mathbf{S}_2$. It is important to emphasize that the excited-state spectral features can also show energy splittings due to antiferromagnetic coupling through a bridging ligand.[25] This is addressed in section III. The excited-state dimer splitting complicates the analysis of the absorption spectrum, but once understood, provides significant insight into the interactions between the metal centers due to the bridging ligand. In section IV, this monomer → dimer analysis is applied to the absorption spectrum of oxyhemocyanin. The assignment of the oxyhemocyanin O_2^{2-} → Cu(II) charge-transfer spectrum supports the electronic structure description of the side-on bridged structure of this site (Figure 1A) developed in section II and provides insight into the electronic structure contribution to the reversible binding and activation of dioxygen. The peroxide–binuclear Co(III) complexes in Figure 1, parts C and D, are considered in section V. Polarized single-

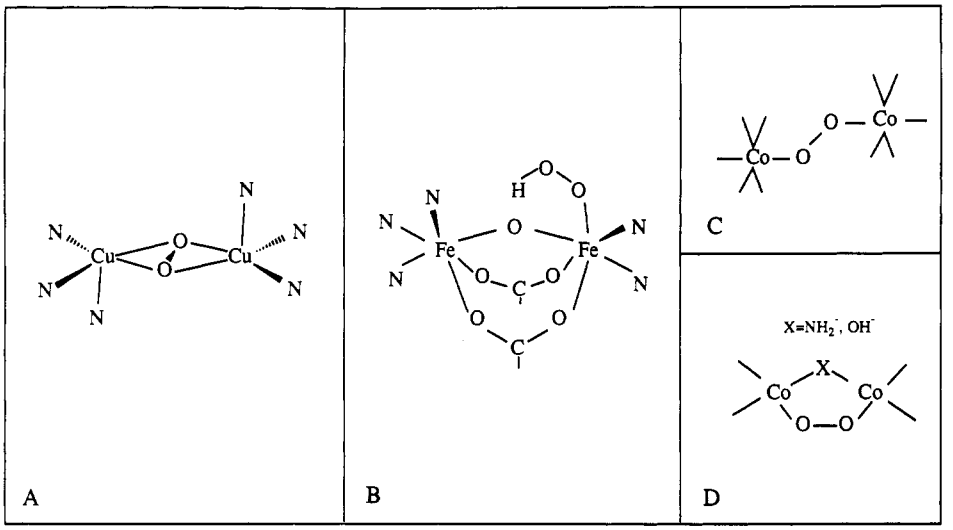

Figure 1. (A) Structure of oxyHc, (B) structure of oxyHr, (C) typical geometry of *trans*-peroxo–Co dimers, and (D) typical geometry of *cis*-peroxo–Co dimers.

crystal data have provided an assignment of the charge transfer features of the *trans*-μ-1,2 structure and indicate the presence of an inverted bonding scheme relative to most peroxo–metal complexes.[26] These studies are extended to the *cis*-μ-1,2-peroxide-bridged binuclear Co(III) complex and contrasted to the end-on peroxide-bridged copper dimers. In section VI we consider the electronic structure of the μ-oxo-Fe^{III}_2 core which is present in oxyhemerythrin, Figure 1B, and has unusual spectral features indicating that the electronic structure is dominated by the oxo bridge.[27] The polarized single-crystal spectrum of oxyhemerythrin combined with SCF-Xα-SW calculations allows further definition of the electronic structure of the hydroperoxo–Fe(III) bond and its contribution to reversible O_2 binding. A common theme for all these studies is that the charge-transfer transitions directly probe ligand–metal bonding and that the dominant spectral features exhibited by the complexes in Figure 1 indicate highly covalent bonds which can make a significant contribution to reactivity.[28]

II. Electronic Structures of Peroxo–Cu(II) Complexes

Spectroscopic studies of a series of copper–peroxo complexes have provided significant insight into the nature of copper–peroxo bonding. Several binding modes of peroxide to Cu(II) are known, although only two copper–peroxo model complexes have been structurally characterized by X-ray crystallography; a *trans*-μ-1,2 end-on dimer, $[\{Cu(TMPA)\}_2(O_2)]^{2+}$,[29] (Figure 2B) and a side-on μ-η^2:η^2 dimer, $[Cu(HB(3,5\text{-}i\text{-}Pr_2pz)_3)]_2(O_2)$[11,30] (Figure 2C). Recently, oxyhemocyanin (oxyHc) has also been characterized by X-ray crystallography and was found to also have a side-on, μ-η^2:η^2 bridging peroxide.[10] Finally, a copper–peroxo monomer $[Cu_2(XYL\text{–}O\text{–})(O_2)]^+$ (Figure 2A), has been spectroscopically characterized but could not be crystallized.[31,32] Spectroscopic studies of these three model complexes and oxyHc have permitted an electronic structure comparison between the different copper–peroxide binding modes and provide insight into the electronic structure contribution to reversible binding of dioxygen by hemocyanin.

The highest occupied molecular orbitals (HOMOs) of peroxide are a pair of degenerate π^* antibonding

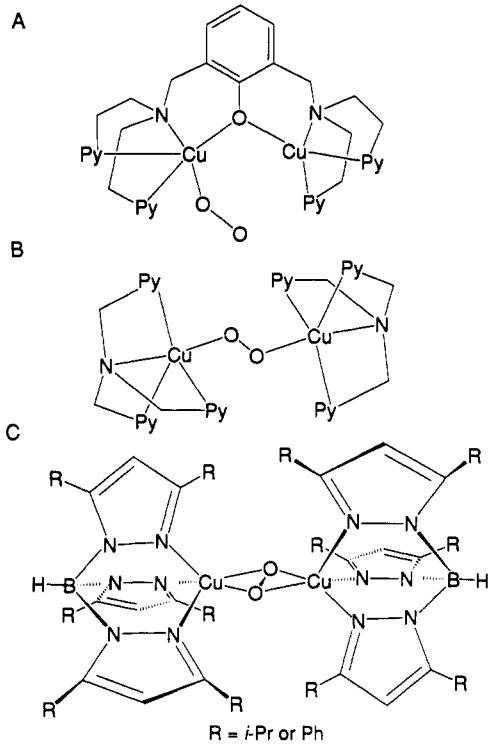

Figure 2. Peroxo–copper complexes with different peroxide binding geometries: (A) end-on monomer, $[Cu_2(XYL\text{–}O\text{–})(O_2)]^+$, (B) *trans* end-on dimer, $[\{Cu(TMPA)\}_2(O_2)]^{2+}$, and (C) side-on dimer, $[Cu(HB(3,5\text{-}i\text{-}Pr_2pz)_3)]_2(O_2)$.

orbitals. When peroxide binds end-on to a copper(II) ion, these π^* peroxide valence orbitals split in energy due to a bonding interaction with the half-occupied $d_{x^2-y^2}$ HOMO of the copper ion (Figure 3). One of the π^* orbitals, designated π^*_σ, is oriented in the plane of the copper $d_{x^2-y^2}$ orbital along the ligand metal bond and is stabilized by a strong σ-donor interaction with the copper ion. The other π^* orbital, the π^*_v, is oriented normal (or vertical) to the plane of the $d_{x^2-y^2}$ orbital and thus has only a weak π interaction with the copper ion. The stabilization of the π^* orbitals is proportional to their overlap with the Cu valence orbitals. Thus, the $O_2^{2-} \rightarrow$ Cu(II) charge transfer (CT) transition originating from the peroxide π^*_σ orbital is at higher energy than the $O_2^{2-} \rightarrow$ Cu(II) CT transition originating from the peroxide π^*_v orbital. In the Mulliken approximation,[33]

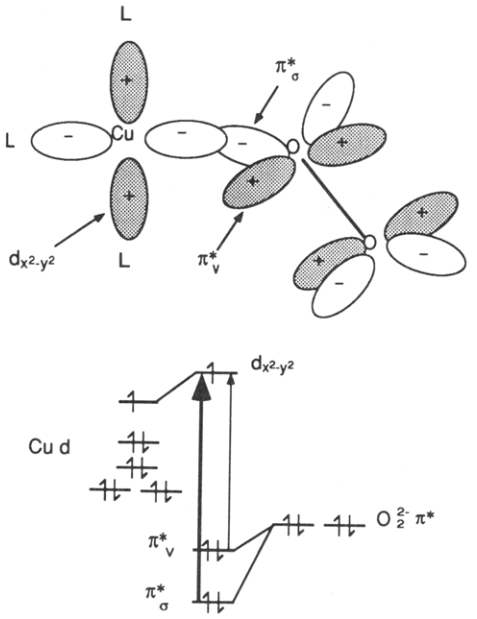

Figure 3. Peroxide–copper bonding and peroxide-to-copper charge-transfer transitions for peroxide bound end-on to one Cu(II).

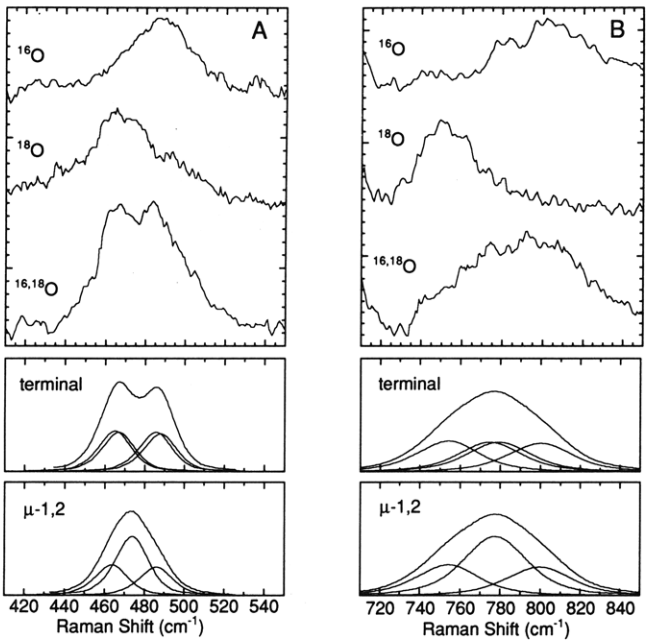

Figure 4. Resonance Raman spectra of the end-on monomer $[Cu_2(XYL–O–)(O_2)]^+$ showing (A) the Cu–O stretch and (B) the O–O stretch for $^{16}O_2$, $^{16}O^{18}O$, and $^{18}O_2$ isotopes. Below these are simulated spectra based on the experimental frequencies and line shapes of these peaks assuming either a symmetric (μ-1,2) or asymmetric (terminal) binding geometry.

the intensity of the $O_2^{2-} \rightarrow$ Cu(II) CT transitions is also proportional to the square of the overlap between the peroxide π* and Cu d orbitals involved in the transition so that the $\pi^*_\sigma \rightarrow$ Cu(II) CT transition is predicted to be more intense than the $\pi^*_v \rightarrow$ Cu(II) CT transition. Thus, the UV/vis CT absorption spectrum of a complex with peroxide bound end-on to a single Cu(II) is expected to exhibit a higher energy, higher intensity $\pi^*_\sigma \rightarrow$ Cu(II) CT transition and a lower energy, lower intensity $\pi^*_v \rightarrow$ Cu(II) CT transition.

The complex $[Cu_2(XYL–O–)(O_2)]^+$ (Figure 2A) exhibits the $O_2^{2-} \rightarrow$ Cu(II) CT absorption intensity pattern described above. This complex has not been crystallized but is spectroscopically well characterized and is found to have peroxide bound end-on to a single copper. Thus this complex provides quantitative information concerning the copper–peroxide interactions described in the qualitative MO model in Figure 3 and a basis for understanding more complicated copper dimer structures in which the peroxo bridges the two copper ions. The peroxo binding geometry in $[Cu_2(XYL–O–)(O_2)]^+$ was determined by a resonance Raman isotope study.[32] Several peroxo binding geometries were considered, including bridging modes since the complex contains two copper ions bridged by a phenolate oxygen. The complex exhibits Raman peaks at 803 and 488 cm^{-1} which shift to 750 and 464 cm^{-1}, respectively, when $^{18}O_2$ is substituted for $^{16}O_2$ and are therefore assigned as O–O and Cu–O stretches (Figure 4). This confirmed the presence of dioxygen bound to the copper as peroxide. The effect of a mixed isotope, $^{16,18}O_2$, substitution on these peaks was used to determine the peroxide binding geometry. A 1:2:1 statistical mixture of $^{16}O_2$:$^{16}O^{18}O$:$^{18}O_2$ was used. If the peroxide were bound such that its oxygens were inequivalent there would be two possible orientations of the $^{16}O^{18}O$ with different O–O and Cu–O stretching frequencies. A normal coordinate analysis showed that for a μ-1,1 bridging geometry or end-on terminal binding to only one of the copper ions, the ν(Cu–O) peak splitting should be large enough to be observed. In contrast, for a *cis*- or *trans*-μ-1,2 bridging geometry in which the oxygens are equivalent, no splitting of either the O–O stretch or symmetric Cu–O stretch would occur. A splitting of the Cu–O stretch was in fact observed, ruling out the symmetric μ-1,2-geometry (Figure 4A). In agreement with a simulated Raman spectrum using frequencies calculated by normal coordinate analysis and the experimental band shapes, no splitting of the O–O stretch was observed due to the large component band width of the ν(O–O) peak and the smaller calculated splitting for the ν(O–O) (Figure 4B). A μ-1,1 bridging geometry was ruled out by EXAFS results which showed the Cu···Cu distance to be 3.31 Å,[34] which is too large for a μ-1,1 bridge on the basis of structural analogy to crystallographically defined hydoxo and methoxo doubly bridged copper dimers with the same (XYL–O–) ligand. In conclusion, detailed analysis of the mixed isotope results indicates that the peroxide is end-on bound to one copper and any interaction of the peroxide with the second copper is minor. This complex will therefore be referred to as an end-on monomer.

Analysis of the electronic absorption spectrum of the end-on monomer (Figure 5) shows that the electronic structure of this complex can be interpreted in terms of the simple description of $Cu–O_2^{2-}$ bonding depicted in Figure 3. The two CT bands at 503 nm (19 900 cm^{-1}, ϵ = 5 800 M^{-1} cm^{-1}) and 625 nm (16 000 cm^{-1}, ϵ = 1 100 M^{-1} cm^{-1}) are assigned as π^*_σ and $\pi^*_v \rightarrow$ Cu(II) CT bands, respectively. Resonance Raman profiles of the O–O and Cu–O stretches show enhancement by both CT bands, confirming these assignments (Figure 5).[32] Due to greater overlap with the copper ion, the π^*_σ orbital is more Cu–O bonding than the π^*_v; the π^*_v, with less Cu character, is more O–O antibonding than the π^*_σ. The $\pi^*_\sigma \rightarrow$ Cu(II) CT transition should therefore cause more distortion of the Cu–O bond length and less distortion of the O–O bond than the $\pi^*_v \rightarrow$ Cu(II) CT transition.

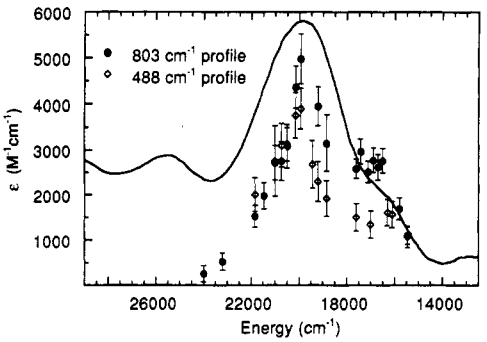

Figure 5. Charge-transfer absorption spectrum of the end-on monomer $[Cu_2(XYL-O-)(O_2)]^+$ with resonance Raman excitation profiles for the O–O stretch (803 cm^{-1}) and the Cu–O stretch (488 cm^{-1}).

Since A-term resonance Raman enhancement by an electronic transition is proportional to the square of the excited-state distortion along the enhanced vibrational mode, the $\pi^*_\sigma \rightarrow$ Cu(II) CT transition should more strongly enhance the Cu–O stretch and more weakly enhance the O–O stretch than the $\pi^*_v \rightarrow$ Cu(II) CT transition. The O–O and Cu–O vibrations show enhancement from both the 503- and 625-nm $O_2^{2-} \rightarrow$ Cu(II) CT transitions. The 488-cm^{-1} Cu–O stretch, however, shows relatively less enhancement than the 803-cm^{-1} O–O stretch from the 625-nm shoulder, consistent with assignment of the 503-nm band as the $\pi^*_\sigma \rightarrow$ Cu CT transition and the 625-nm band as the $\pi^*_v \rightarrow$ Cu(II) CT transition.

SCF-Xα-SW calculations were performed on an end-on copper–peroxo monomer model, $(NH_3)_3CuO_2$, with square planar coordination geometry.[35] The results of these calculations agree with the qualitative description of copper–peroxide bonding above. The half-occupied HOMO of the complex is primarily Cu $d_{x^2-y^2}$ with contributions from the peroxide π^*_σ and nitrogen ligand orbitals which are antibonding with respect to the Cu $d_{x^2-y^2}$ orbital (Figure 6A). The next highest molecular orbital, the π^*_v, has predominantly peroxide character and is oriented vertical to the Cu $d_{x^2-y^2}$ orbital with a node in the Cu–O–O plane. The peroxide orbital interacts weakly with the Cu d orbitals and the electron density remains equally distributed between the oxygen atoms. The π^*_σ orbital is stabilized below the π^*_v orbital due to the σ-bonding interaction between the peroxide π^*_σ and the Cu $d_{x^2-y^2}$ orbitals (Figure 6B). The nitrogen ligand orbitals contribute very little to this wave function. The σ-donor interaction of the peroxide π^*_σ orbital with the Cu $d_{x^2-y^2}$ is reflected by lower electron density on the oxygen atom bound to the copper compared to the terminal oxygen atom, both in the π^*_σ molecular orbital and also in total electron density (not shown).[35]

The first peroxo-bridged copper dimer to be structurally characterized by X-ray crystallography, $[\{Cu(TMPA)\}_2(O_2)]^{2+}$, has a *trans*-$\mu$-1,2 end-on peroxo-bridging geometry[36] (Figure 2B). The copper ions have a distorted trigonal bipyramidal coordination geometry with the pyridyl nitrogens in the equatorial positions and the aliphatic amine and peroxide in the axial positions. The planar C_{2h} Cu_2O_2 unit has Cu–O, O–O, and Cu···Cu distances of 1.852, 1.432, and 4.359 Å, respectively, and the complex has crystallographic C_i symmetry. To gain insight into the electronic structure

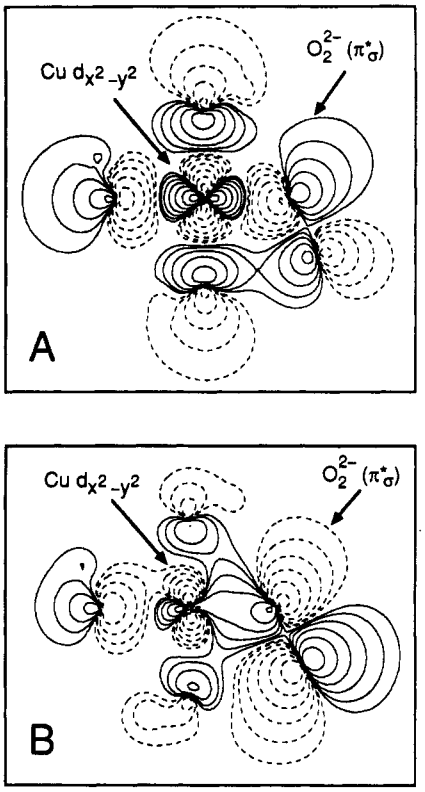

Figure 6. SCF-Xα-SW calculation for an end-on peroxo–copper monomer $(NH_3)_3CuO_2$: contour plots of (A) the HOMO and (B) the π^*_σ bonding molecular orbital.

of an end-on peroxo-bridging geometry, BS-SCF-Xα-SW calculations were performed on a *trans*-μ-1,2-peroxo-bridged model.[35] The calculation described here was performed on a C_{2h} model structure, $[(NH_3)_3CuO_2Cu(NH_3)_3]$, with square-planar coordination around each Cu to facilitate comparison with the end-on monomer calculation. (A calculation on a *trans*-dimer structure with trigonal bipyramidal coordination around the copper ions which more closely resembles the TMPA complex was performed and yielded qualitatively similar results to the C_{2h} calculation summarized here).[37] The LUMO and HOMO of the *trans*-μ-1,2-peroxo-bridged model contain symmetric and antisymmetric combinations of the Cu $d_{x^2-y^2}$ orbitals with the one-electron orbitals primarily localized on one side of the dimer (Figure 7). In the spin-up and spin-down HOMO and LUMO orbitals, the Cu $d_{x^2-y^2}$ orbital on which the electron density is localized has an antibonding interaction with the peroxide π^*_σ orbital. The interaction of the peroxide π^*_σ orbital with the other Cu $d_{x^2-y^2}$ orbital is antibonding in the LUMO and bonding in the HOMO resulting in the HOMO–LUMO splitting. This HOMO–LUMO splitting correlates to the magnitude of the ground-state exchange coupling between the two halves of the dimer due to the bridging peroxide[38] and has implications for excited-state dimer interactions which will be discussed in section III. The next highest occupied energy level, the molecular π^*_v, has mostly peroxide character with a small contribution from the Cu $d_{xz,yz}$ orbitals. The primarily peroxide π^*_σ level (Figure 7C) is at much deeper energy due to stabilization by a strong σ-bonding interaction with the Cu $d_{x^2-y^2}$ orbital. Significant differences are observed between the monomer and the *trans* dimer. The calculated splitting of the π^*_σ and π^*_v orbitals is much greater in the

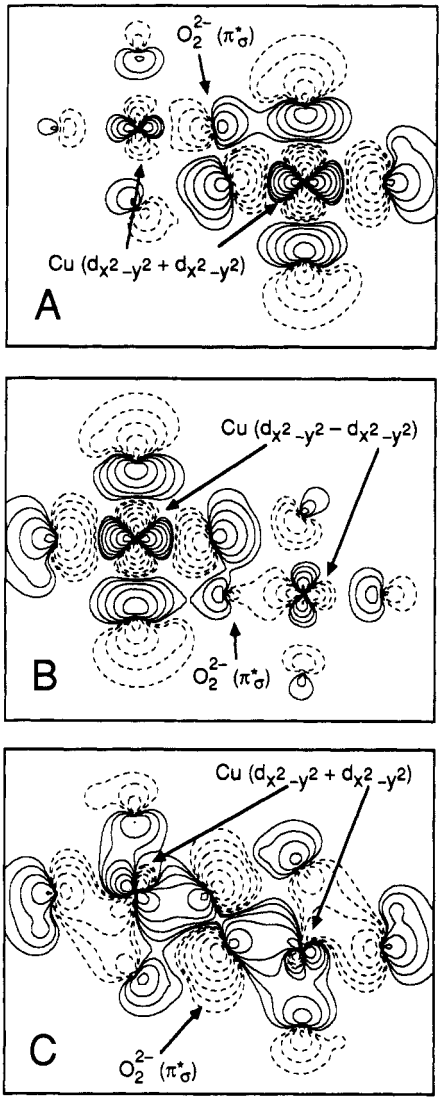

Figure 7. BS-SCF-Xα-SW calculation for a *trans* end-on peroxo–copper dimer: contour plots of (A) the LUMO, (B) the HOMO, and (C) the π^*_σ orbital.

trans dimer than in the monomer due to the second σ-bonding interaction of peroxide with Cu in the dimer. Also, there is less total electron density on the peroxide in the dimer due to the two σ-donor interactions shifting electron density to the copper ions. The σ-donor interactions remove electron density from a peroxide antibonding orbital resulting in a stronger O–O bond and a higher O–O force constant in the dimer.

The absorption spectrum of the *trans* dimer complex (Figure 8) has charge-transfer bands at 435 nm (23 000 cm^{-1}, ϵ = 1 700 M^{-1} cm^{-1}), 524 nm (19 100 cm^{-1}, ϵ = 11 300 M^{-1} cm^{-1}), and 615 nm (16 250 cm^{-1}, ϵ = 5 800 M^{-1} cm^{-1}).[37] The bands at 524 and 615 nm are assigned as the π^*_σ and $\pi^*_v \rightarrow$ Cu(II) CT transitions, respectively, on the basis of their intensities and energies. The intensity of the O_2^{2-} $\pi^*_v \rightarrow$ Cu(II) CT band is greater than for the monomer and side-on dimer peroxo–copper complexes. This is attributed to mixing of the d orbitals due to deviation of the ligand field from ideal trigonal bipyramidal geometry in the $[\{Cu(TMPA)\}_2(O_2)]^{2+}$ complex, allowing greater overlap between the π^*_v and the half-occupied Cu(II) d orbital. Raman peaks observed at 832 and 561 cm^{-1} shift to 826 and 554 cm^{-1} with $^{18}O_2$ isotopic substitution identifying these vibrations as O–O and Cu–O stretches (Figure 8, insets). A normal coordinate analysis shows that the higher O–O stretching frequency in the end-on dimer compared to the monomer reflects a higher O–O force constant (3.1 mdyne/Å vs 2.9 mdyne/Å for the monomer). This is consistent with the SCF-Xα-SW calculations which showed that the additional σ-donor bonding interaction in the dimer as compared to the monomer resulted in a less negative peroxide with less electron density in the π^*_σ antibonding orbital.

The resonance enhancement behavior of the ν(O–O) peak (Figure 8) is consistent with the assignment of the absorption spectrum with both $O_2^{2-} \rightarrow$ Cu(II) CT bands giving enhancement, the greater enhancement coming from the $\pi^*_v \rightarrow$ Cu(II) CT transition as in the monomer. The resonance behavior of the ν(Cu–O) peak, however, is different from that in the monomer, indicating that the excited-state distortions along the Cu–O stretching mode are very different in the dimer. The ν(Cu–O) peak is enhanced by the 435- and 615-nm transitions but not the 524-nm transition. The lack of enhancement by the 524-nm transition is attributed to the strong electronic coupling of the two halves of the domer in the π^*_σ excited state which causes the excited-state distortion to be the same on both sides of the dimer and leads the Cu–O distorting forces to cancel.[37] The similar enhancement of the 435- and 615-nm bands led to an assignment of the 435-nm band as a second component of the π^*_v transition.

The presence of two components of the $\pi^*_v \rightarrow$ Cu(II) CT transition provides an example of the excited-state splitting we have found to occur in bridged copper dimers[25,39–42] (section III). Figure 9 qualitatively shows that the two observed components of the π^*_v are singlet and triplet states split by an excited-state exchange interaction, J^{CT}. This is similar to the antiferromagnetic coupling in the ground state, J^{GS}, but involves the CT excited state. The singlet and triplet states are each further split into symmetric (g) and antisymmetric (u) combinations of the CT excitations to each copper center. Only one of the resulting four states is electric dipole allowed in the *trans* end-on bridged complex and the CT transition to the triplet π^*_v excited state gains intensity through spin–orbit coupling. The origin of the CT excited-state splittings is discussed in section III. The charge-transfer states calculated in the BS-SCF-Xα-SW approximation do not allow for this splitting.[35] The magnitude of the excited-state exchange splitting is dependent on the overlap between the Cu $d_{x^2-y^2}$ and peroxide π^* orbitals containing the unpaired electrons. Thus, J^{CT} is much greater for the π^*_σ CT excited state than for the π^*_v CT excited state. Consequently, the $\pi^*_v \rightarrow$ Cu(II) transition energy calculated by BS-SCF-Xα-SW ($\sim$16 000 cm^{-1} for the *trans* dimer) corresponds more closely to the observed value (16 500 cm^{-1}) than the calculated $\pi^*_\sigma \rightarrow$ Cu(II) transition energy (calculated $\sim$40 000 cm^{-1}, observed 19 100 cm^{-1}).[35] The observation of both the singlet and triplet π^*_v CT transitions in the *trans*-μ-1,2 bridged dimer provides an experimental determination of the excited-state exchange energy for this state ($-2J^{CT}$ = 7600 cm^{-1}).[37] The excited-state exchange splitting for the π^*_σ CT excited state should be even larger. This will be discussed further in section III.

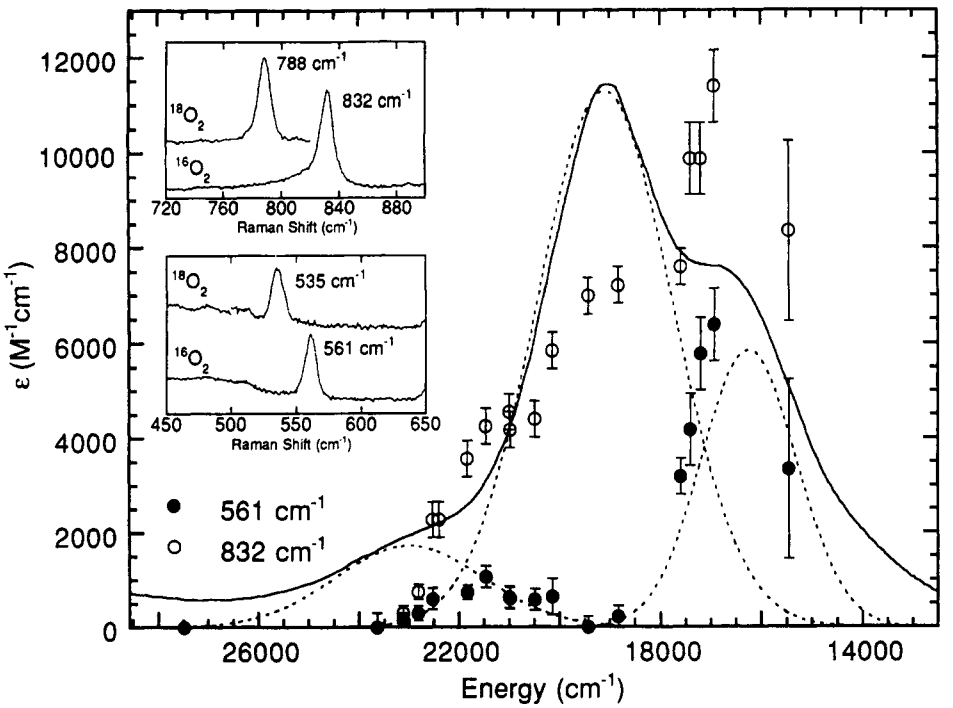

Figure 8. Absorption spectrum of the *trans* end-on dimer $[\{Cu(TMPA)\}_2(O_2)]^{2+}$ with resonance Raman profiles for the O–O and Cu–O peaks. The O–O and Cu–O Raman peaks for $^{16}O_2$ and $^{18}O_2$ isotopes of the complex are shown in the insets.

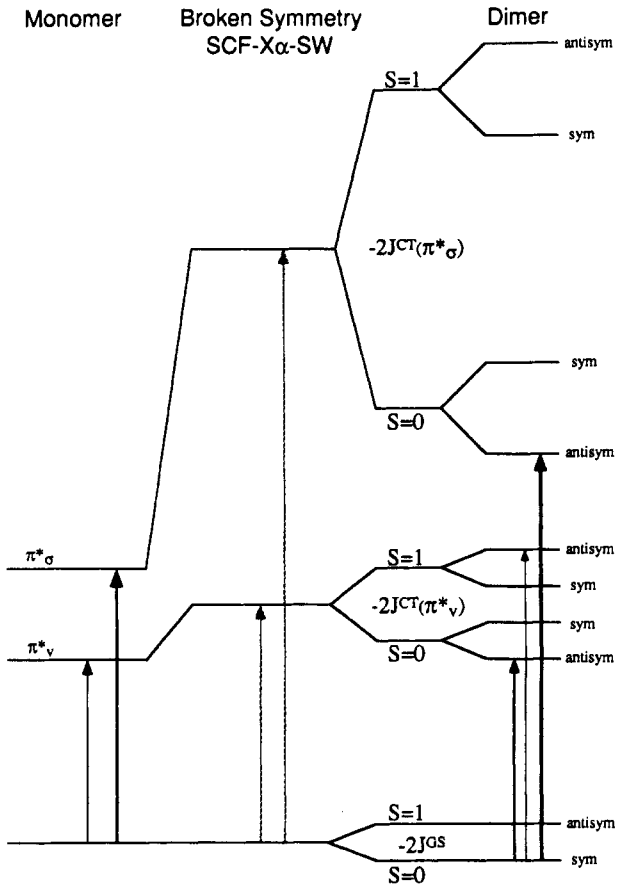

Figure 9. Splitting diagram for the peroxide-to-copper CT excited states of the *trans* end-on complex. Arrows indicate the transitions observed for the monomer (left), the BS-SCF-Xα-SW transition state calculation for a *trans* dimer (center), and the $[\{Cu(TMPA)\}_2(O_2)]^{2+}$ *trans* end-on dimer complex (right).

The side-on μ-η^2:η^2-peroxo-bridging geometry found in $[Cu(HB(3,5\text{-}i\text{-}Pr_2pz)_3)]_2(O_2)$ (Figure 2C) and oxyhemocyanin exhibits an electronic structure quite different from that of the end-on bridging geometries. The $[Cu(HB(3,5\text{-}i\text{-}Pr_2pz)_3)]_2(O_2)$ complex has a crystallographic center of inversion with O–O and Cu–O bond lengths of 1.41 and 1.91 Å, respectively.[11,30] The copper ions are coordinated in a very distorted square pyramidal geometry with two equatorial 2.00-Å and one apical 2.26-Å pyrazole nitrogen ligands. BS-SCF-Xα-SW calculations were performed on a planar D_{2h} side-on model, $[(NH_3)_2Cu]_2O_2^{2+}$, with square planar coordination geometry.[35] The broken symmetry HOMO and LUMO are delocalized onto both halves of the dimer and involve symmetric and antisymmetric (with respect to inversion) combinations of Cu $d_{x^2-y^2}$ orbitals respectively. The delocalization of the broken symmetry orbitals indicates strong coupling between the two halves of the dimer. In the LUMO (Figure 10A), both Cu $d_{x^2-y^2}$ orbitals have an antibonding interaction with the peroxide π^*_σ orbital. The peroxide has two antibonding interactions with each of the two copper ions, indicating an extremely large σ-donor interaction between peroxide and copper. In the HOMO (Figure 10B), a new bonding interaction which is not observed in the monomer or *trans* dimer structures occurs between the Cu $d_{x^2-y^2}$ orbitals and the peroxide σ^* orbital. The peroxide σ^* orbital acts as a π-acceptor, increasing the HOMO–LUMO splitting and stabilizing the copper–peroxide structure. As in the monomer and *trans* dimer structures, the next occupied molecular orbital is primarily composed of the peroxide π^*_v orbital which mixes weakly with the Cu $d_{xz,yz}$ orbitals. The molecular π^*_σ orbital is stabilized to much deeper energy with respect to the π^*_v by the four σ-donor bonding interactions of the peroxide π^*_σ with the copper ions (Figure 10C).

The copper–peroxide bonding interactions described by BS-SCF-Xα-SW calculations on the side-on and *trans* end-on structures are compared in Figure 11. The HOMO–LUMO splitting is several times larger for the side-on dimer than for the *trans* dimer. This arises

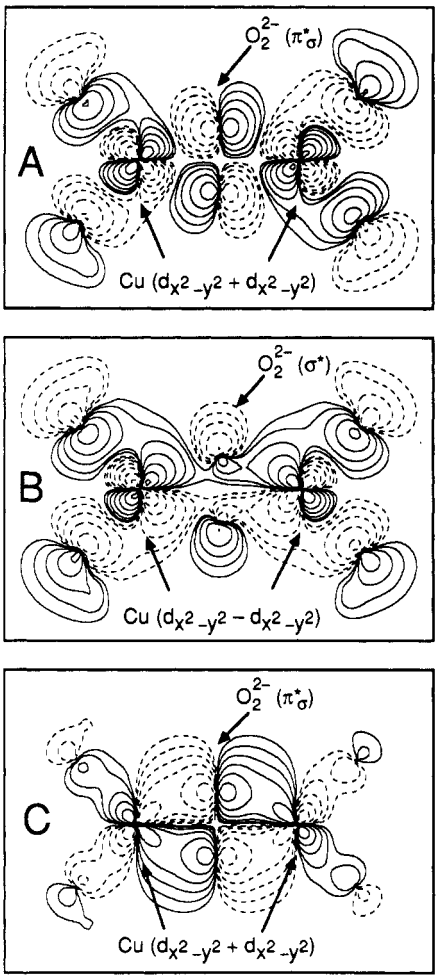

Figure 10. BS-SCF-Xα-SW calculation for a side-on peroxo–copper dimer: contour plots of (A) the LUMO, (B) the HOMO, and (C) the π^*_σ orbital.

from two contributions, the unusual π-bonding interaction of the peroxide σ^* stabilizing the HOMO in the side-on structure and the strong σ-donor interaction of the peroxide π^*_σ destabilizing the LUMO. The energy splitting of the π^*_σ and π^*_v orbitals in the side-on bridged dimer (~5.5 eV) is much greater than that calculated for the *trans* end-on bridged dimer (~2.5 eV) and the monomer (~1 eV) and correlates to the number of σ-bonding interactions present in these three geometries (4, 2, and 1 respectively). As with the *trans* end-on structure, the π^*_v → Cu(II) CT transition energy calculated by BS-SCF-Xα-SW (16 000 cm^{-1}) is in reasonable agreement with the experimental value. However, compared to the *trans* dimer calculation, the larger π^*_σ excited-state antiferromagnetic exchange splitting, resulting from the greater overlap between the π^*_σ and Cu $d_{x^2-y^2}$ orbitals in the side-on dimer, causes the BS-SCF-Xα-SW calculated π^*_σ → Cu(II) transition energy to be overestimated by more than in the *trans* dimer calculation (~65 000 cm^{-1} calculated vs 28 500 cm^{-1} observed for both the [Cu(HB(3,5-*i*-$Pr_2pz)_3$)]$_2(O_2)$ complex and oxyHc).[35] Since the side-on bridging geometry has particularly strong σ donation to the copper, the peroxide oxygens are calculated to have less total electron density than in the *trans* end-on dimer which in turn has less total electron density on the peroxide than in the monomer. The side-on structure therefore has the greatest donation of antibonding electron density from the peroxide to the coppers and might be expected to have the strongest intraperoxide bond and thus a high peroxide stretching frequency. However, the π-acceptor interaction of the peroxide σ^* serves to weaken the O–O bond, accounting for the surprisingly low O–O stretching frequencies observed for the [Cu(HB(3,5-*i*-$Pr_2pz)_3$)]$_2(O_2)$ complex and oxyHc (*vide infra*).

The [Cu(HB(3,5-*i*-$Pr_2pz)_3$)]$_2(O_2)$ complex exhibits intense O_2^{2-} → Cu(II) CT transitions at 350 nm (28 600 cm^{-1}, ϵ = 26 000 M^{-1} cm^{-1}) and 538 nm (18 600 cm^{-1}, ϵ = 2 000 M^{-1} cm^{-1}), assigned as the π^*_σ and π^*_v → Cu(II) CT transitions[11,30,35,43] (Figure 12A). OxyHc exhibits very similar π^*_σ → Cu(II) and π^*_v → Cu(II) CT transitions at 340 nm (29 400 cm^{-1}) and 570 nm (17 500 cm^{-1}) as well as an additional band in the CD not observed in the absorption spectrum[39] (Figure 12B). The assignment of these transitions as O_2^{2-} → Cu(II) CT transitions is consistent with the Raman enhancement of the O–O stretch by these bands in the side-on complex[43] and in oxyHc.[4,44] The absorption intensities of the O_2^{2-} → Cu(II) CT transitions have been used to experimentally quantify the relative peroxide σ donation to the coppers in the monomer, *trans* dimer and side-on dimer complexes.[43] The oscillator strength, *f*, relates the integrated intensity of an absorption band to the transition-moment integral:

$$f_{exp} = (4.32 \times 10^{-9}) \int \epsilon(\nu)\, d\nu \quad (1)$$

$$f_{theory} = (8\pi^2 mc/3h)\nu[\int \psi^g \mathbf{M} \psi^e\, d\tau]^2 \quad (2)$$

ϵ is the molar extinction coefficient (M^{-1} cm^{-1}), ν is the

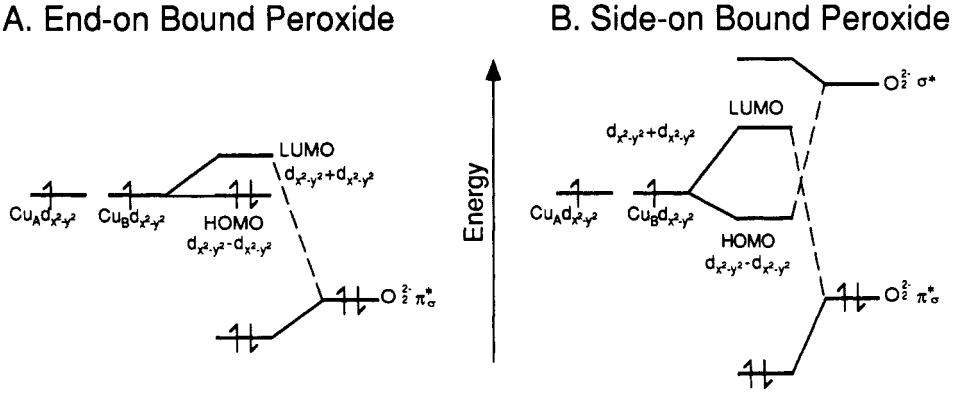

Figure 11. Energy-level diagram for (A) end-on and (B) side-on peroxide-bridging geometries showing the dominant bonding orbitals and approximate energy splittings for the two geometries.

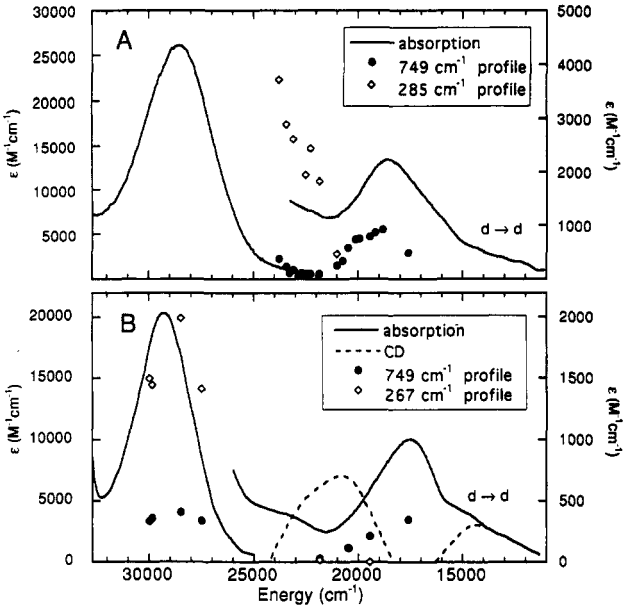

Figure 12. Absorption spectra and resonance Raman profiles of the O–O and Cu–O peaks for (A) the side-on bridged model $[Cu(HB(3,5\text{-}i\text{-}Pr_2pz)_3)]_2(O_2)$ and (B) oxyHc. The ϵ scale for the higher energy region is on the left and ϵ for the lower energy region is on the right.

frequency (cm^{-1}), $[\int \psi^g \mathbf{M} \psi^e \, d\tau]$ is the transition moment integral (cm), ψ^g and ψ^e are the ground and excited states involved in the transition. A CT transition involves excitation from a predominantly ligand (O_2^{2-} π_σ^*) donor orbital, ψ^D, to a predominantly Cu $d_{x^2-y^2}$ half-occupied acceptor orbital, ψ^A, where the CT donor and acceptor orbitals can be expressed as linear combinations of metal, χ_M, and ligand, χ_L, orbitals:

$$\psi^D = C^D{}_M \chi^D{}_M + C^D{}_L \chi^D{}_L \quad (3)$$

$$\psi^A = C^A{}_M \chi^A{}_M + C^A{}_L \chi^A{}_L \quad (4)$$

In the electric dipole approximation the transition-moment integral for the CT transition from ψ^D to ψ^A contains the following four terms:

$$\int \psi^D \mathbf{r} \psi^A \, d\tau = C^D{}_M C^A{}_M \int \chi^D{}_M \mathbf{r} \chi^A{}_M \, d\tau + C^D{}_M C^A{}_L \int \chi^D{}_M \mathbf{r} \chi^A{}_L \, d\tau + C^D{}_L C^A{}_M \int \chi^D{}_L \mathbf{r} \chi^A{}_M \, d\tau + C^D{}_L C^A{}_L \int \chi^D{}_L \mathbf{r} \chi^A{}_L \, d\tau \quad (5)$$

While all of the terms will be similarly related to the overlap of the metal and ligand orbitals, calculations have shown that the ligand–ligand term dominates the intensity of charge-transfer transitions.[45,46] Although orbitals from ligands other than peroxide may contribute to $\chi^A{}_L$, they will have little effect on the transition-moment integral due to lack of overlap with $X^D{}_L$, which has little contribution from ligands other than O_2^{2-}. For the monomer, the ligand–ligand term reduces to $(C^D{}_L C^A{}_L \vec{r})$,[47] where $\vec{r}$ is the vector from the bound oxygen of the peroxide to the metal. For the dimers, the ligand–ligand term in eq 5 reduces to $(C^D{}_L C^A{}_L \vec{r} \cos \phi)$, where ϕ is the angle between the transition vectors to each copper in the dimer. These vectors are taken to be from the center of the O–O bond to the copper. Thus, for the side-on and *trans* end-on dimers in which the transition vectors are from the center of symmetry to the copper ions, $\cos \phi = -1$, and all of the transition intensity is associated with the observed electric dipole-allowed component.

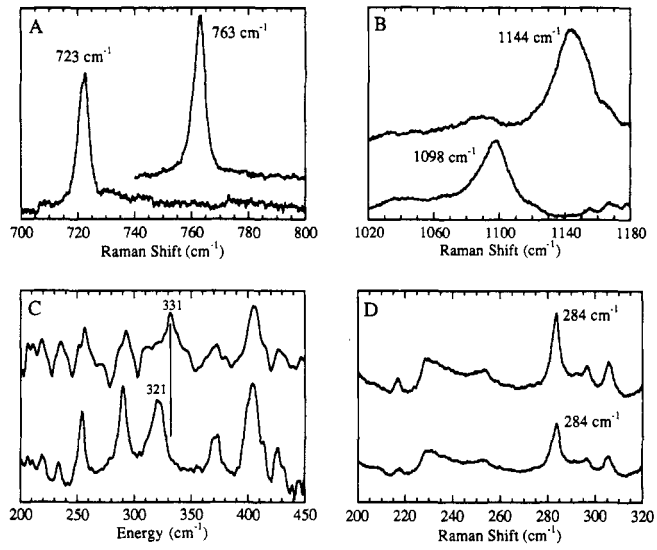

Figure 13. Resonance Raman (A, B, and D) and infrared (D) spectra of the in-plane Cu_2O_2 vibrations of the side-on dimer $[Cu(HB(3,5\text{-}i\text{-}Ph_2pz)_3)]_2(O_2)$.

The σ-donor ability of the peroxide corresponds to the amount of Cu $d_{x^2-y^2}$ character in the fully occupied, predominantly peroxide π_σ^* orbital which is given by $(C^D{}_M)^2$. Since ψ^D has only Cu $d_{x^2-y^2}$ and O_2^{2-} π_σ^* character, the σ-donor ability may be estimated using $(C^D{}_M)^2 = [1-(C^D{}_L)^2] = (C^A{}_L)^2$. Thus, eq 6 directly relates the σ donation by the peroxide π^*orbitals to the

$$f_{exp}/[(1.085 \times 10^{11})\nu r^2] = (C^A{}_L)^2[1-(C^A{}_L)^2] \approx (C^A{}_L)^2 \quad (6)$$

intensities of the $O_2^{2-} \rightarrow$ Cu(II) CT transitions in Figures 5, 8, and 12, permitting an experimental estimate of the relative peroxide charge donation to the copper ions. By using equation 6, the oscillator strengths of the $O_2^{2-} \rightarrow$ Cu(II) CT transitions in the monomer (f = 0.06), *trans* dimer (f = 0.15), and side-on dimer (f = 0.29) complexes give a ratio of peroxide to metal charge donation of 1:1.9:3.7 for this series. This indicates that the peroxide donates approximately twice the electron density (or roughly the same amount per copper) to two end-on bound copper ions as to one. The high absorption intensity of the 350-nm CT band in the side-on peroxo-bridged complex reflects donation of nearly four times as much peroxide electron density to the copper ions compared to the monomer, or twice as much per copper as either end-on complex. This produces a less negative peroxide in the side-on bridged dimer than in the end-on bridged dimer, which is, in turn, less negative than the monomer, in agreement with the BS-SCF-Xα-SW calculations.

Four vibrational modes of the copper–peroxide unit were observed in the resonance Raman and infrared spectra of $[Cu(HB(3,5\text{-}R_2pz)_3)]_2(O_2)$[43] (Figure 13). A more stable close analogue of the *i*-Pr side-on complex with R = Ph rather than *i*-Pr was used for the normal coordinate study. An unusually low intra-peroxide stretching frequency of 763 cm^{-1} which shifted to 723 cm^{-1} with $^{18}O_2$ was observed in the Raman spectrum (ν = 749 cm^{-1} in both the R = *i*-Pr derivative and oxyHc).

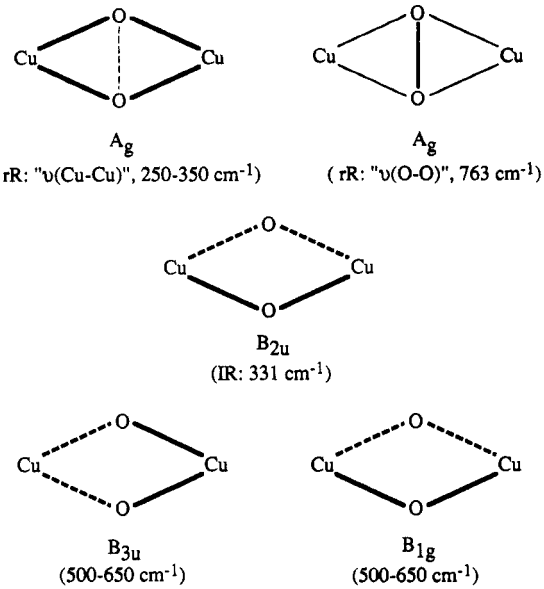

Figure 14. In-plane normal vibrational modes of the side-on bridging Cu_2O_2 unit. Solid and broken lines represent opposite distortions. Thicker lines indicate the dominant motion in the two A_g modes.

This peak was enhanced by both $O_2^{2-} \rightarrow$ Cu(II) CT transitions in the resonance Raman profile. Raman peaks at 284 cm^{-1} (no shift with $^{18}O_2$) and 1144 cm^{-1} (1098 cm^{-1} with $^{18}O_2$) and a peak at 331 cm^{-1} in the IR spectrum were also assigned as copper–peroxide modes. One striking feature of the Raman spectrum of the side-on complex is the lack of a totally symmetric Cu–O stretch at ~500–650 cm^{-1} as is typically observed in cobalt–peroxide dimers and the monomer and *trans* end-on copper–peroxo dimer complexes. A normal coordinate analysis reveals that in the side-on D_{2h} copper–peroxo unit, the A_g symmetric Cu–O stretch involves primarily copper motion and thus occurs at low frequency (Figure 14). The 284-cm^{-1} peak, identified as a vibration of the copper–peroxo unit from its enhancement by the $O_2^{2-} \rightarrow$ Cu(II) CT bands (Figure 12), is assigned to this mode. (Note that the full rR profile was obtained for the analogous 285 cm^{-1} peak in the R = *i*-Pr complex). The lack of an $^{18}O_2$ isotope shift for the 284-cm^{-1} peak is reasonable in light of this assignment since little oxygen motion occurs in this mode (Figure 14). The 285-cm^{-1} peak is much more enhanced by the $\pi_\sigma^* \rightarrow$ Cu(II) CT transition than by the $\pi_v^* \rightarrow$ Cu(II) CT transition. These results are consistent with the description of this mode as a Cu···Cu stretch since the $\pi_\sigma^* \rightarrow$ Cu(II) CT transition involves excitation from a bonding to an antibonding orbital with respect to the four Cu–O bonds involved in Cu···Cu motion, whereas the $\pi_v^* \rightarrow$ Cu(II) CT transition shifts electron density out of the O–O antibonding π_v^*, shortening the O–O bond but not greatly affecting the Cu···Cu distance. The normal coordinate analysis predicts other, non-totally symmetric copper–peroxide stretching modes of B_{3u} and B_{1g} symmetry to occur in the 500–650-cm^{-1} range but these modes have no resonance intensity due to their symmetry.[48] The Raman peak at 1 144 cm^{-1} is assigned as the totally symmetric overtone of one of these two modes. The normal coordinate calculation using these assignments shows that the low O–O stretching frequency does reflect a low O–O force constant of 2.4 mdyn/Å.

The experimentally derived peroxide σ-donor strength and intraperoxide force constants (k_{O-O} = 2.9, 3.1, and 2.4 mdyne/Å for the monomer, *trans* end-on dimer, and side-on dimer, respectively) for the three peroxo–copper models are consistent with the BS-SCF-Xα-SW description of peroxo–copper bonding for this series of binding geometries. The increasing σ-donation of electron density from the peroxide to the copper on going from the monomer to the end-on dimer to the side-on dimer indicated by the SCF-Xα-SW calculations is reflected in the increasing $O_2^{2-} \rightarrow$ Cu(II) CT transition intensities from which the 1:1.9:3.7 ratio of σ-donation is derived for the series. The degree of σ donation out of the π^* O–O antibonding orbitals is also reflected in the O–O force constants for the monomer and *trans* dimer models. The side-on complex, however, despite having the strongest σ-donor interaction, has an offsetting π-acceptor interaction involving the strongly O–O antibonding O_2^{2-} σ^* orbital, which greatly weakens the O–O bond. The side-on dimer thus has a less negative (more "superoxide-like") peroxide which nevertheless has an extremely weak O–O bond.

These studies of the electronic structure of the end-on and side-on dimers provide an understanding of the electronic structural contributions to the reactivity of the side-on peroxide bound active sites of hemocyanin and tyrosinase. This is discussed in section VII. Clearly the peroxide CT spectrum provides important insight into the peroxo–copper bond. There are, however, several features of the CT spectrum of the peroxo-bridged dimers yet to be addressed. These include the discrepancy between the calculated and observed $\pi_\sigma^* \rightarrow$ Cu(II) CT transition energies and the additional higher energy triplet component of the $\pi_v^* \rightarrow$ Cu(II) transition observed for the *trans* complex, both due to excited-state dimer splittings. Also, the third CT transition observed in the CD spectrum of oxyhemocyanin indicates a splitting of the allowed singlet transitions due to dimer interactions. These will be considered in the following sections.

III. Charge-Transfer Excited States in Dimers

A theoretical understanding of the effects of dimer formation on excited electronic states is of central importance for the interpretation of the optical spectra of bridged-metal systems. Here, we are mainly interested in dimer effects on the bridging ligand → metal charge-transfer states. Copper(II)–peroxo complexes are prototype systems for this problem since they have only one magnetic orbital per metal site and they exist with various ligand binding modes which all show very different peroxide → Cu(II) CT spectra (section II). In this section, the problem of CT excited-state splittings of copper–peroxide systems is presented from a general point of view and then applied to oxyhemocyanin in section IV.

We consider a dimeric Cu(II) complex bridged by peroxide. In order to simplify the treatment, only the highest orbitals of O_2^{2-}, π_σ^* and π_v^*, and the highest, singly occupied orbitals d_A and d_B of the two Cu(II) centers are included. A ligand → metal CT (LMCT) transition may go from the π_σ^* or the π_v^* orbital of the bridging peroxide to the "left" or the "right" copper center meaning that both the $\pi_\sigma^* \rightarrow$ Cu and the $\pi_v^* \rightarrow$ Cu(II) CT states are doubly degenerate. Empirically,

Scheme 1

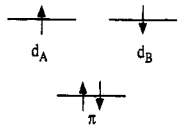

Scheme 2

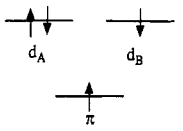

it is found that each of these degeneracies is lifted by dimer interactions leading to the so-called *sym–antisym* splitting which may be large (several thousand wavenumbers). Further, each LMCT transition changes the copper configuration from d^9–d^9 to d^9–d^{10} and leaves an unpaired electron in the respective ligand orbital. Coupling of the two unpaired electrons in the ligand and metal orbitals leads to a singlet and a triplet CT state which, again, may split by several thousand wavenumbers. In total, each monomer $\pi_\sigma^* \rightarrow$ Cu(II) or $\pi_v^* \rightarrow$ Cu(II) LMCT state splits into four states in the dimer. The splitting scheme for the π_σ^* ($\equiv \pi$) $\rightarrow$ Cu LMCT transition is derived and the relevant parameters are presented.

The ground-state configuration of a Cu(II)–peroxo dimer may be represented by Scheme 1. The corresponding singlet and triplet states are $^1\Gamma_+^{GS}$ and $^3\Gamma_-^{GS}$ where Γ_+ designates the (totally) symmetric and Γ_- the antisymmetric wave function with respect to a symmetry element relating the two halves of the dimer (mirror plane or center of inversion). A LMCT transition corresponds to a shift of an electron from π to d_A (or d_B), leading to the four CT excited singlet and triplet states $^1\Gamma_+^{CT}$, $^1\Gamma_-^{CT}$, $^3\Gamma_+^{CT}$ and $^3\Gamma_-^{CT}$ shown in Scheme 2. We first consider the diagonal energies of the electronic Hamiltonian consisting of $\sum h(i)$, containing the one-electron kinetic and potential energy operators and a two-electron part $\sum e^2/r_{ij}$, representing the electron–electron repulsion:

$$H = \sum_i h(i) + \sum_{ij} e^2/r_{ij} \tag{7}$$

The resulting energies of the four CT states are

$$\langle {}^1\Gamma_-{}^{CT}\rangle = \Delta E + J_{e\pi} + 2I - L - h_{AB} \tag{8a}$$

$$\langle {}^1\Gamma_-{}^{CT}\rangle = \Delta E + J_{d\pi} - 2I + L + h_{AB} \tag{8b}$$

$$\langle {}^3\Gamma_+{}^{CT}\rangle = \Delta E - J_{d\pi} - L - h_{AB} \tag{8c}$$

$$\langle {}^3\Gamma_-{}^{CT}\rangle = \Delta E - J_{d\pi} + L + h_{AB} \tag{8d}$$

with

$$J_{d\pi} = \int d_A^*(1)\pi(2)|e^2/r_{12}|\pi(1)d_A(2)\, d\tau = \langle d_A\pi|e^2/r_{12}|\pi d_A\rangle = \langle d_B\pi|e^2/r_{12}|\pi d_B\rangle \tag{9a}$$

$$I = \langle d_A\pi|e^2/r_{12}|\pi d_B\rangle \tag{9b}$$

$$L = \langle d_A\pi|e^2/r_{12}|d_B\pi\rangle \tag{9c}$$

$$h_{AB} = \langle d_A|h(1)|d_B\rangle \tag{9d}$$

ΔE is an average dimer CT transition energy which is related to the CT energy Δ of the corresponding monomer (one copper bound to π) by[25]

$$\Delta E = \Delta + J_{d\pi} - K_{d\pi} \tag{10}$$

where

$$K_{d\pi} = \langle d_A\pi|e^2/r_{12}|d_A\pi\rangle = \langle d_B\pi|e^2/r_{12}|d_B\pi\rangle \tag{11}$$

The resulting splitting scheme is shown in Figure 15. Note that an important contribution to the average CT energy in the dimer has not been included. This corresponds to an additional donation of electron density from the ligand to the metals upon bridging which increases the effective nuclear charge of the ligand. By determining Δ from molecular orbital calculations (*vide infra*), this interaction is taken into account. The diagonal splitting of every monomer CT transition in the dimer can be described by the parameters $J_{d\pi}$, I, L, and h_{AB} (eq 9a–d). $J_{d\pi}$ describes the singlet–triplet splitting. I is the Coulomb-mediated excitation transfer integral[49,50] which can be interpreted as an interaction energy between two transition dipoles[51] (Scheme 3). The corresponding contribution $4I$ to the singlet CT-state splitting (eq 8a,b) is accounted for by the transition dipole vector coupling (TDVC) model developed earlier in order to determine CT-state splittings and selection rules in peroxide and analogous azide-bridged copper dimers.[39] The classical interaction energy between two dipoles $\mathbf{M}_1$ and $\mathbf{M}_2$ at a distance $R = |\mathbf{R}|$ is given by

$$E = \frac{\mathbf{M}_1\cdot\mathbf{M}_2}{R^3} - 3\frac{(\mathbf{M}_1\cdot\mathbf{R})(\mathbf{M}_2\cdot\mathbf{R})}{R} \tag{12}$$

This expression has been evaluated for a *cis*-μ-1,3-azide-bridged Cu(II) dimer with C_{2v} symmetry (Figure 16). Due to the similarity of the π_σ^{nb} orbital of N_3^- with the π_σ^* orbital of O_2^{2-}, metal–azide systems may serve as electronic structural analogues for metal peroxo systems. From eq 12 and Figure 16, the energy difference between the symmetric ("+"; symmetry A_1 in C_{2v}) and the antisymmetric ("–"; symmetry B_1 in C_{2v}) combination of the two transition dipoles is given by[51]

$$\langle\langle {}^1\Gamma_+{}^{CT}\rangle - \langle {}^1\Gamma_-{}^{CT}\rangle\rangle_{TDVC} = \Delta E(A_1 - B_1) = 2\frac{\mathbf{M}^2}{\mathbf{R}^3}(\cos\Phi + 3\cos^2\Theta) \tag{13}$$

Here, Θ is the angle between the vector $\mathbf{R}$ and $\mathbf{M}_1$ (or $\mathbf{M}_2$), and Φ is the angle between the two dipoles (Figure 16). Note that the "+" combination of the transition dipoles corresponds to a CT transition from $^1\Gamma_+^{GS}$ to $^1\Gamma_+^{CT}$ (symmetry A_1) and the "–" combination to a transition from $^1\Gamma_+^{GS}$ to $^1\Gamma_-^{CT}$ (symmetry B_1). Further, the intensity ratio between the two components of the LMCT transition is given by

$$\frac{I_{A_1}}{I_{B_1}} = \frac{(\mathbf{M}_1 + \mathbf{M}_2)^2}{(\mathbf{M}_1 - \mathbf{M}_2)^2} = \frac{\cos^2(\Phi/2)}{\sin^2(\Phi/2)} \tag{14}$$

By using the observed oscillator strengths of the azide $\pi_\sigma^{nb} \rightarrow$ Cu(II) CT transitions[42] and the structural

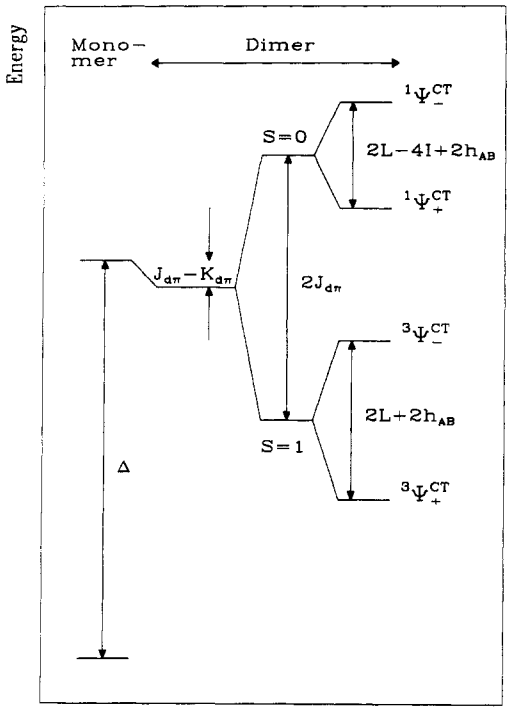

Figure 15. Splitting of a monomer transition in a dimer due to in-state interactions.

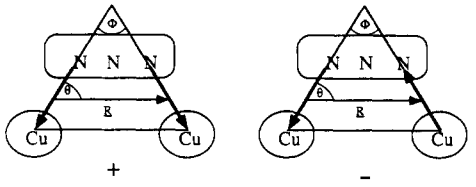

Figure 16. Coupling of two transition dipole vectors in a dimer (TDVC model) for *cis* coordination of a bridging ligand, N_3^-.

Scheme 3

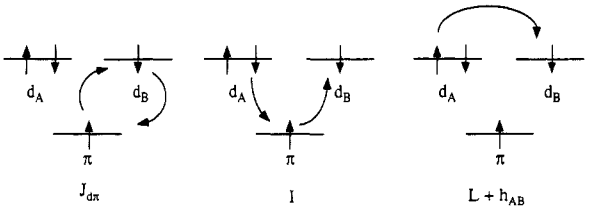

parameters of a *cis*-μ-1,3-azide-bridged Cu(II) dimer, the TDVC model gives a CT-state splitting (eq 13) of 630 cm^{-1} and an intensity ratio (eq 14) of 8.6. The experimentally observed azide → Cu(II) CT intensity pattern allows assignment of its A_1 and B_1 components and the observed value for the π_σ^{nb} → Cu(II) CT-state splitting is $\Delta E(A_1 - B_1) = 3600\ cm^{-1}$.[42] The discrepancy between the observed and theoretical CT-state splitting cannot be ascribed to the neglect of h_{AB} and the exchange-mediated excitation transfer integral L in Scheme 3 since, from exciton theory, L is known to be small compared to I,[49,50,52] and h_{AB} is small as both copper ions are far apart and do not overlap. (Note that in refs 41 and 42, L and h_{AB} have been combined into the L integral which is large in these earlier treatments since nonorthogonal orbitals were employed.) Hence, configuration interaction (CI) between the CT states and other states of the same symmetry has to be considered for a quantitative analysis. As we start from a localized description with the unpaired electrons on each metal, we develop a model of dimer excited-state splitting including CI in a valence-bond (VBCI) approach.

So far, no overlap between the ligand and metal orbitals has been taken into account. Bonding is introduced by the transfer matrix element

$$\langle {}^3\Gamma_-{}^{GS}|H|{}^3\Gamma_-{}^{CT}\rangle = \langle {}^1\Gamma_+{}^{GS}|H|{}^1\Gamma_+{}^{CT}\rangle = \sqrt{2}\langle d_A|h(1)|\pi\rangle \equiv \sqrt{2}h_{d_A\pi} = \sqrt{2}h_{d_B\pi} \equiv h_{d\pi} \quad (15)$$

The triplet secular determinant

$$\begin{vmatrix} \langle {}^3\Gamma_-{}^{GS}\rangle - E & h_{d\pi} \\ h_{d\pi} & \langle {}^3\Gamma_-{}^{CT}\rangle - E \end{vmatrix} = 0 \quad (16)$$

describes the mutual bonding interaction between the triplet ground and $^3\Gamma_-{}^{CT}$ excited state where $\langle {}^3\Gamma_-{}^{GS}\rangle$ and $\langle {}^3\Gamma_-{}^{CT}\rangle$ are the energies of these states in the absence of CI. In contrast, $^3\Gamma_+{}^{CT}$ cannot interact with the ground state. Thus, the interaction (eq 16) is expected to give a large splitting of the triplet CT excited states (Figure 17, right). Analogous considerations apply for the singlet ground and CT states. Here, the symmetric components $^1\Gamma_+{}^{GS}$ and $^1\Gamma_+{}^{CT}$ interact and $^1\Gamma_-{}^{CT}$ is unaffected which gives a splitting order opposite to that of the triplet CT states (Figure 17, left). Whereas the triplet interaction matrix (eq 16) is complete within the three-orbital four-electron picture, there are additional higher-energy singlet states which have to be included: Starting from the CT configuration (Scheme 2), the unpaired electron on d_B may jump to the bridging ligand orbital leading to a metal-to-metal CT (MMCT) state with one Cu(I) (d^{10}) and one Cu(III) ion (d^8 configuration) (Scheme 4), or the unpaired electron on the peroxide may jump to d_B leaving a doubly vacant orbital π (double CT, DCT) (Scheme 5). Whereas there is only one DCT state, $^1\Gamma_+$, the MMCT states are of $^1\Gamma_+$ and $^1\Gamma_-$ symmetry. In total, the two following secular determinants are obtained for the $^1\Gamma_-$ (eq 17) and the $^1\Gamma_+$ states (eq 18):

$$\begin{vmatrix} \langle {}^1\Gamma_-{}^{CT}\rangle - E & h_{d\pi} \\ h_{d\pi} & \langle {}^1\Gamma_-{}^{MMCT}\rangle - E \end{vmatrix} = 0 \quad (17)$$

$$\begin{vmatrix} \langle {}^1\Gamma_+{}^{GS}\rangle - E & h_{d\pi} & 0 & 0 \\ h_{d\pi} & \langle {}^1\Gamma_+{}^{CT}\rangle - E & h_{d\pi} & \sqrt{2}h_{d\pi} \\ 0 & h_{d\pi} & \langle {}^1\Gamma_+{}^{MMCT}\rangle - E & 0 \\ 0 & \sqrt{2}h_{d\pi} & 0 & \langle {}^1\Gamma_+{}^{DCT}\rangle - E \end{vmatrix} = 0 \quad (18)$$

The secular determinants eqs 16–18 involve four parameters, the LMCT energy Δ, the energies of the MMCT and DCT states, $U = \langle {}^1\Gamma^{MMCT}\rangle$ and $E_{DCT} = \langle {}^1\Gamma^{DCT}\rangle$, and the transfer matrix element $h_{d\pi}$. The parameters Δ and $h_{d\pi}$ can be obtained from a MO calculation of the triplet LMCT energies.[25] In this MO framework, the two Cu d orbitals, d_A and d_B, at an energy Δ above π are combined to form the molecular orbitals

$$d_1 = (1/\sqrt{2})(d_A + d_B) \quad (19a)$$

$$d_2 = (1/\sqrt{2})(d_A - d_B) \quad (19b)$$

One combination has the same symmetry as the π orbital and, therefore, mixes with π and becomes the LUMO of the complex, whereas the other combination has a symmetry different from π, stays nonbonding and becomes the HOMO; the corresponding energy splitting

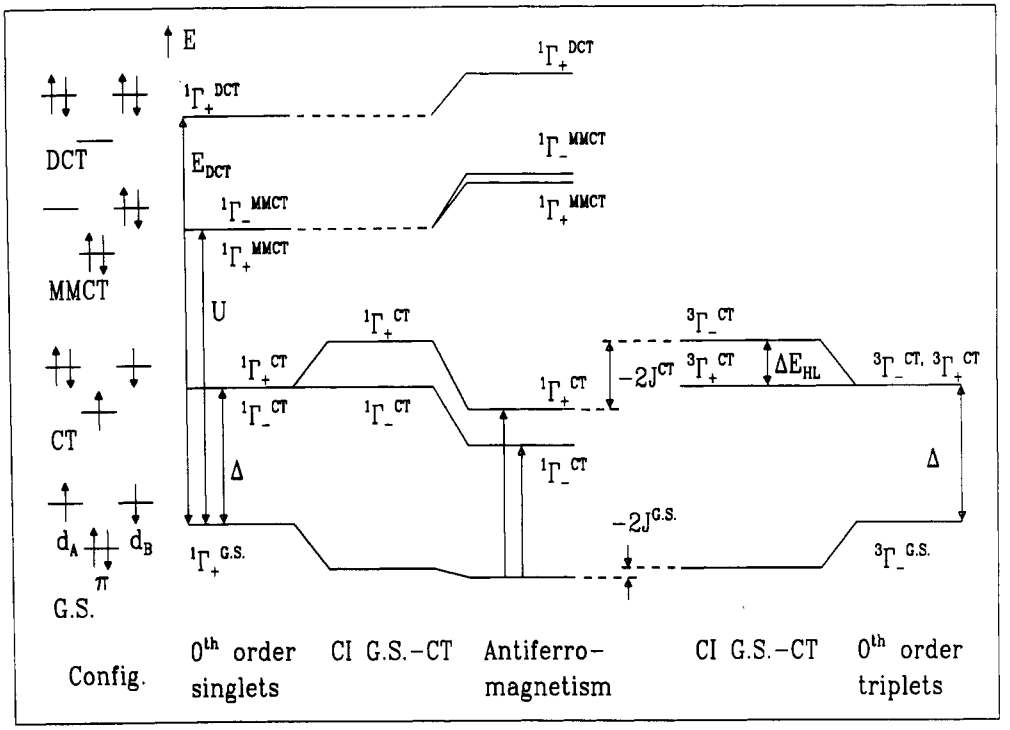

Figure 17. Energy-level scheme resulting from application of the VBCI model. Observed transitions are indicated by arrows in center.

Scheme 4

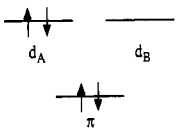

Scheme 5

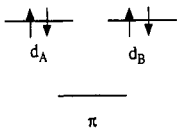

is the HOMO–LUMO gap ΔE_{HL}. In terms of MO functions, the triplet $M_S = 1$ ground state $^3\Gamma_-^{GS}$ is given by the Slater determinant $|(\pi^+)(\pi^-)(HOMO^+)(LUMO^+)|$, the triplet $^3\Gamma_+^{CT}$ $M_S = 1$ CT state by the Slater determinant $|(\pi^+)(HOMO^+)(HOMO^-)(LUMO^+)|$ (both unpaired electrons in orbitals of same symmetry), and the CT state $^3\Gamma_-^{CT}$ ($M_S = 1$) by $|(\pi^+)(HOMO^+)(LUMO^-)(LUMO^+)|$ (both unpaired electrons in orbitals of different symmetry). It can be shown that the energies and eigenfunctions of the MO model are identical to those resulting from the triplet VBCI matrix (eq 16).[25] Therefore, the VBCI parameters $h_{d\pi}$ and Δ can be calculated from the triplet energies obtained with SCF-Xα-SW transition-state calculations. In particular, Δ is given by (Figure 17, right)

$$[E(^3\Gamma_+^{CT}) - E(^3\Gamma_-^{GS})] - [E(^3\Gamma_-^{CT}) - E(^3\Gamma_+^{CT})] = \Delta \quad (20)$$

and, knowing Δ, $h_{d\pi}$ follows from eq 16

$$E(^3\Gamma_-^{CT}) - E(^3\Gamma_-^{GS}) = 2[(\Delta/2)^2 + h_{d\pi}^2]^{1/2} \quad (21)$$

Note that the $^3\Gamma_-^{CT}$ state is reached from $^3\Gamma_+^{CT}$ by a jump of one electron from the HOMO to the LUMO (*vide supra*). Hence, the energy difference between $^3\Gamma_-^{CT}$ and $^3\Gamma_+^{CT}$ is given by the HOMO–LUMO splitting ΔE_{HL} (Figure 17).

The singlet CT-state splitting has been experimentally observed in strongly antiferromagnetically coupled dimers but the triplet splitting has not. With respect to the singlet energies, the VBCI model predicts that the singlet CT-state splitting is opposite in sign to the triplet CT-state splitting (*vide supra*) but reduced by the interaction of $^1\Gamma_+^{CT}$ with $^1\Gamma_+^{DCT}$ (Figure 17). If $E_{DCT} \gg \Delta$, the singlet CT-state splitting reflects the triplet CT-state splitting which is the HOMO–LUMO splitting and thus provides chemical information about the bonding interaction of the bridging ligand with the metal centers. The VBCI model also predicts that both $^1\Gamma_+^{CT}$ and $^1\Gamma_-^{CT}$ are shifted to lower energy by interaction with the MMCT states of the same symmetry. As the CT triplets are not subject to such an interaction, the CT singlets are at lower energy than the CT triplets. Note that this corresponds to an antiferromagnetic interaction in the CT excited state (excited-state antiferromagnetism, ESAF). As a measure of ESAF, we define the energy difference between the states

$$-2J^{CT} = \langle ^3\Gamma_-^{CT}\rangle - \langle ^1\Gamma_+^{CT}\rangle \quad (22)$$

after configuration interaction with the ground and higher energy CT states, respectively (eqs 16 and 18 and Figure 17, left-middle). If $h_{d\pi} \ll U$, Δ, and E_{DCT}, $-2J^{CT}$ is given by

$$-2J^{CT} = h_{d\pi}^2\left(\frac{1}{U-\Delta} + \frac{1}{(E_{DCT}/2)-\Delta}\right) \quad (23)$$

The physical origin of this interaction is the presence of two unpaired electrons in directly overlapping orbitals, i.e. one in a metal and one in a ligand orbital (Scheme 2). Note the relationship of eq 23 with the HOMO–LUMO splitting ΔE_{HL} which, in the same limit,

is given by $h_{d\pi}^2/\Delta$. Both interactions have the same physical origin and are of the same order of magnitude. Finally, this CT excited-state antiferromagnetism relates to the ground-state antiferromagnetism due to mixing of the CT state into the ground-state singlet and triplet wave functions. As in eq 23, one obtains from eqs 16–18, for the ground-state antiferromagnetism (GSAF),

$$-2J^{GS} = \frac{h_{d\pi}^4}{\Delta^2}\left(\frac{1}{U} + \frac{1}{E_{DCT}/2}\right) = \Delta E_{HL}^2\left(\frac{1}{U} + \frac{1}{E_{DCT}/2}\right) \quad (24)$$

and with the ground-state/CT-state mixing coefficient $\lambda = -h_{d\pi}/\Delta$, it follows from eq 23 and eq 24 for

$$\Delta \ll U, E_{DCT}/2$$

$$-2J^{GS} = \lambda^2(-2J^{CT}) \quad (25)$$

Note that, apart from the contribution from the DCT state, this mechanism corresponds to the superexchange pathway invoked for antiferromagnetic dimer coupling in the ground state.[38] For reasonable values of λ (0.1–0.3), ESAF can be 1–2 orders of magnitude larger than GSAF.

In summary, the VBCI model provides a method to calculate CT-state splittings and indicates how these are related to bonding. The magnitude of the splitting of the in-plane $\pi_\sigma^* \rightarrow$ Cu(II) transition is related to the value of the HOMO–LUMO splitting in the particular dimeric complex and thus provides direct information about the strength of the metal-bridging ligand interaction. Second, the VBCI model quantitates CT excited-state antiferromagnetism (ESAF) in terms of configuration interaction with higher-energy MMCT and DCT states. Since ground-state antiferromagnetism (GSAF) derives from mixing of the ground state with the CT-state wave functions subject to ESAF, ESAF is much larger than GSAF and, hence, should greatly affect the excited-state spectrum. This is, in fact, the origin of "dimer" bands which appear in the absorption spectrum of dimers at lower energy than in monomers and were previously assigned to SPE transitions (simultaneous pair excitations).[53] Thus, the study of CT-state splittings and CT excited-state antiferromagnetism provides detailed information regarding the electronic structure of dimers and, in particular, insight into the origin of their magnetic properties.

IV. Electronic Absorption Spectrum of Oxyhemocyanin

In section II, the BS-SCF-Xα-SW calculation of the side-on peroxide-bridged Cu(II) dimer site found in oxyHc has been presented. There are two problems which need to be addressed: (i) the BS-SCF-Xα-SW method does not give CT excited-state splittings (section III), and (ii) the peroxide $\pi_\sigma^* \rightarrow$ Cu(II) CT energies obtained this way are consistently too high (up to 25 000 cm^{-1}) which, as described in the preceding section, is due to a neglect of CT excited-state antiferromagnetism (ESAF). In this section, the CT-state energies of the side-on bridged copper–peroxo dimer are calculated with the VBCI model, compared with the BS-SCF-Xα-SW results and related to the electronic

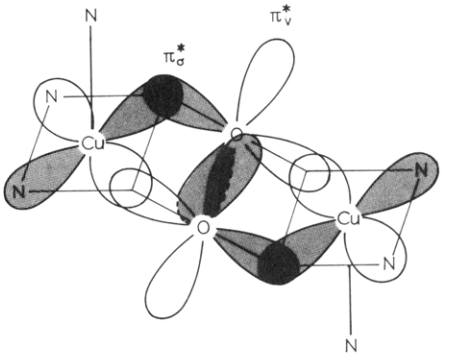

Figure 18. Schematic structure of the side-on peroxide-bridged copper dimer including orbitals involved in bonding.

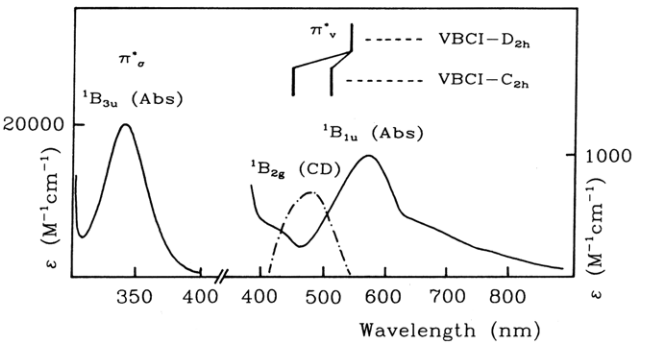

Figure 19. Electronic absorption and CD spectra of oxy-Hemocyanin (busycon) with calculated transition energies in planar (D_{2h}) and nonplanar (C_{2h}) symmetry.

absorption spectrum of the side-on model complex [Cu(HB(3,5-*i*-Pr$_2$pz)$_3$]$_2$(O_2^{2-}) and that of oxyHc.[54]

The valence orbitals of the side-on bridged peroxide model complex are shown schematically in Figure 18. The coordination around each cupric ion is square pyramidal, hence, the dimer is nonplanar. As the apical Cu–N bondlength is elongated with respect to the two others, planar (D_{2h}) dimer symmetry is considered first. With the z axis perpendicular to the Cu–O_2–Cu plane and the x axis parallel to the Cu–Cu vector, the selection rules for the $\pi_v^*(O_2^{2-}) \rightarrow$ Cu(II) LMCT singlet transitions (only the singlets will be spin allowed from the A_{1g} singlet ground state) are $B_{2g}(R_y)$ and $B_{1u}(z)$, and for the $\pi_\sigma^*(O_2^{2-}) \rightarrow$ Cu(II) singlet transitions are A_{1g}-(forbidden) and $B_{3u}(x)$. Hence, four singlet CT states are predicted three of which should contribute to the optical absorption and CD spectrum. The spectrum of oxyHc (Busycon) is presented in Figure 19.[3,55] There are two intense bands in the visible (580 nm; ϵ = 1 000 M^{-1} cm^{-1}) and the UV (350 nm; 20 000 M^{-1} cm^{-1}) region and one CD absorption feature at 480 nm (ΔE = +2.5 M^{-1} cm^{-1}). As all these features are absent in the met derivative [Cu(II)Cu(II)], they are assigned to $O_2^{2-} \rightarrow$ Cu(II) charge-transfer transitions. Since the highest occupied orbital of each copper, $d_{x^2-y^2}$, has two lobes directed to the peroxide ligand (Figure 18), the π_σ^* orbital in the xy plane is expected to be more strongly stabilized than the π_v^* orbital perpendicular to that plane (section II). Therefore, the high-intensity band at 29 000 cm^{-1} is assigned to the $\pi_\sigma^* \rightarrow$ Cu($^1B_{3u}$) CT transition, the low-intensity electric-dipole band at 17 500 cm^{-1} to the $\pi_v^* \rightarrow$ Cu($^1B_{1u}$) CT transition, and the CD feature at 20 500 cm^{-1} not present in the absorption spectrum is assigned as the magnetic dipole-allowed transition $\pi_v^* \rightarrow$ Cu($^1B_{2g}$). The spectrum of the side-on

model complex [Cu(HB(3,5-*i*-Pr_2pz)$_3$](O$_2$) is very similar to that of oxyHc (Figure 12) and the same assignments apply, i.e. the $\pi^*_\sigma \rightarrow$ Cu($^1B_{3u}$) transition is observed at 28 600 cm^{-1} (ϵ = 26 000 M^{-1} cm^{-1}) and the electric dipole allowed $\pi^*_v \rightarrow$ Cu($^1B_{1u}$) transition at 18 600 cm^{-1} (ϵ = 2 000 M^{-1} cm^{-1}) (section II).[43] Due to the lack of optical activity, no CD signal is present.

The VBCI model is now applied to the side-on model complex and oxyHc, respectively. From D_{2h} SCF-Xα-SW transition-state calculations, the transition energies from the ground-state triplet ($^3B_{3u}^{GS}$) to the triplet $\pi^*_\sigma \rightarrow$ Cu(II) CT states are calculated at 62 880 cm^{-1} ($^3A_{1g}^{CT}$) and 71 330 cm^{-1} ($^3B_{3u}^{CT}$), respectively. From eqs 20 and 21, these energies lead to a zeroth-order CT energy Δ of 54 430 cm^{-1} and a transfer integral $h_{d\pi}$ of −23 050 cm^{-1}. In order to evaluate the singlet CT energies, values for the MMCT- and DCT-state energies U and E_{DCT}, respectively, are needed. From photoelectron spectroscopy, U is known to be around 6.5 eV in dimeric copper systems.[56] E_{DCT} is evaluated by SCF-Xα-SW transition-state calculations of two consecutive transitions giving a value of 140 000 cm^{-1} for the side-on bridged dimer. With the use of this set of parameters and eqs 17 and 18, the energies of the two singlet $\pi^*_\sigma \rightarrow$ Cu(II) LMCT transitions are calculated to be 41 060 cm^{-1} ($^1B_{3u}^{CT}$) and 43 780 cm^{-1} ($^1A_{1g}^{CT}$). Compared with the experimental $^1B_{3u}^{CT}$ transition energy of 28 600 cm^{-1}, the VBCI value is still over 10 000 cm^{-1} too large, but represents a significant improvement over the broken-symmetry result of 66 800 cm^{-1}. It has been found that the $\pi^*_\sigma \rightarrow$ Cu(II) LMCT energy in BS-SCF-Xα-SW calculations decreases from 66 800 to 39 300 cm^{-1} by reducing the Cu sphere size from 2.95 to 2.60 bohrs, whereas the $\pi^*_v \rightarrow$ Cu(II) transition energy shows virtually no change.[35] Reducing the copper sphere size would further lower the π^*_σ CT energy. The difference between the BS-SCF-Xα-SW and the VBCI result is due to the inclusion of excited-state antiferromagnetism which amounts to a ~30 000-cm^{-1} stabilization of the singlet in the side-on dimer. Finally, the energy of the $\pi^*_v \rightarrow$ Cu(II) CT transition is calculated at 18 400 cm^{-1} which compares well with experiment. In D_{2h} symmetry, however, no splitting is predicted by the VBCI model as all π^*_v CT states transform as different irreducible representations than the ground and π^*_σ CT states. In order to account for the $\pi^*_v \rightarrow$ Cu(II)-state splitting observed in the electronic spectrum of oxyHc, the analysis has to be based on a more realistic molecular symmetry.

From the nonplanar structure of the side-on peroxo complex (Figure 18), the effective symmetry is C_{2h} with the $z' = C_2$ axis along the O–O vector. Now the peroxide π^*_σ and π^*_v orbitals both transform according to the same irreducible representation, B_g, and each $\pi^*_\sigma \rightarrow$ Cu(II) and $\pi^*_v \rightarrow$ Cu(II) singlet CT state splits into an $A_g(R_{z'})$ and $B_u(x',y')$ component. As a consequence of the square pyramidal N_3O_2 coordination around each copper, the principal axis of each copper center is tilted by ~10° with respect to the Cu–O_2–Cu plane defining π^*_σ and π^*_v (Figure 18). Hence, a nonvanishing matrix element $(h_{d\pi})_v = \sqrt{2}\langle\pi^*_v|h|d_A\rangle$ exists which was zero in D_{2h} symmetry due to the orthogonality of D_A, the Cu $d_{x^2-y^2}$ orbital and the π^*_v orbital. Likewise, the electric dipole transition from π^*_v to d_A which has been allowed group theoretically for the B_{1u} component in D_{2h} symmetry (parallel to z), but in fact had zero intensity in D_{2h} symmetry due to the orthogonality of π^*_v and d_A, gains intensity in C_{2h} to the extent that the copper centers are tilted with respect to the Cu–O_2–Cu plane. We make the approximation that the transition moments $\langle d_A|\mu|\pi^*\rangle$ are proportional to the transfer matrix elements $h_{d\pi}$, i.e.

$$\frac{\langle d_A|\mu|\pi^*_v\rangle}{\langle d_A|\mu|\pi^*_\sigma\rangle} = \frac{(h_{d\pi})_v}{h_{d\pi}} \tag{26}$$

From the oscillator strengths of the π^*_σ and π^*_v transitions, one obtains a ratio of 1:3.5 for the left side of eq 26 and, with $h_{d\pi}$ = 23 050 cm^{-1}, a value of −6 600 cm^{-1} is obtained for $(h_{d\pi})_v$. The zeroth-order CT energy Δ_v for the π^*_v transition is determined by moving one electron from π^*_v to the HOMO starting from the triplet ground state, giving a value of Δ_v = 7 700 cm^{-1} (section III). Now the secular determinants, eqs 17 and 18, including the ^1B_u and ^1A_g components of the π^*_v LMCT states, can be solved. Note that via the matrix element $(h_{d\pi})_v$ the $^1A_g(\pi^*_v)$ CT state interacts with both the ^1A_g ground and the ^1A_g MMCT state, whereas the $^1B_u(\pi^*_v)$ state interacts only with the ^1B_u MMCT state. Further, there is no interaction between the π^*_σ and π^*_v LMCT states as the matrix element $\langle\pi^*_\sigma|h|\pi^*_v\rangle$ vanishes. Finally, the DCT states with two electrons removed from π^*_v or one from π^*_σ and π^*_v are neglected as their energy is high compared to the off-diagonal matrix element. Solving the secular determinants for ^1A_g and ^1B_u gives the following optical transition energies (see Figure 19): $^1B_u(\pi^*_v)$, 19 520 cm^{-1}; $^1A_g(\pi^*_v)$, 22 410 cm^{-1}; $^1B_u(\pi^*_\sigma)$, 44 330 cm^{-1}; $^1A_g(\pi^*_\sigma)$, 46 250 cm^{-1}. The calculated π^*_v-state splitting (2 900 cm^{-1}) is in good agreement with the observed value (3 000 cm^{-1}).

In summary, the VBCI model combined with SCF-Xα-SW molecular orbital calculations allows an understanding of the spectral features and the electronic structure of oxyhemocyanin. The side-on binding mode results in a strong interaction between peroxide and copper as reflected by the very large value of the transfer matrix element and the huge stabilization of the π^*_σ orbital. Both parameters are calculated to be larger than in the *trans*-μ-1,2-peroxo-bridged Cu dimer. The large value of the transfer element corresponds to a strong donation of electron density into the copper orbitals making the side-on bridging O_2^{2-} the least negative within the Cu–peroxo series (section II).[35] The VBCI model also predicts a very strong antiferromagnetism in the CT excited state which lowers the observed CT energy by over 25 000 cm^{-1} from the value predicted by BS-SCF-Xα-SW transition-state calculations. This excited-state antiferromagnetism (ESAF) is transferred into the ground state by mixing between the CT and ground-state wavefunctions, giving an estimate for the ground-state coupling constant $-2J^{GS}$ of 2 500 cm^{-1} which is 1 order of magnitude smaller than ESAF (only a lower limit of $-2J^{GS} > 600$ cm^{-1} was obtained from SQUID susceptibility measurements).[43] The splitting of the $\pi^*_v \rightarrow$ Cu(II) LMCT transition reflects the interaction of π^*_v orbital with the Cu $d_{x^2-y^2}$ orbitals due to the nonplanarity of the dimer. Since the energy gap between the π^*_v orbital and the highest energy d

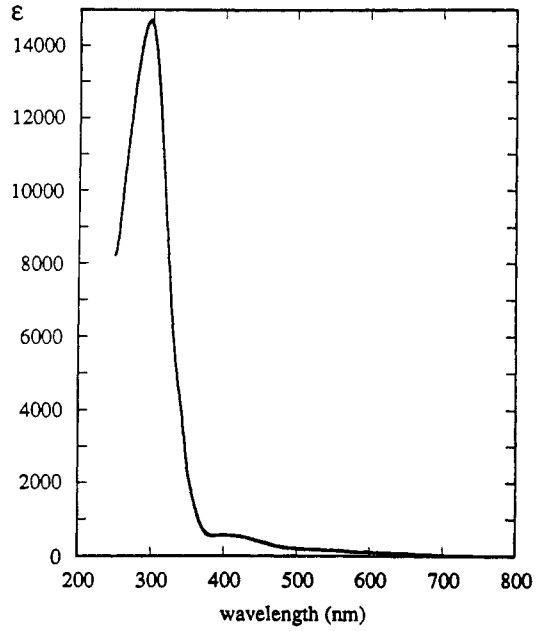

Figure 20. Glass absorption spectrum of [(en)(dien)Co(O_2)-Co(en)(dien)]$^{4+}$ at 78 K.

orbitals of the copper centers is small, a relatively small distortion causes a relatively large splitting (3000 cm^{-1}) of the $\pi_v^* \rightarrow$ Cu(II) LMCT states.

V. Electronic Absorption Spectrum of Co(III) Dimers: Comparison to Cu(II) Dimers

Cobalt–peroxo systems comprise a large number of structurally characterized monomers as well as *cis*- and *trans*-μ-1,2-peroxo- and μ-1,1-hydroperoxo-bridged dimers.[21,57] The variety of O_2^{2-} binding modes allows a systematic comparison of the spectral properties of the different cobalt–peroxo species which is of interest with respect to an understanding of electronic-structural factors influencing oxygen binding and activation, photochemical properties, and, in particular, a comparison to the spectroscopic and chemical properties of the analogous copper–peroxo systems. A number of spectroscopic investigations have been carried out on *cis*- and *trans*-μ-1,2-cobalt–peroxo complexes[58-64] and their electronic and spectroscopic properties have been reviewed.[2,65] However, band assignments have been based on solution spectra, and no complete picture of ligand-field and charge-transfer spectra has been achieved. Therefore, we have performed a single-crystal polarized absorption study of the electronic structure of *trans*-μ-1,2-peroxo binuclear cobalt complexes.[26]

Figure 20 shows the solution spectrum of [(en)(dien)-Co(O_2)Co(en)(dien)]$^{4+}$ at 78 K. The dominant feature is a band at 300 nm ($\epsilon \approx 14\,000$ M^{-1} cm^{-1}). Much less intense ($\epsilon < 500$ M^{-1} cm^{-1}) bands are observed at 400 and 550 nm. From overlap and energy considerations, the 300-nm band is assigned to the $\pi_\sigma^* \rightarrow$ Co CT transition.[2] This assignment is supported by the Raman preresonance enhancement of the 800-cm^{-1} O–O stretching vibration. As indicated in previous sections, a second, less intense CT transition from the peroxide π_v^* orbital is expected at lower energy. However, the plot[26] of the frequency-corrected Raman intensity $I^{1/2}$ against the Shorygin function A[66] in Figure 21 shows only a straight line corresponding to an Albrecht A

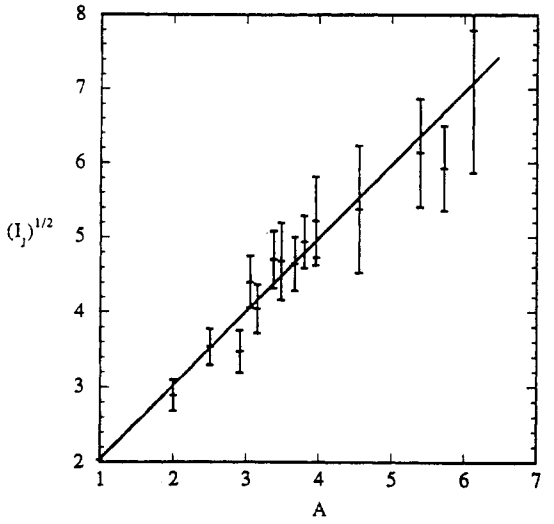

Figure 21. Plot of the square root of the intensity of the O–O stretch vs the Shorygin function for a *trans* 1,2 cobalt–peroxo dimer.

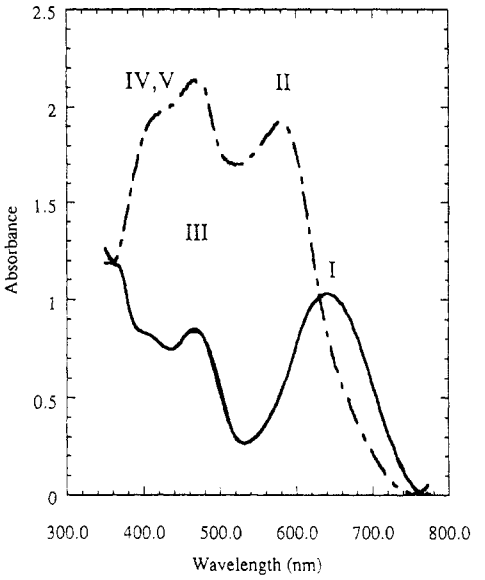

Figure 22. Single-crystal polarized absorption spectra of $[Co_2(NH_3)_{10}](SCN)_4$ along [001] (solid) and [110] (dot–dash) directions.

term enhancement[67] of ν_{O-O} with respect to the 300-nm band, i.e. there is no indication of a second peroxide $\rightarrow$ Co CT transition. The position of the $\pi_v^* \rightarrow$ Co CT transition was then determined through single-crystal, polarized absorption measurements of various *trans*-μ-1,2-peroxo-bridged cobalt dimers.

Figure 22 presents the polarized single-crystal spectra of the orthorhombic system $[(NH_3)_5Co(O_2)Co(NH_3)_5](SCN)_4$ with $\mathbf{E} \parallel [001] = c$ (along the needle axis; solid line) and $\mathbf{E} \parallel [110]$ (perpendicular to the needle axis; dot–dash line). If the molecular coordinate system is chosen such that Z is perpendicular to the Co–O_2–Co plane and X parallel to the Co–O bond (Figure 23), one can determine from the X-ray structure that the crystal spectra along [001] and [110] are given by

$$\epsilon_{[001]} = 1.00\epsilon_Z \qquad (27)$$

$$\epsilon_{[110]} = 0.55\epsilon_X + 0.45\epsilon_Y$$

in terms of spectra along the molecular axes X, Y, and Z. Figure 22 shows that five bands can be identified

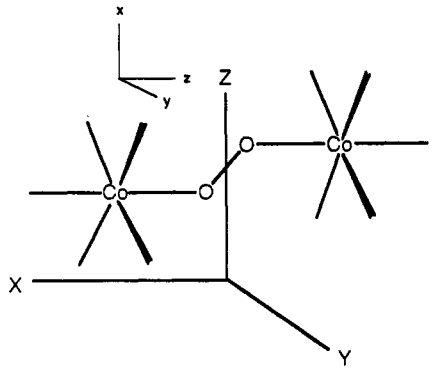

Figure 23. Coordinate frame for *trans*-O_2^{2-}-Co dimer systems.

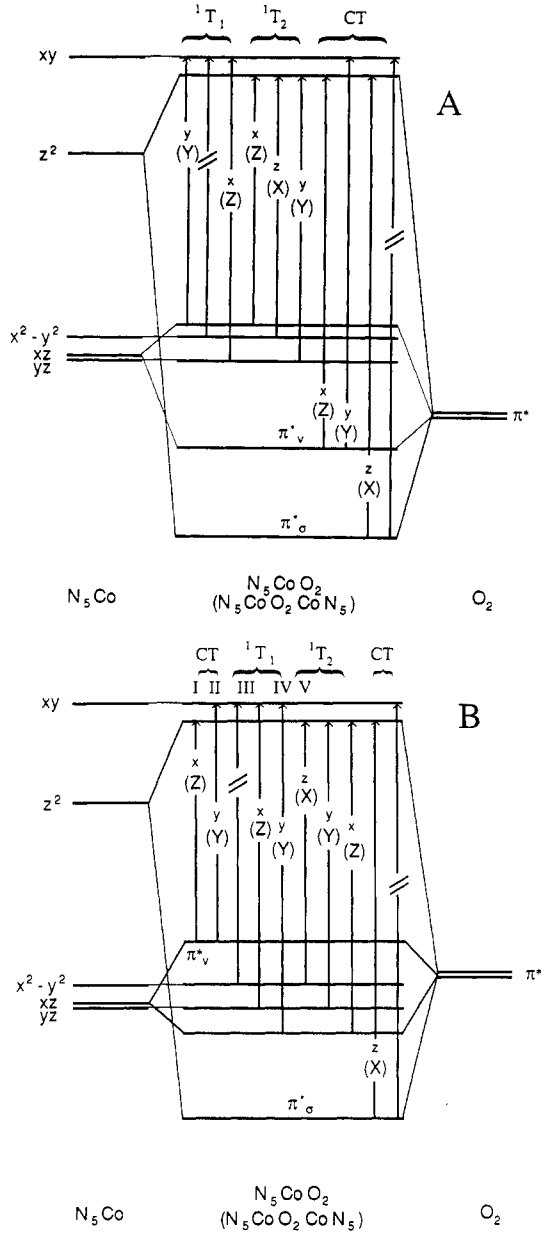

Figure 24. (A) Bonding scheme of cobalt–peroxo complexes with $\pi^*(O_2^{2-})$ lower in energy than the metal t_{2g} orbitals, polarizations in monomer (lowercase) and dimer (uppercase). Part B shows the bonding scheme for the same complexes with $\pi^*(O_2^{2-})$ higher in energy than the metal t_{2g} orbitals.

in the visible part of the spectrum which are denoted by I–V. Importantly, band I, the lowest energy band, is *Z* polarized. Figure 24 presents two possible bonding schemes to account for the spectral properties of cobalt–peroxo systems. If the π^*_v orbital is assumed to be at lower energy than the manifold of cobalt t_{2g} orbitals (Figure 24A), a π-antibonding interaction is anticipated to occur between π^*_v and $d_{x^2-y^2}$ of each cobalt center (for the definition of *x*,*y* see Figure 23), and the lowest ligand field transition is expected to be $d_{x^2-y^2} \rightarrow d_{xy}$ which is *Y* polarized. A possible candidate for a *Z*-polarized transition within this bonding scheme would be $d_{x^2-y^2} \rightarrow d_{z^2}$ which, however, derives from the octahedral $^1A_1 \rightarrow {}^1T_2$ transition and is expected to be at much higher energy. Hence, the bonding in Figure 24A is excluded by the experimental result and the energetic sequence between π^*_v and the cobalt t_{2g} orbitals has to be reversed, i.e. π^*_v must be at higher energy than the metal t_{2g} manifold (Figure 24B). In this alternative bonding description, band I is assigned to $\pi^*_v \rightarrow d_{z^2}$ (*Z* polarized). Note that this indicates that the HOMO of binuclear *trans*-μ-1,2-peroxide-bridged cobalt complexes is not of metal, but of ligand (O_2^{2-}) character. A consistent assignment of the remaining bands II–V has further been achieved within Figure 24B (Table 1) by comparing the polarized single-crystal absorption spectra of five structurally characterized *trans*-μ-1,2-peroxo–cobalt systems. In particular, band II was found to be $\pi^*_v \rightarrow d_{xy}$, i.e. a second component of the $\pi^*_v \rightarrow$ Co CT transition, and bands III–V were assigned to d–d transitions.

Table 1

band	energy range, nm	polarization	assignment
I	660–750	*Z*	$\pi^*_v \rightarrow z^2$
II	590–500	*Y*	$\pi^*_v \rightarrow xy$
III	500–475	*X*,*Y*	$x^2-y^2 \rightarrow xy$
		Z	$yz \rightarrow xy$
IV	420–435	*Y*	$xz \rightarrow xy$
V	415–440	*X*	$x^2-y^2 \rightarrow z^2$
	300	*X*	$\pi^*_\sigma \rightarrow z^2$

Each of the transitions mentioned so far splits into a *g* and an *u* combination in the dimer as described in section III. Denoting the C_{2h} dimer states with Ψ, monomer wave functions with $\phi(1)$ and $\phi(2)$, respectively, and excited state wave functions with a prime, one obtains for the *g* ground and *g*,*u* excited states of the *trans*-μ-1,2-peroxide-bridged dimer

$$\Psi_g = \varphi(1)\,\varphi(2)$$

$$\Psi_g' = \varphi'(1)\,\varphi(2) + \varphi(1)\,\varphi'(2) \qquad (28)$$

$$\Psi_u' = \varphi'(1)\,\varphi(2) - \varphi(1)\,\varphi'(2)$$

The total transition dipole moment **M** is given in terms of monomer transition dipole moments $\mathbf{M}_1$ and $\mathbf{M}_2$ from the peroxo ligand to the 1 and 2 by

$$\mathbf{M}_+ = \langle \Psi_g|\vec{\mu}|\Psi_g'\rangle = \langle \varphi(1)|\vec{\mu}|\varphi'(1)\rangle + \langle \varphi(2)|\vec{\mu}|\varphi'(2)\rangle = \mathbf{M}_1 + \mathbf{M}_2 = 0$$

$$\mathbf{M}_- = \langle \Psi_g|\vec{\mu}|\Psi_u'\rangle = \langle \varphi(1)|\vec{\mu}|\varphi'(1)\rangle - \langle \varphi(2)|\vec{\mu}|\varphi'(2)\rangle = \mathbf{M}_1 - \mathbf{M}_2 = 2\mathbf{M}_1 \quad (29)$$

Only the transitions from the g ground state to the u excited state are electric dipole allowed and thus no LF

or CT excited-state splittings can be observed in the optical spectra of *trans*-μ-1,2-systems.

In summary, the investigation of the *trans*-μ-1,2-peroxo–cobalt systems have indicated a strong stabilization of the peroxide ligand as reflected by the large value of the $\pi_v^* - \pi_\sigma^*$ splitting (17 000 cm^{-1}). This stabilization is due to good overlap and a strong σ-bonding interaction between the peroxide π_σ^* and the Co d_{z^2} orbitals. The ligand field bands III–V are typical of low-spin Co(III) systems and reflect the coordination to a ligand with one π orbital perpendicular to the Co–O_2–Co plane. The $\pi_v^* \rightarrow$ Co transitions appear at lower energy than the ligand field bands indicating that the HOMO in the *trans*-μ-1,2 cobalt–peroxo complexes has ligand π_v^* character. It is of interest to compare the spectroscopic and electronic properties of the *trans*-μ-1,2 cobalt–peroxo to those of the analogous copper *trans*-μ-1,2-peroxo system $[\{Cu(TMPA)\}_2(O_2)]^{2+}$ which has been described in section II. These are two striking differences in the peroxide $\rightarrow$ metal CT spectra: (i) whereas the intensity of the $\pi_v^* \rightarrow$ Co transition is small and comparable to those of the LF transitions ($\epsilon \sim 100$ M^{-1} cm^{-1}), the intensity of the $\pi_v^* \rightarrow$ Cu transition is nearly 2 orders of magnitude higher ($\sim$6 000 M^{-1} cm^{-1}) and comparable to that of the $\pi_\sigma^* \rightarrow$ Cu(II) transition (12 000 M^{-1} cm^{-1}). (ii) The separation between the spin-allowed π_v^* and π_σ^* CT bands is 17 000 cm^{-1} for the cobalt complex (*vide supra*) and only 2 600 cm^{-1} for the copper complex. The first difference is due to a distortion of the copper coordination away from regular trigonal bipyramidal symmetry, whereas the cobalt systems have a coordination close to regular octahedral around the metal centers. This distortion leads to a nonzero overlap of d_{z^2}(Cu) with π_v^* and causes the high intensity of the $\pi_v^* \rightarrow$ Cu(II) CT transition. The second difference is related to the fact that Co(III) ions are closed subshell systems, whereas Cu(II) centers have one unpaired electron which, in the CT state, may couple with an unpaired electron in the bridging ligand orbital causing a large energy depression of the (singlet) CT state (excited-state antiferromagnetism, section III). In terms of the VBCI model (section III), ESAF is described by configuration interaction of the CT with a MMCT state which requires an additional (virtual) transition from a Cu(II) center to the ligand resulting in a Cu^+–Cu^{3+} (d^{10}–d^8) final configuration. In the case of the Co(III) systems, this transition is expected to be at much higher energy as one electron has to be removed from the $(t_{2g})^6$ configuration. In addition, the Co^{2+}–Co^{4+} configuration would be high spin and cannot act to lower the energy of the singlet CT state.

Spectra of doubly bridged μ-hydroxo- or μ-amido *cis*-μ-1,2-peroxo–cobalt compounds (Figure 25) are very different from those of the singly bridged *trans*-cobalt dimer systems as now two intense UV bands at 290 and 350 nm ($\epsilon \approx 6\,000$ M^{-1} cm^{-1}) are observed.[2,65,68] From SCF-Xα-SW calculations on *trans* mono and *cis* dibridged copper–peroxide systems,[35] the different coordination should not strongly affect the π_σ^* and π_v^* orbital energies. In the dibridged systems, however, additional CT transitions are expected from the bridging hydroxo or amido ligands to the metal, and these systems are known to be severely distorted with Co–O–O–Co dihedral angles of around 60°.[21,57] Due to this distortion, the Co d_{z^2} orbitals have a reduced overlap

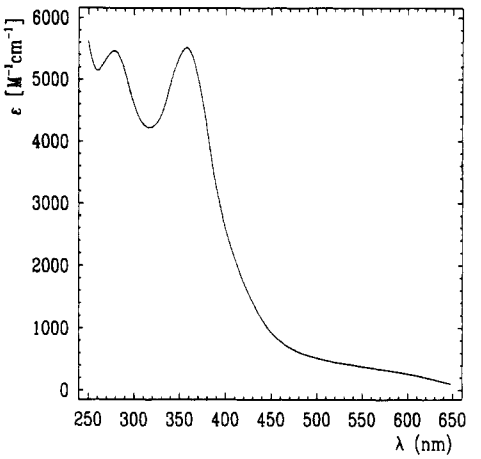

Figure 25. Spectra of doubly bridged *cis*-μ-1,2-O_2^{2-} binuclear Co(III) systems.

with $\pi_\sigma^*(O_2^{2-})$, but a nonvanishing overlap with $\pi_v^*(O_2^{2-})$, i.e. π_σ^* becomes less σ bonding than in the *trans* systems and π_v^* gets some σ-bonding character. As a consequence, the π_σ^* and π_v^* transitions should approach each other in energy. The 290- and 350-nm bands have been assigned to O_2^{2-} $\pi_\sigma^* \rightarrow$ Co and $\pi_v^* \rightarrow$ Co CT transitions,[2,65] but as has been pointed out,[68] the shift of the $\pi_\sigma^* \rightarrow$ Co CT transition from 300 nm in the *trans* systems to higher energy is not consistent with the above bonding description. Moreover, the donation of electron density from the second bridging ligand (OH^-, NH_2^-) to the Co(III) atoms is expected to decrease the amount of charge donation from the peroxide and, hence, the stabilization of π_σ^* leading to a further decrease of the $\pi_\sigma^* \rightarrow$ Co transition energy. An alternative assignment of the 290-nm band is an hydroxo or amido $\rightarrow$ Co charge-transfer transition and the 350-nm band is a superposition of the π_σ^* and π_v^* Co CT transitions. This would, however, require that the hydroxo $\rightarrow$ Co and the amido $\rightarrow$ Co CT transitions appear at the same energy. Finally, the $\pi_\sigma^* \rightarrow$ Co CT transition should split into two transitions in the dimer as described in section III with both transitions being electric dipole allowed in a *cis*-μ-1,2 geometry. Thus, the 290-nm band could correspond to the higher energy component of $\pi_\sigma^* \rightarrow$ Co CT transition and the 350-nm band to the lower energy compartment of $\pi_\sigma^* \rightarrow$ Co or a superposition of π_σ^* and $\pi_v^* \rightarrow$ Co CT transitions.

Assignment of the lowest energy band (band I) in the spectra of the *trans*-μ-1,2 cobalt–peroxo complexes to $\pi_v^* \rightarrow$ Co has important implications with respect to the photochemistry of cobalt–peroxo systems. Thus, the yield of photoinduced deoxygenation is wavelength independent in the range of 300–550 nm for the *trans*-μ-1,2 systems which was interpreted as being due to a low-lying photoactive state at $\lambda > 550$ nm[69] which, from our polarized data, has to be the $\pi_v^* \rightarrow$ Co LMCT state. In contrast, the doubly bridged systems show a clear correlation of the rate of dioxygen release with the band at 290 nm. The presence of a second bridge in addition to peroxide also has implications on the reactivity of the cobalt–peroxo species. The oxygen affinity of the dibridged systems has been shown to be in general smaller than of the monobridged systems[70] which is understandable in terms of the reduced stabilization of the π_σ^* level in the presence of a second bridge (*vide*

supra). Differences in stability of the *cis*-μ-1,2 dibridged systems are mainly due to the nature of the second bridge: whereas the μ-amido systems are quite stable even in acid solution, the μ-hydroxo bridge is hydrolyzed in acid solution to give a single-bridged species which decomposes rapidly to 2Co(II) ions and O_2. It should be noted that the instability of the monobridged complexes in acid solution does not arise from protonation of the bound peroxide which, on the contrary, stabilizes the complex,[71] but rather from dissociation and protonation of the free ligands (e.g. NH_3). The protonated form of the *cis*- or *trans*-μ-1,2-peroxide bridge is in equilibrium with the μ-1,1-hydroperoxo species which appears as an intermediate in reactions involving oxygen transfer and further reduction to water. It has been shown[72] that the μ-1,1-hydroperoxo–cobalt species generated in the reduction of *trans*-μ-1,2-superoxo–cobalt systems with metals (Fe^{2+}, Cr^{2+}, V^{2+}, Eu^{2+}) decays to Co^{2+} ions and O_2 at a rate which is inversely proportional to $[H^+]$ which indicates that peroxide is stabilized in the μ-1,1-hydroperoxo binding mode toward loss as O_2. Alternatively, it has been demonstrated that the essential step in the chloride- or bromide-catalyzed disproportionation of μ-peroxo–μ-amido–cobalt systems is the attack of Cl^- (or Br^-) on the μ-amido–μ-1,1-hydroperoxo intermediate leading to the μ-OH–μ-NH_2 complex and HOCl (or HOBr);[73] the same mechanism is involved in the reduction of peroxo cobalt(III) complexes with iodide.[74] The higher reactivity of the μ-1,1 as compared to the *cis*- or *trans*-μ-1,2 bonding mode toward oxygen transfer and further reduction could be due to contributions from both structural and electronic factors, i.e. the easier attack of a substrate on the O–O bond oriented perpendicular to the Co–Co axis and the polarization of this bond induced by the asymmetric coordination.

In summary, the spectral features of μ-1,2 cobalt–peroxo systems are consistent with a description of a Co^{3+}–O_2^{2-}–Co^{3+} unit with a large amount of charge delocalization (stabilization) of the bound peroxide toward the metals. This is reflected in the large number and high stability of peroxo–cobalt complexes. In comparison, the *trans*-μ-1,2-peroxo binuclear copper(II) system is much less stable as peroxide is bound to divalent metals and the amount of charge donation of peroxide is smaller. In order to activate dioxygen toward oxygenation and further reduction, cobalt–peroxo chemistry requires rearrangement to the μ-1,1-hydroperoxo binding mode. This appears to be related to the binding of dioxygen as end-on hydroperoxide in the multicopper oxidases (e.g. laccase) which catalyzes the four-electron reduction of dioxygen to water.[75]

VI. Electronic Absorption Spectra of Met- and Oxyhemerythrin: Nature of the μ-Oxo and Hydroperoxo–Fe(III) Bond

The interaction of binuclear iron proteins with dioxygen has the focus of much recent work in bioinorganic chemistry.[76-79] The first known binuclear non-heme iron protein system to bind oxygen was oxyHr which was structurally characterized in 1985.[80] The electronic structure of met and oxyHr are the subject of this section. It should also be noted that there has been recent work in the synthesis and characterization of non-heme iron–peroxo model complexes.[81,82]

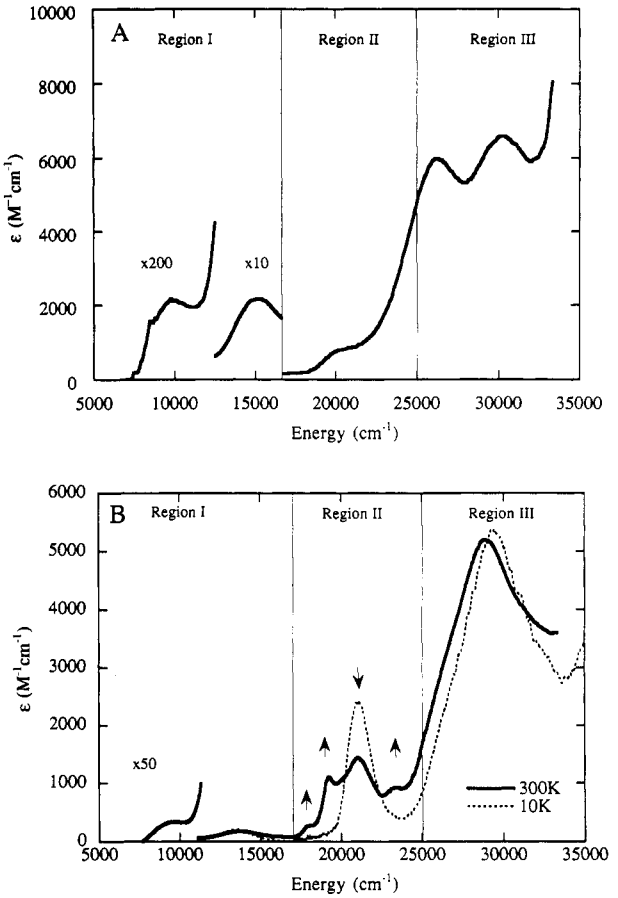

Figure 26. (A) Room-temperature absorption spectrum of metCl⁻ Hr and (B) room-temperature and low-temperature (10 K) absorption spectra of the tribridged model complex.

A. The Fe^{III}–O–Fe^{III} Bond

In addition to the peroxo–Fe^{III} bond, oxyHr contains an Fe^{III}–O–Fe^{III} core (Figure 1B). It is important to understand the electronic structure of the Fe^{III}–O–Fe^{III} unit that dominates the bonding in this site. MetHr, i.e. the binuclear ferric form which also contains the Fe^{III}–O–Fe^{III} unit, binds small anions to one Fe(III). The room temperature absorption spectrum of the metCl⁻ derivative (Figure 26A) exhibits the distinctive spectral features which are associated with the Fe^{III}–O–Fe^{III} unit. These include d–d or ligand-field (LF) bands that are orders of magnitude more intense than are found for ferric monomers[83] and new intense low-energy bands which were originally thought to be simultaneous pair excitations (SPE) transitions.[14] SPE transitions correspond to LF transitions occurring simultaneously on both irons of the dimer which are coupled through the exchange interaction to give one transition at twice the single-ion transition energy. It has been shown that these bands should, in fact, be assigned to oxo → Fe charge-transfer transitions[17] which are at unusually low energy. Model complexes containing the Fe^{III}–O–Fe^{III} unit exist which have been the subject of numerous studies.[76,79,84,85] The model complex $[Me_3Tacn(OAc)Fe]_2O$,[86] based on its ideal orientation in the unit cell, has been studied in great detail using a combination of spectral techniques. Hereafter it will be referred to as the tribridged structure. The room-temperature and low-temperature glass spectra shown in Figure 26B are very similar to those of metHr and have been divided into three regions. Note that the features in region II are resolved into a number of

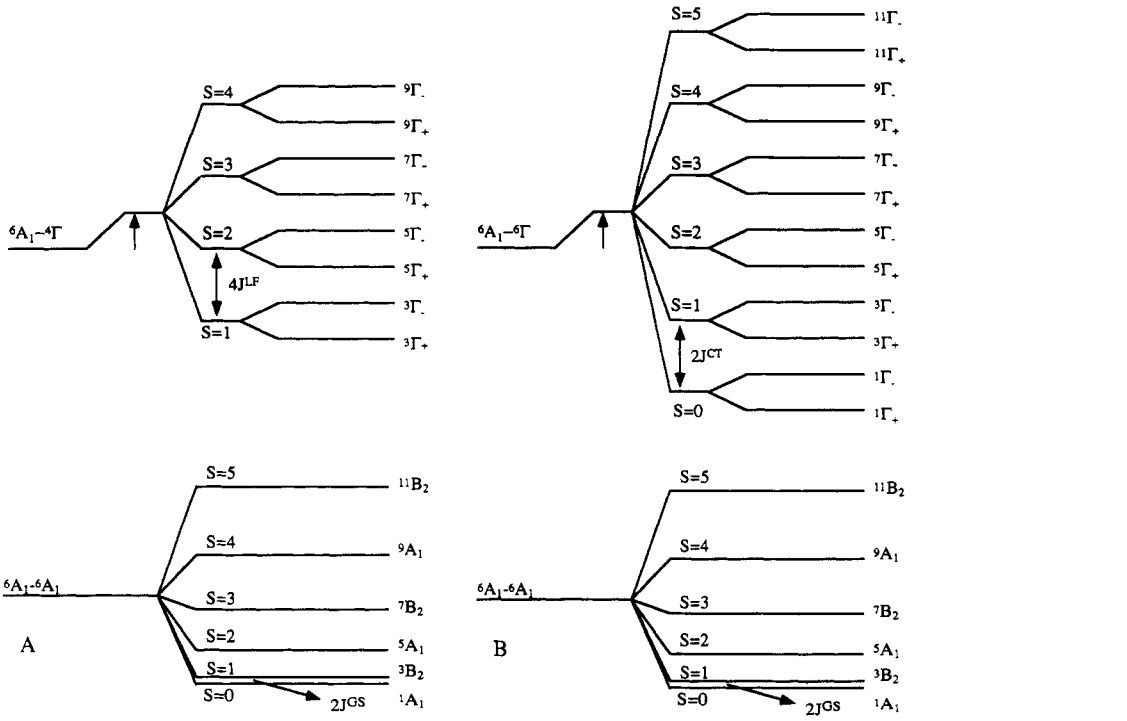

Figure 27. (A) Energy-level splittings for GS and spin-forbidden LF excited states in the dimer and (B) energy-level splitting for GS and spin-allowed CT excited states in the dimer.

components which show a striking temperature dependence. For a correlation of the absorption spectrum with the Fe–O–Fe angle, data for a single oxo-bridged complex, $[(HEDTA)Fe]_2O$, hereafter called the mono-bridged structure, with an angle of 165° [87] has been analyzed and, where necessary, will be used to aid in the description of these systems. Also to gain further insight into the Fe–oxo bond, BS-SCF-Xα-SW calculations have been performed on idealized geometries based on both structures.

These model complexes, which are both antiferromagnetically coupled, reproduce the ground-state magnetic properties of metHr. The bridging oxo with its short Fe–O distance of 1.8 Å is the dominant pathway for superexchange in these systems. Upon formation of the dimer, the ground state splits into six total spin states due to antiferromagnetic coupling of two $S = {}^5/_2$ monomers to give $S_{Total} = 0, 1, 2, 3, 4, 5$ states of the spin ladder shown in the bottom half of Figure 27, parts A and B. The splitting is governed by the ground state J^{GS}. The symmetry of the states can be obtained using a group theoretical technique which involves coupling the two C_{4v} monomers.[88] Transitions will be observed only from thermally populated components of the ground state, and, from a Boltzmann analysis of the ground spin states using a J^{GS} of -120 cm^{-1}, which is the experimentally determined ground-state exchange value for the tribridged structure,[86] only the singlet, triplet, and quintet sublevels of the ground state are significantly populated at 300 K.

The excited-state absorption spectrum of the ligand-field and oxo $\rightarrow$ Fe^{3+} charge-transfer transitions is a direct probe of the iron–oxo bond and also offers insight into the efficiencies of the specific orbital superexchange pathways in both the ground and excited states (*vide infra*). First we consider the LF transitions. All LF transitions of high-spin d^5 ions, $^6A_1 \rightarrow {}^4\Gamma$ ($\Gamma = T_1, T_2, A_1, E$), are spin forbidden, and the energy ordering of predicted transitions are given by the weak field

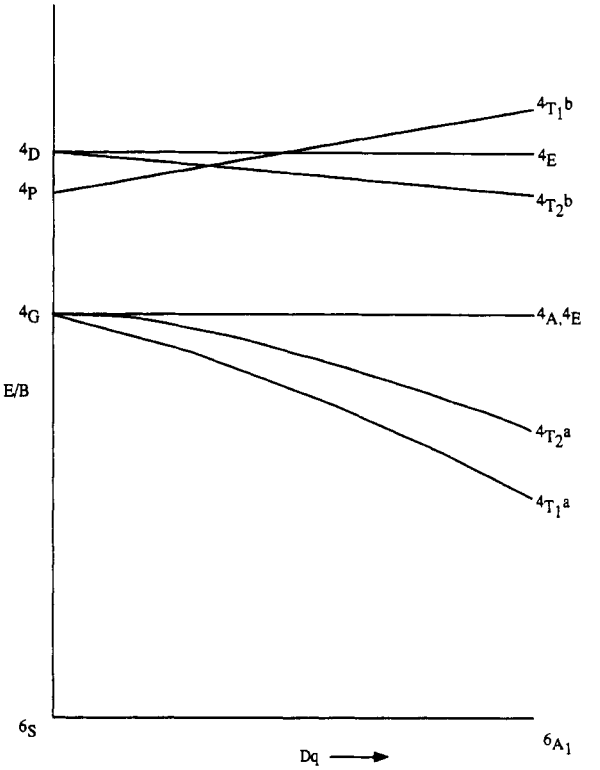

Figure 28. Tanabe–Sugano diagram for high spin d^5.

Tanabe–Sugano diagram[89] for d^5 in Figure 28. In Figure 27A are the LF states of the dimer obtained when one ion undergoes a quartet ligand-field transition resulting in a complex that has an $S = {}^5/_2$ (ground state) ion on one side of the dimer and an $S = {}^3/_2$ (excited state) ion on the other side. These spins couple leading to four spin states ($S_{Tot} = 1, 2, 3, 4$) with an energy splitting described by an excited state J^{LF} value. In the excited state, a matrix element exists that can transfer the excitation to the other side of the dimer leading to a symmetric (+) and antisymmetric (−) splitting of each

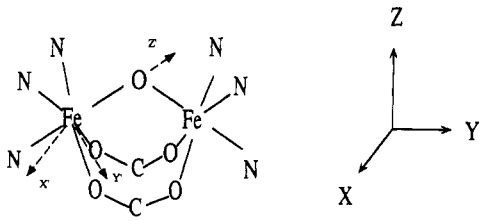

Figure 29. Coordinate frame for the tribridged model complex.

spin component in the excited state yielding a total of eight possible transitions in the dimer for each monomer ligand-field transition, with the symmetry of the dimer states dependent on the specific single ion excited-state denoted by Γ (Figure 27A, top). As presented in section III a similar interaction also occurs for charge-transfer transitions yielding energy splittings of excited total spin states. Since charge-transfer transitions for d^5 systems are spin allowed, in the excited state of the dimer both of the irons will have spins of $^5/_2$. Coupling these spins yields the same S_{Tot} values obtained in the ground state (S_{Tot} = 0, 1, 2, 3, 4, 5) but again antisymmetric and symmetric combinations of these transitions yields a total of 12 possible excited states as given in Figure 27B, top. With significant excited-state antiferromagnetism of the oxo → Fe(III) CT transitions, the singlet transitions will be stabilized in energy and thus accessible in the UV/vis absorption spectrum.

Focusing on the lower energy ligand-field transitions, the glass spectra in Figure 26B show two broad transitions centered at 9 500 and 13 500 cm^{-1} which can be assigned to the lowest energy predicted octahedral LF transitions. Inspection of the Tanabe–Sugano diagram in Figure 28 indicates that these transitions are the $^6A_1 \rightarrow {}^4T_1$ and $^4T_2$ transitions, respectively. The $^4T_2$ transition is ~20 times more intense than the $^6A_1 \rightarrow {}^4T_1$ transition. To probe these transitions in greater detail, single-crystal polarized electronic absorption data were obtained, and the coordinate frame and core atoms for tribridged structure is shown in Figure 29. Z is along the C_2 axis which is perpendicular to the Fe–Fe axis (i.e. in plane polarization), Y is along the Fe–Fe axis (i.e. parallel polarization), and X is perpendicular to the Fe–O–Fe plane (i.e. out of plane perpendicular polarization). (Also included in Figure 29 is a primed coordinate frame for each Fe center which orients the z' axis along the Fe–O bond and x' and y' bisecting the metal–ligand bonds.) The single-crystal polarized absorption spectra of the $^4T_1$ transition for the tribridged structure are shown in Figure 30 along with their temperature dependence. Figure 30 gives two Y-polarized bands at 8 000 cm^{-1} and 9 500 cm^{-1} with ϵ = 7 and 12 M^{-1} cm^{-1} at low temperature with the higher energy band increasing in intensity with increasing temperature. There is no X-polarized intensity and only a weak broad Z-polarized band which is temperature independent. The $^4T_1$ region for monobridged structure is very similar.[27] The $^4T_2$ transition intensity exhibits little temperature dependence and thus only the low-temperature polarized absorption spectrum is shown in Figure 31, which demonstrates that the predominant polarization is along the Fe–Fe vector **Y** with an ϵ value > 400 M^{-1} cm^{-1}. The equivalent transition in the monobridged structure is shifted to higher energy and overlaps with other

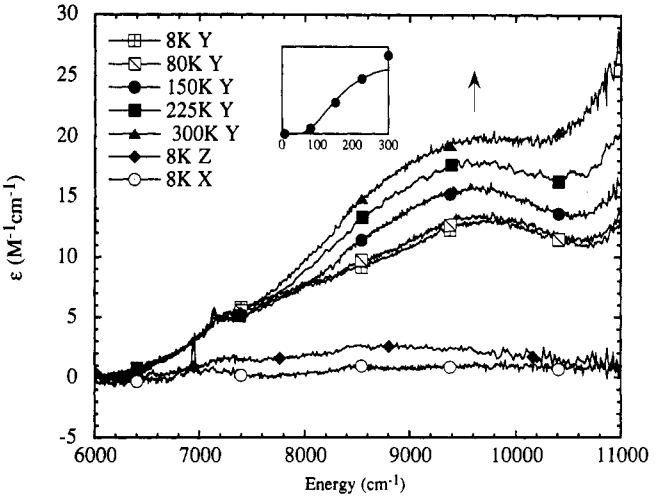

Figure 30. Single-crystal polarized absorption spectra for the $^4T_1$ transition in the tribridged structure. Inset shows a fit of intensity to the Boltzmann population of the S = 1 component of the GS.

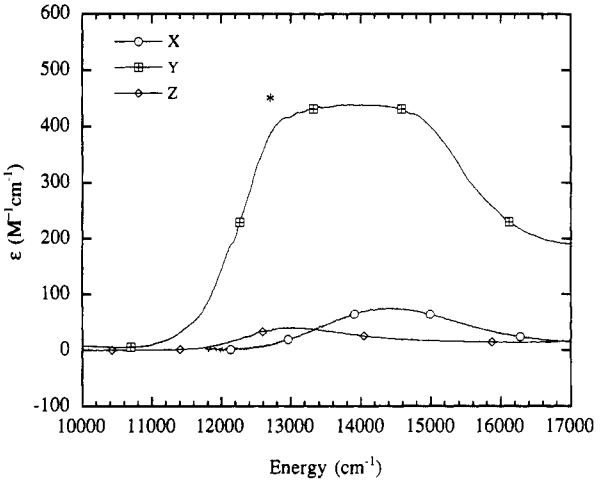

Figure 31. Single-crystal polarized absorption spectra for the $^4T_2$ transition in the tribridged structure. [The asterisk (*) denotes that the peak is intense but distorted due to stray light effects.]

transitions,[27] but it is also temperature independent and parallel polarized.

There are several important features to note in these lowest energy ligand-field transitions of the Fe^{III}–O–Fe^{III} moiety. First, the intensity of these transitions is at least 1 order of magnitude greater than what is found for spin-forbidden, Laporté-forbidden octahedral monomer ligand field transitions.[83] Also, almost all of the intensity is polarized along the Fe–Fe vector. Finally one should note the temperature dependence of the these transitions with the $^4T_1$ increasing in intensity by a factor of 2 with increasing temperature and the $^4T_2$ exhibiting less temperature dependence.

There are two intensity mechanisms that can be effective for electronic transitions in a dimer.[90,91] The first mechanism involves thermal population of higher spin components of the ground state which then undergo spin-allowed transitions, i.e. population of the $^3B_2$ component 240 cm^{-1} above the ground state in the tribridged structure in Figure 27A can lead to a spin-allowed transition to the S_T = 1 (triplet) components of these ligand-field excited states. However, this mechanism cannot account for the high intensity observed at low temperature. The second intensity

mechanism involves spin–orbit (SO) coupling which overcomes the spin forbiddenness of transitions and is generally present for monomers with spin-selection rules of $\Delta S = 0, \pm 1$.[92,93] This mechanism can account for the low-temperature intensity observed in Figures 30 and 31; however, this intensity in the Fe–O–Fe dimer is 1 order of magnitude higher than that in the monomer. The spin–orbit matrix elements[94] which describe this process are

$$\langle {}^6A_1 M_s | M_q | {}^4\Gamma h M_{s'} \rangle = \frac{\langle {}^6A_1 M_s | H_{SO} | {}^4T_1 h' M_{s'} \rangle \langle {}^4T_1 h' M_{s'} | M_q | {}^4\Gamma h M_{s'} \rangle}{[E({}^4T_1) - E({}^6A_1)]} + \frac{\langle {}^6A_1 M_s | M_q | {}^6T_1 h'' M_s \rangle \langle {}^6T_1 h' M_s | H_{SO} | {}^4\Gamma h M_{s'} \rangle}{[E({}^6T_1) - E({}^4\Gamma)]} \quad (30)$$

where M_s and $M_{s'}$ are the spin components of the $^6A_1$ and $^4\Gamma$ states; h, h', and h'' are the orbital components of the $^4\Gamma$, $^4T_1$, $^6T_1$ states; M_q is the electric dipole operator; and H_{SO} is the spin–orbit operator. Equation 30 contains the sum of two terms, the first mixes quartet ligand field character into the sextet ground state and the second mixes sextet charge-transfer character into the quartet ligand-field excited state. Since this SO coupling mechanism is also operative in monomer transitions, there must be features unique to the Fe^{III}–O–Fe^{III} unit to account for the increased intensity at low temperature. These unique characteristics are the high covalency of the Fe–oxo bond and the existence of low-energy parallel polarized oxo $\rightarrow$ Fe^{3+} charge transfer transitions, both of which contribute to the second term. The high covalency of this unit mixes metal and oxo character, thus enabling the SO coupling between LF and CT transitions to be nonzero as described in the second term of eq 30. The higher covalency also causes these CT transitions to occur at low energy which provides for more efficient mixing.

On the basis of the above analysis for SO orbit intensity for the $S = 0 \rightarrow S = 1$ transition observed at low temperature, one would expect the intensity to decrease with increasing temperature. This is not observed experimentally, in fact, the intensity increases. Thus, the effect of SO coupling on transitions from the $S = 1$ state was analyzed. Since we have found that the SO intensity of spin-forbidden bands in a ferric monomer is dependent on the M_S value,[94] vector coupling these M_S values into the dimer S_T values gives the relative SO intensity from the $S_T = 0$ and $S_T = 1$ components of the ground state. This analysis demonstrates that the $S_T = 0 \rightarrow S_T = 1$ and the $S = 1 \rightarrow S = 1$ should be the same,[27] therefore explaining the lack of decrease in intensity with increasing temperature. The fit of the intensity observed for the $^6A_1 \rightarrow {}^4T_1$ indicates that an additional exchange interaction also contributes to the $S = 1 \rightarrow S = 1$. An analysis of the selection rules for these transitions also accounts for the observed temperature-dependent polarizations.[27] The inset in Figure 30 gives the Boltzmann fit of the increase in parallel polarized intensity as a function of temperature using only the $S = 1$ state. Population of the $S_T = 1$ component of the ground state can thus accounts for this increase in intensity with the deviation from the theoretical Boltzmann plot at 300 K attributed to 7% population of the $S_T = 2$ spin state.

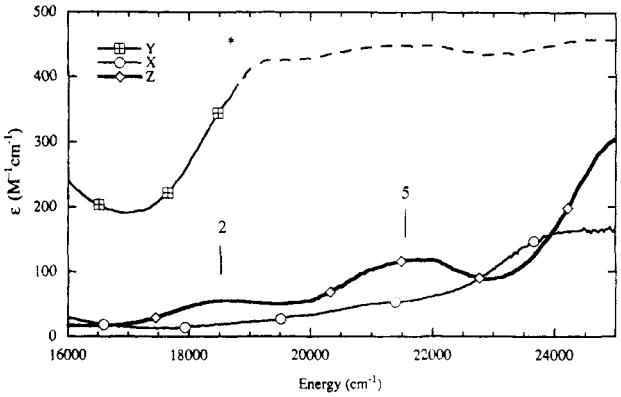

Figure 32. Single-crystal polarized absorption spectra for region II (16 000–25 000 cm^{-1}) in the tribridged structure. [The asterisk (*) denotes that the peak is intense but distorted due to stray light effects.]

In summary analysis of the two lowest energy ligand field transitions in these complexes has demonstrated that the predominant intensity gaining mechanism at low temperature in the dimer is spin–orbit coupling. The increase in intensity over the monomer is derived from the highly covalent oxo–Fe^{3+} bond in the dimer. This provides low-energy CT transitions and allows for significant mixing of Fe and oxo centers, making SO coupling of these CT transitions into the LF states more efficient. The increase in intensity observed with increasing temperature is attributed to spin-allowed triplet transitions allowed due to exchange. This exchange mechanism also accounts for the observed polarization.

Inspection of region II in Figure 26B shows at least four transitions with a marked temperature dependence. The largest band at 21 000 cm^{-1} nearly doubles in intensity upon cooling to 8 K while the other bands are eliminated at low temperature. Therefore the peak at 21 000 cm^{-1} can be assigned as a transition originating from the $S_T = 0$ component of the ground state in Figure 27 with the other transitions associated with higher total spin sublevels of the ground state. The low-temperature polarized absorption data for the tribridged structure is shown in Figure 32 which clearly demonstrates the predominant parallel polarization in this region. (Note that the Y-polarized peaks are distorted due to stray light effects from high absorption in the crystal.) There are two peaks observable in the Z-polarized spectrum at low temperature at 18 400 cm^{-1} (band 2) and 21 500 cm^{-1} (band 5). No peaks are observed in the X-polarized spectrum which gradually increases in intensity to higher energy. The variable-temperature mull spectrum of this region is shown in Figure 33. These orientationally averaged features reflect the dominant parallel polarized absorption spectrum. The prominent feature at low temperature has shifted to 20 500 cm^{-1} (band 4) from the glass (Figure 26B) but again clearly decreases in intensity with increasing temperature. Also as the temperature is raised at least three features grow in at ~17 750 (band 1), 19 100 (band 3), and 24 000 cm^{-1} (bands 6 and 7). On the basis of their temperature dependence,[27] the features at 17 750 and 19 100 cm^{-1} are assigned to transitions associated with population of the $S = 2$ and $S = 1$ components of the ground state, respectively. The feature at 24 000 cm^{-1} can also be associated with two transitions corresponding to population of $S = 1$ and $S = 2$ spin states as shown by variable-temperature

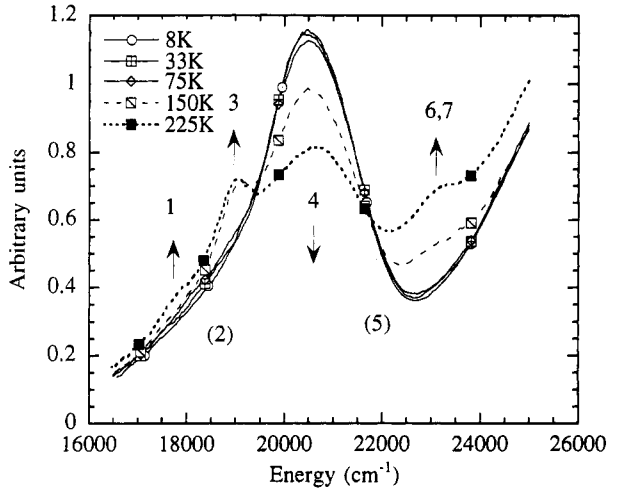

Figure 33. Variable-temperature mull spectra for region II of the tribridged structure. Arrows denote the change in intensity with increasing temperature.

MCD.[27] A summary of the polarizations and temperature dependence of the seven observed bands in this region is given in Table 2.

Resonance Raman profiles were obtained for the Fe–O–Fe symmetric stretch at 540 cm^{-1} (inset) at 77 K and room temperature and are shown in Figure 34. From the profiles, two features appear to be enhanced at low temperature, bands 2 and 4, which are the only bands present in this region at 77 K. The enhancement of band 4 decreases with increasing temperature while that of band 2 shows less of a temperature dependence. On the basis of the fact that the Fe–O–Fe symmetric stretch is enhanced by resonance from bands 2 and 4 and that these are singlet transitions, bands 2 and 4 are assigned as oxo → Fe^{3+} charge-transfer transitions. As discussed earlier, charge-transfer transitions in the dimer are spin allowed and can therefore have significant intensity for transitions originating in the $S = 0$ component of the ground state in Figure 27B. Further analysis of these bands will be presented along with the remaining oxo → Fe^{3+} CT transitions later in this section.

On the basis of their temperature dependence, bandwidths, and energy, bands 1 and 3 in Figure 33 are assigned as ligand-field (LF) transitions. The full width at half max for these transitions is ~400 cm^{-1} from Gaussian resolution of mull spectra as opposed to widths of ~2 000 cm^{-1} for band 4 or of the $^6A_1 \rightarrow {}^4T_1$ or $^6A_1 \rightarrow {}^4T_2$ transitions which all involve orbital changes in the transition. The $^6A_1 \rightarrow {}^4A_1$, ^4E ligand field transitions, predicted to be the next ligand field transitions from the Tanabe–Sugano diagram in Figure 28, are expected to be sharp since they are LF-independent spin flip transitions, $t_{2g}^3e_g^2 \rightarrow t_{2g}^3e_g^2$. Therefore bands 1 and 3 are assigned as components of the $^6A_1 \rightarrow {}^4A_1$, ^4E transitions where the striking temperature dependence can be resolved due to their sharpness. Their main source of intensity is from the exchange intensity mechanism with the corresponding dimer selection rules accounting for the parallel polarization.

This ordering of spin states with the $S = 2$ transition 1350 cm^{-1} below the $S = 1$ gives an effective excited state J^{LF} of 220 cm^{-1} with the plus sign indicative of ferromagnetism in the excited state. The ferromagnetism exhibited for the $^4A_1$, ^4E transitions implies that the orbital pathways involved in superexchange are perturbed in this ligand field excited state. The ground state J^{GS} has contributions from 25 orbital pathways involving all combinations of the five half-occupied d orbitals on each iron. This is described in eq 31:[95]

$$J^{GS} = J_{AB}(^6A_{1g}\,{}^6A_{1g}) = \frac{1}{25}\sum_{i,j} J_{A_iB_j} \qquad (31)$$

where A and B refer to the two Fe atoms and i and j to their respective d orbitals. Most of these will be negligible or ferromagnetic since they involve orbitals which do not overlap the bridging oxo or the pathway involves orthogonal p orbitals on the oxo. The overall sum leads to the observed antiferromagnetism of −120 cm^{-1} in the ground state which is due to a few strong antiferromagnetic pathways (*vide infra*). In order to probe the change in exchange coupling in the excited state, the Tanabe model[95] of exchange splitting in LF excited states has been employed. This model was specifically developed to explain the dimer spectra of spin-flip transitions which can be described in a spin Hamiltonian formalism. The equation for J^{LF} in the dimer excited state corresponding to excitation of one Fe to the $^4A_{1g}$ state (using octahedral notation) is given below: (Note that although the ^4E_g transition is predicted to be nearly degenerate with the $^4A_{1g}$, the following analysis for the ^4E_g transition cannot account for the observed ferromagnetism in the excited state. The low spectral intensity of the $^6A_{1g} \rightarrow {}^4E_g$ compared to the $^6A_{1g} \rightarrow {}^4A_{1g}$ intensity in d^5 Mn dimers has been previously noted.)[96]

$$J^{LF}(^4A_1) = J^*_{AB}(^6A_{1g}\,{}^4A_{1g}) = \frac{1}{25}\left\{\frac{25}{18}\sum_{\substack{(t)\\(t^*)}} J_{u^*} + \frac{25}{24}\sum_{\substack{(e)\\(e^*)}} J_{ee^*} + \frac{50}{36}\sum_{\substack{(t)\\(e^*)}} J_{te^*}\right\} \qquad (32)$$

where t and e refer to the ($d_{xz'}$, $d_{yz'}$, $d_{x^2-y^2}$, and (d_{z^2}, $d_{xy'}$) orbitals respectively with the prime notation referring to the Fe–O z' axis as shown in Figure 29 and the asterisk (*) referring to orbitals for the $^4A_{1g}$ state. Assuming that the individual t and e orbital pathways are the same in the ground and excited state, ratios of the weighting coefficients of specific orbital pathways in the ES and GS determine whether the contributions of these pathways are expected to increase or decrease upon excitation.[96] To account for the observed ferromagnetism in the excited state, the coefficient of an antiferromagnetic pathway needs to decrease with a concomitant increase for a ferromagnetic pathway. The results of BS-SCF-Xα-SW calculations (*vide infra*) indicate that the efficient antiferromagnetic pathways are the $d_{xz'}$-$d_{xz'}$ out of plane π pathway and the "mixed" pathways of $d_{yz'}$-d_{z^2} and d_{z^2}-$d_{yz'}$. The important ferromagnetic pathways are also assumed to involve these orbitals ($d_{xz'}$, $d_{yz'}$, d_{z^2}) which have significant oxo character, but in pathways which involve orthogonal orbitals on the oxo bridge. The ferromagnetic orbitals are therefore $d_{xz'}$-$d_{yz'}$ and d_{z^2}-$d_{xz'}$. Table 3 shows that for this $^6A_1 \rightarrow {}^4A_1$ transition in the dimer, the mixed d_{z^2}-$d_{yz'}$ and $d_{yz'}$-d_{z^2} antiferro pathway coefficients both decrease to 0.69 with an increase in the $d_{xz'}$-$d_{yz'}$ ferro pathway coefficient to 1.39 which can account for the observed ferromagnetism. Note that the $d_{xz'}$-$d_{xz'}$ antiferro pathway is less efficient for exchange coupling as it is predicted to increase upon excitation. This

Table 2. Polarizations, Energies, and Temperature Dependence of Region II Transitions

	bands						
	1	2	3	4	5	6	7
energy, cm^{-1}	17 750	18 400	19 100	20 500	21 500	22 000	23 500
polarization	*Y*	*Z*	*Y,Z*	*Y*	*Z*	*Y,Z*	*Y,Z*
temperature dependence	$S = 2$	$S = 0$	$S = 1$	$S = 0$	$S = 0$	$S = 1$	$S = 2$
assignment	$^4A_1,^4E$	oxo-CT	$^4A_1,^4E$	oxo-CT	$^4T_{2b}$	$^4T_{2b}$	$^4T_{2b}$

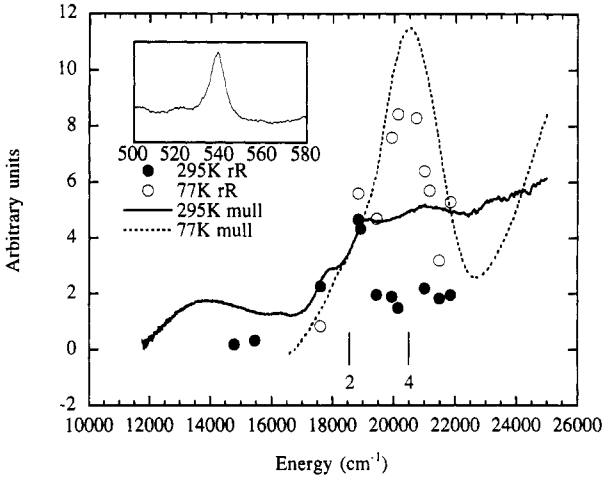

Figure 34. Room temperature and 77 K mull absorption spectra and rR profiles of the Fe–O–Fe symmetric stretch (inset) in region II.

Table 3. Ratio of ES/GS coefficients of Superexchange Pathways

	antiferro pathways			ferro pathways	
excited state	$J_{xz'-xz'}$	$J_{yz'-z^2'}$	$J_{z^2-yz'}$	$J_{xz'-z^2}$	$J_{xz'-yz'}$
$^6A_1{}^4A_1$	1.39	0.69	0.69	0.69	1.39

demonstrates the importance of these mixed $d\pi$–$d\sigma$ pathways as mediators of antiferromagnetic exchange.

Bands 6 and 7 in Figure 33 are also assigned to ligand-field transitions, the $^4T_2{}^b$ transitions, which are predicted to be next highest in energy (Figure 28) and which are also predicted to be sharp. On the basis of their temperature dependence,[27] bands 6 and 7 are assigned as triplet and quintet transitions. Their energy order gives a J^{LF} in the excited state of -495 cm^{-1}, indicating antiferromagnetism in this excited state. Since band 5 is not enhanced in the resonance Raman profile, it appears to be an $S = 0$ transition associated with the $^4T_2{}^b$ transition which gains intensity through the SO coupling mechanism described previously.

In summary, a number of states contribute to the absorption spectrum of the tribridged complex in region II. By using a combination of variable-temperature orientationally averaged and polarized absorption, VTMCD, and VT resonance Raman spectroscopies, this region has been assigned as ligand-field and oxo → Fe^{3+} CT transitions. The most intense peak at 20 500 cm^{-1} which is assigned as an oxo → Fe^{3+} CT transition is a clear example of a pure singlet transition which follows the temperature dependence expected for depopulation of the $S = 0$ component of the ground state. This demonstrates that this singlet transition is well separated from the corresponding triplet and thus shows the existence of strong excited-state antiferromagnetism, ESAF, for this charge-transfer state as shown in Figure 27B. The ligand-field transitions demonstrate the existence of both ferromagnetic and antiferromagnetic interactions in the $^4A_1$ and $^4T_2{}^b$ excited states in the dimer respectively. On the basis of an analysis of the $^4A_1$ transition, the mixed $d\pi$–$d\sigma$ pathways are experimentally determined to be particularly efficient for exchange coupling in both the ground and ligand-field excited states. Thus the absorption spectrum probes magnetic coupling in the excited state and shows which excited-state orbital pathways are dominant.

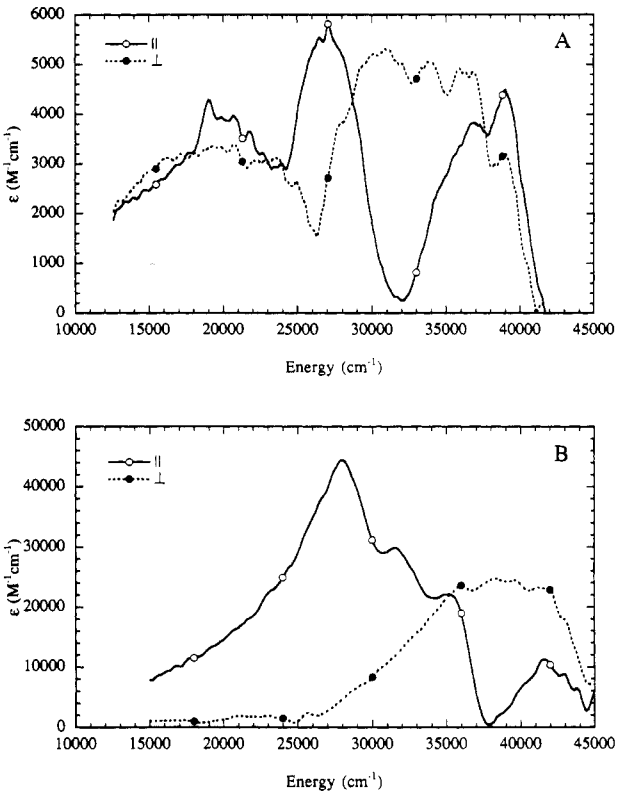

Figure 35. Polarized absorption spectra obtained from Kramers–Kronig converted reflectance data for the tribridged (A) and monobridged structures (B).

The polarized absorption spectra obtained from Kramers–Kronig transformed reflectance data for both the mono- and tribridged structures are shown in Figure 35.[27] The lowest energy major absorption in both of these complexes in region III (energy > 25 000 cm^{-1}) is parallel polarized. In the tribridged structure there are two overlapping peaks at 26 000 and 29 000 cm^{-1} and additional parallel polarized peaks between 34 000 cm^{-1} and 40 000 cm^{-1}. The spectrum of the monobridged structure has parallel polarized absorption peaks at 28 000, 31 500, and 35 000 cm^{-1} with additional parallel polarized intensity between 40 000 and 45 000 cm^{-1}. Also, for the tribridged structure, the perpendicular polarized intensity starts growing in at 30 000 cm^{-1}. The monobridged structure exhibits perpendicular intensity after 35 000 cm^{-1}. From the higher intensity of these transitions, $\epsilon > 3\,000$ M^{-1} cm^{-1}, this region should be dominated by CT transitions which are spin- and parity-allowed transitions. The oxo → Fe^{3+} charge-transfer transitions in the dimer are

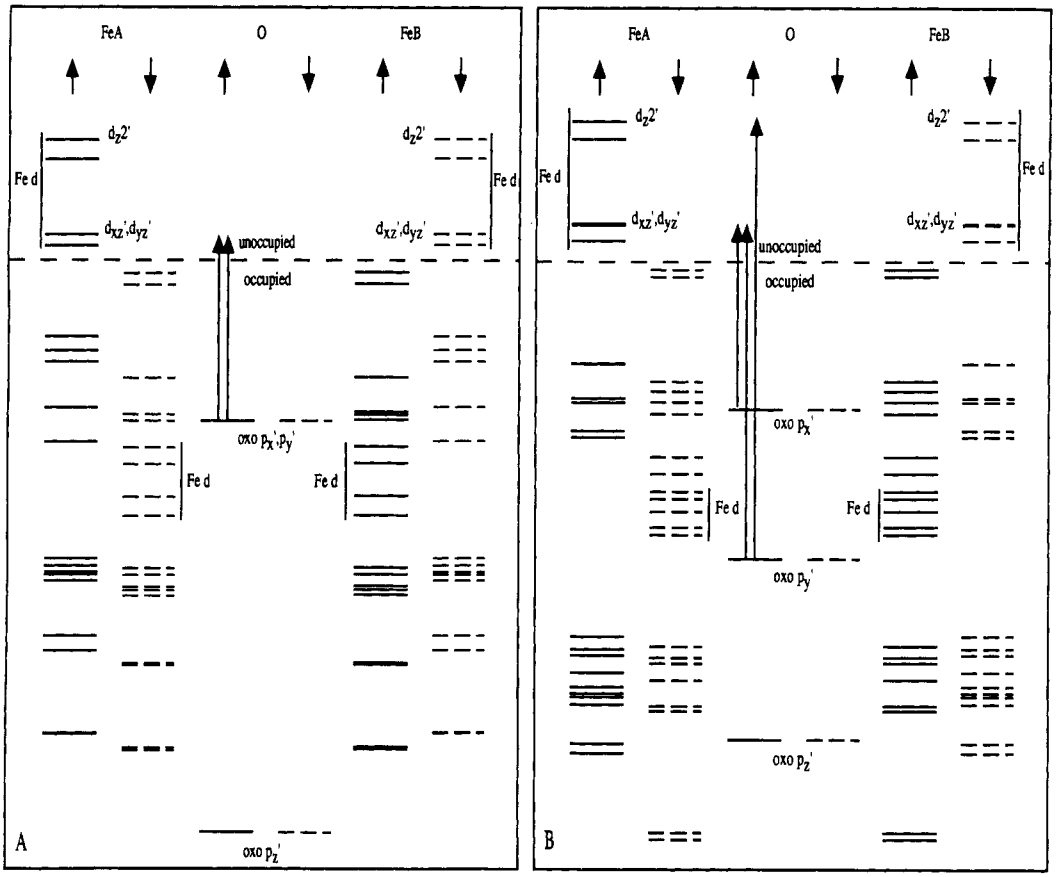

Figure 36. Energy level diagrams form BS-SCF-Xα-SW calculation on (A) a linear monobridged and (B) a tribridged (Fe–O–Fe angle = 120°) complexes.

predicted to be both parallel and in-plane perpendicular polarized. Thus on the basis of their polarizations and intensity the low-energy CT transitions can be assigned as oxo → Fe^{3+} charge-transfer transitions. BS-SCF-Xα-SW calculations aid in the analysis of these transitions.

The BS-SCF-Xα-SW energy-level diagrams for structures based on these complexes are given in Figure 36 where the calculation based on the monobridged structure has been idealized to linear. The calculations give a large monomer exchange splitting between occupied and unoccupied d orbitals with the occupied d orbitals greatly stabilized in energy and mixed with ligand orbitals.[27] Focusing on the unoccupied d orbitals, both calculations give the expected C_{4v} splitting due to the strong Fe^{3+}–oxo bond with the d_{z^2} orbital highest in energy and the $d_{xz'}$, $d_{yz'}$ orbitals nearly degenerate and higher in energy than the $d_{x^2-y^2}$ component of the t_{2g} set. In order to obtain a better description of the specific orbital interactions, contour plots of the wave functions of these d orbitals are presented. Only the Fe d_{z^2}, $d_{xz'}$ and $d_{yz'}$ orbitals are considered which are involved in bonding with the oxo. The contour plots for orbitals in the linear structure (Figure 37A,B) show the classic σ–σ and π–π orbital interactions predicted in qualitative bonding arguments.[97] Figure 37A gives the d_{z^2}-$p_{z'}$-d_{z^2} pathway which is σ antibonding and highest in energy. Figure 37B shows the $d_{yz'}$-$p_{y'}$-$d_{yz'}$ interaction which is identical to the $d_{xz'}$-$p_{x'}$-$d_{xz'}$ interaction. Assuming the delocalization of these orbitals reflects their strength as superexchange pathways in the dimer,[27] these three pathways are predicted to be similar in effectiveness in the linear dimer. The contour plots for the corresponding orbitals for tribridged

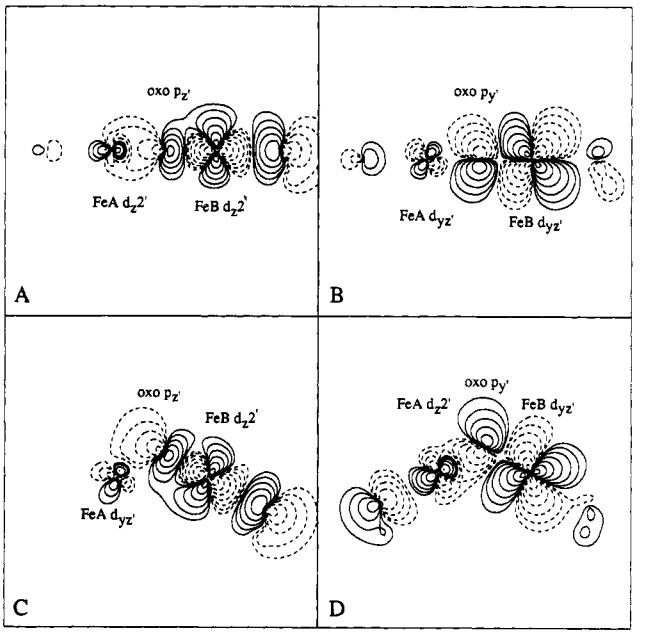

Figure 37. Contour plots of (A) the d_{z^2} orbital (linear dimer) for FeB which shows the σ–σ pathway for exchange, (B) the $d_{yz'}$ orbital (linear dimer) for FeB which shows the π–π pathway, (C) the d_{z^2} orbital (tribridged dimer) for FeB which shows the π–σ, and (D) the $d_{yz'}$ orbital (tribridged dimer) for FeB which shows the σ–π pathway.

structure show some marked differences. The contour of the FeB d_{z^2} orbital in Figure 37C shows this to be antibonding to the oxo $p_{z'}$ which also π antibonds with the $d_{yz'}$ orbital on FeA. Figure 37D gives a similar interaction with the FeB $d_{yz'}$orbital π antibonding to the oxo $p_{y'}$ which σ antibonds with the d_{z^2} of FeA. The $d_{xz'}$-$p_{x'}$ interaction is identical to that of the linear case

shown in Figure 37B. The σ and π interactions are the important pathways in the linear dimer, with the out-of-plane π interaction still present in the bent calculation but the mixed $\pi-\sigma$ and $\sigma-\pi$ pathway have become the other major pathways for coupling. A mixed pathway has also been predicted to be efficient from analysis of the GS magnetic properties of mixed-metal dimer systems.[98] From a breakdown of charges for the relevant orbitals in the BS-SCF-Xα-SW calculation[27] the $d_{yz'}$-$p_{y'}$-d_{z^2} orbital for the tribridged structure in Figure 37D is five times more delocalized than the other d orbitals which is indicative of the relative importance of the this pathway. This is confirmed by the ferromagnetism of the $^4A_{1g}$ excited state discussed above.

For comparison to the excited-state absorption data, transition-state calculations have been performed which give an ordering and estimation of the excitation energy. The predicted energies of the oxo $p_{x'} \rightarrow$ Fe d_{xz} and oxo $p_{y'} \rightarrow$ Fe $d_{yz'}$ transitions (i.e. those expected to have intensity due to good overlap) obtained for transition state calculations for the tribridged structure are 48 000 and 59 000 cm^{-1}. An even higher energy transition should occur for oxo $p_{y'} \rightarrow$ Fe d_{z^2}. These transitions are denoted by the arrows in the middle of Figure 36B. On the basis of the assignments made above, the lowest experimental CT transition energies are at 18 400 and 20 500 cm^{-1} for region II (Table 2) and the parallel-polarized peaks in region III are at 26 000 and 29 000 cm^{-1} (Figure 35). On the basis of the ordering from the BS calculation, the two peaks at 18 400 and 20 500 cm^{-1} are assigned to out of Fe–O–Fe plane $p_{x'} \rightarrow d_{xz'}$ which have the predicted parallel and in-plane perpendicular polarization. The next parallel-polarized transitions can be attributed to a combination of triplet oxo $p_{x'} \rightarrow$ Fe $d_{xz'}$ components of the oxo $p_{y'} \rightarrow$ Fe $d_{yz'}$. Since all of these transitions are at much lower energy than predicted by the BS calculations, these features can be assigned to charge-transfer transitions which have been stabilized due to ESAF. This stabilization, as described in section III, accounts for the lower energy of these transitions and demonstrates the importance of these pathways as mediators of antiferromagnetic exchange with the stabilization of the transitions originating from the in-plane $p_{y'}$ more indicative of the importance of the mixed pathway. A similar assignment is made for the transitions observed in the spectrum of the mono-bridged structure in Figure 35 with the lowest energy Y-polarized transition at 21 000 cm^{-1} assigned to the $p_{x'} \rightarrow d_{xz'}$ transition (middle of Figure 36A), and higher energy bands assigned to triplet $p_{x'} \rightarrow d_{xz'}$ transitions and components of the $p_{y'} \rightarrow d_{yz'}$ and $p_{y'} \rightarrow d_{z^2}$ transition.[27]

A rigorous assignment of the electronic absorption spectrum of the Fe^{III}–O–Fe^{III} unit has now been developed. An important feature of the assignment involves the observed temperature dependence of bands. Bands observed at low temperature and bands which decrease in intensity with increasing temperature can be assigned to spin allowed $S_T = 0 \rightarrow S_T = 0$ CT transitions or to LF transitions which gain intensity through a SO mechanism increased by the covalency of the oxo–Fe bond. The bandwidths for the $^4T_1$ and $^4T_2$ transitions do not allow for determination of excited-state splittings, but the sharp features associated with the ^4A, ^4E, and $^4T_2{}^b$ do allow determination of exchange splittings and have been used to gain experimental

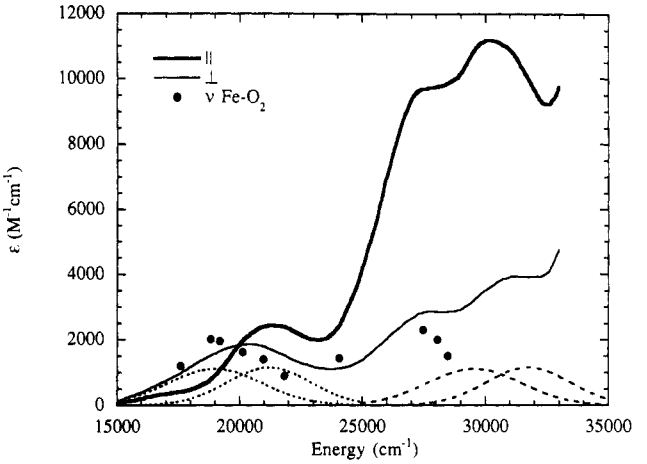

Figure 38. Polarized single-crystal absorption spectra for oxyHr and the Fe–O_2 rR profile. Dashed lines are a fit giving four $O_2^{2-} \rightarrow$ Fe(III) transitions. Points indicate rR excitation profile.

insight into orbital pathways. The low energy of the oxo $\rightarrow$ Fe CT transitions is due to ESAF and demonstrates that there are a number of very effective antiferromagnetic pathways in the Fe^{III}–O–Fe^{III} unit, and in particular the mixed $\pi-\sigma$ pathway.

B. OxyHr

Upon binding of dioxygen to the deoxy [$Fe^{II}Fe^{II}$] site, two electrons are transferred to produce an Fe^{III}–O–Fe^{III}–O_2^{2-} site.[12,99] This oxyHr site is stable and has been crystallographically described to 2.0-Å resolution.[15] The oxygen is bound to one of the Fe centers, and based on the shift in resonance Raman oxy frequencies when H_2O is replaced with D_2O, the peroxide is believed to be protonated and hydrogen bonded to the oxo bridge as shown in Figure 1B.[13,15,100] This is also supported by the decrease in the GS exchange coupling of oxyHr compared to other met derivatives (−77 vs −130 cm^{-1}).[101] Study of the Fe–OO(H) charge-transfer transitions provides insight into the iron–hydroperoxide bond and its relation to the reactivity of this protein active site.

The single-crystal polarized absorption spectrum of oxyHr is shown in Figure 38. There is a significant amount of parallel intensity which, as described above, can be associated with the Fe^{III}–O–Fe^{III} unit, but there is also perpendicular-polarized intensity not present in other derivatives. Before the crystal structure was completed, this perpendicular intensity was used to predict that the peroxide was bound to only one of the Fe atoms.[18] On the basis of the TDVC model discussed in section III, if the peroxide had bridged, one would expect significant projection onto the parallel Fe–Fe polarization which was not experimentally observed. The observed parallel to perpendicular intensity ratio of 1:10 required an O_2^{2-}–Fe–Fe angle of 90 ± 13° and ruled out any bridging geometry. This was an early application of the use of charge-transfer transitions in dimers to understand basic geometric and electronic structure.

For a single peroxide bound to a high-spin ferric monomer one would expect to see two CT transitions, one from the peroxo $\pi_v^* \rightarrow d\pi$, and one from the $\pi_\sigma^* \rightarrow d_{x^2-y^2}$ with the π_σ^* much more intense due to overlap considerations (Figure 39, left). This is not observed in the spectrum of oxyHr.[17] Aided by similarities in

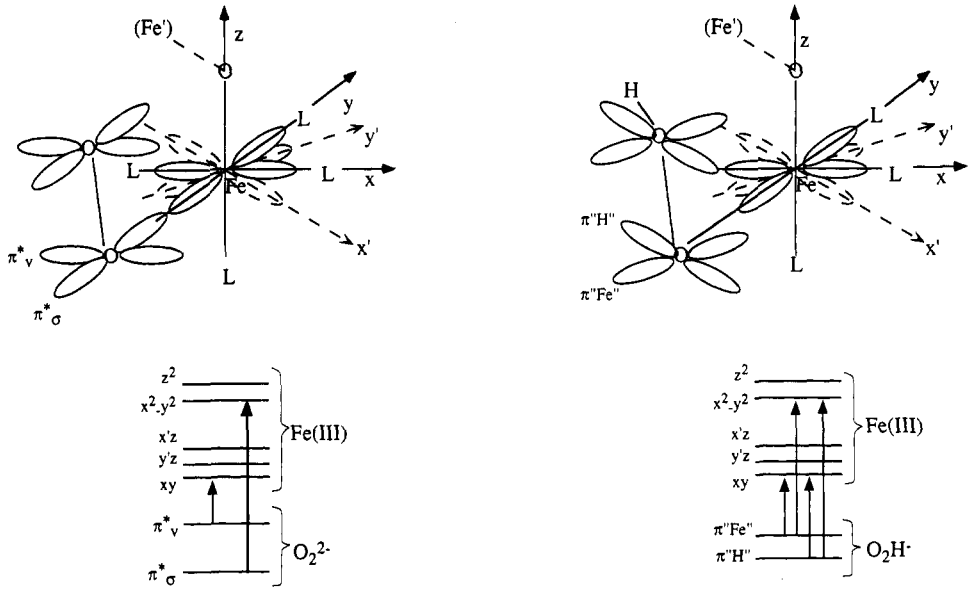

Figure 39. Qualitative bonding description of O_2^{2-}–Fe(III) (left) and HO_2^-–Fe(III) (right). Note that for O_2^{2-} only two transitions are predicted, one more intense than the other, while for HO_2^- there should be four of equal intensity.

the metN$_3^-$ spectrum, the oxyHr perpendicular intensity is assigned as $O_2^{2-} \rightarrow$ Fe charge-transfer transitions, but the charge-transfer spectrum is fit instead with four bands (19 100, 21 100, 29 650, 31 800 cm^{-1}) of approximately the same intensity with an intraset splitting of 2 000 cm^{-1} and interset splitting of 10 500 cm^{-1}. (See Gaussians in Figure 38.[17]) The Raman excitation profile of the Fe–O_2 stretch[100] shown in Figure 38 peaks with the lower energy feature at 19 100 cm^{-1}. This feature is also prominent in the CD spectrum of oxyHr.[17] The profile in the higher energy region appears to peak before the assigned transitions. To explain these observed four transitions of similar intensity, a qualitative bonding model was developed. The peroxide was assumed to interact mainly with the $d_{xy'}$ and $d_{x^2-y^2}$ orbitals of the iron by π and σ interactions, respectively (Figure 39). The interset splitting of 10 500 cm^{-1} was assumed to be due to 10Dq or the $d_{xy'}$-$d_{x^2-y^2}$ splitting. The intraset splitting was attributed to the splitting between the peroxide π^* orbitals. Protonation of the peroxide and rotation of the HO_2^- proton relative to the Fe–OO mixes π^*_v and π^*_σ which would give bands of equal intensity as described in the Figure 39, right. Also since the lower energy transition appears to be the transition that is enhanced in the Raman profile, the more stabilized π^* was assumed to be more involved in bonding to the proton (π^* "H") instead of the iron (π^* "Fe").

To test these predictions, SCF-Xα-SW calculations have been performed on hydroperoxide bound to a high-spin ferric monomer. The structure calculated was similar to that of metHr with the short Fe–O bond of 1.8 Å but now with a proton replacing the second Fe(III) for simplification. The hydroperoxo is placed so that the proton can undergo hydrogen bonding with the "hydroxo" oxygen. Three calculations are considered which differ in the orientation of the proton of the hydroperoxide. The Fe–OOH dihedral angle used for these calculations are 0°, 60°, and 90°. The unoccupied spin-down d orbital and the peroxide orbital energies are given in Figure 40. In all three cases the splitting between the $d_{xy'}$ and $d_{x^2-y^2}$ orbitals is ~10 400 cm^{-1} which is close to the expected 10Dq. For the Θ = 0° calculation, the most stabilized π^* orbital is the π^*_σ, with the π^*_v orbital 11 900 cm^{-1} above it in energy. The contour plots of these orbitals are shown in Figure 41, parts A and B. Figure 41A shows the strong Fe–OO σ bond with the "$d_{x^2-y^2}$" orbital as expected and Figure 41B gives the π interaction with the "d_{xy}" orbital. This latter interaction does not contribute to bonding in Cu systems which have only one unpaired electron on the Cu. Upon changing the dihedral angle to 60°, the splitting between the π orbitals decreases to 7850 cm^{-1} with the wave functions becoming mixed in character. This is clearly illustrated in the contour plots of these orbitals which give two mainly σ interactions as opposed to the expected σ and π interactions. For a dihedral angle 90°, the orbitals become less mixed and again look more like pure σ and π interactions as shown in Figure 18, parts E and F; however, note that in Figure 40 the π^*_v has now been stabilized below that of the π^*_σ by 4 637 cm^{-1}, thus switching their energetic ordering. In summary, protonation and orientation of the proton can mix the π^* orbitals as it rotates between a dihedral angle of 0° and 90°. It also greatly effects the splitting between these π^* orbitals and switches π^*_σ and π^*_v energy ordering on going from 0° to 90°. Thus protonation of the peroxide greatly effects the bonding in this complex and the effect of this interaction is now being studied in detail in order to describe electronic contributions to O_2 bonding and activation.[102]

VII. Electronic Structure Contributions to Reactivity

Charge transfer and related spectral data provide direct probes of peroxide–metal bonds. In hemocyanin, the intense O_2^{2-} π^*_σ charge-transfer transition reflects an extremely strong σ donor interaction relative to an end-on bound peroxide, which results from the fact that the side-on bridging peroxide in Figure 1A has two σ donor interactions with each copper in the dimer. This is complemented by the π acceptor interaction present only in the side-on bridged structure. Together these provide a very strong peroxide–binuclear cupric bonding interaction which stabilizes the oxyhemocyanin

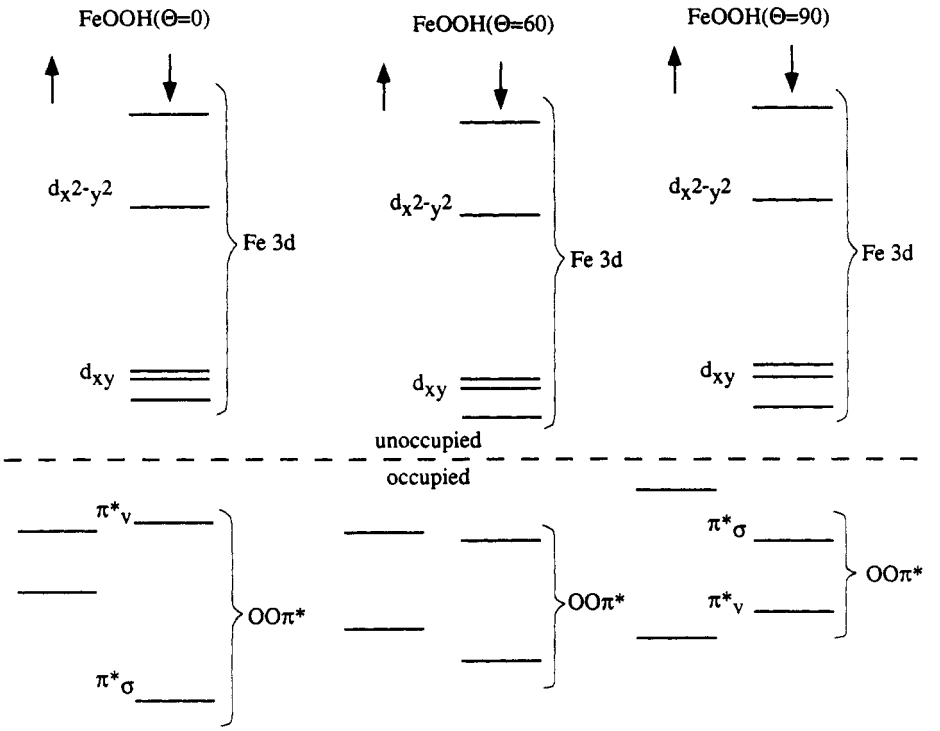

Figure 40. Energy-level diagrams from calculations on Fe(III)-O_2H^- monomers. Θ is the FeOOH dihedral angle.

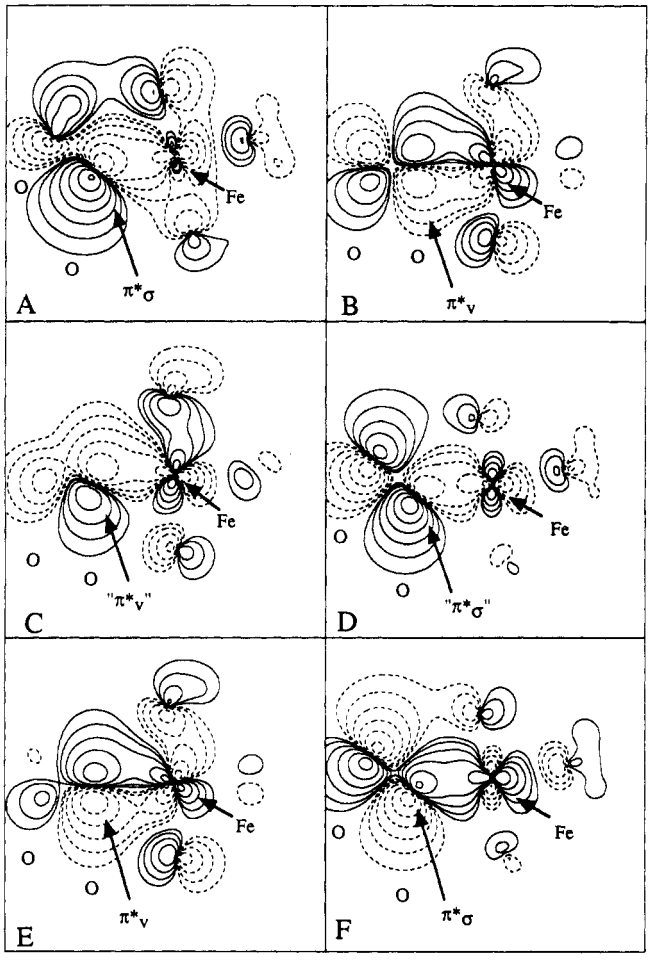

Figure 41. Contour plots of the π^*_σ and π^*_v orbitals for Θ = 0, 60, 90. Note that plots A, D, and F are in the Fe-OO plane and B, C, and E are along the Fe-peroxo bond but perpendicular to the Fe-OO plane.

site from the loss of peroxide which would generate the met derivative which is inactive to further O_2 binding.

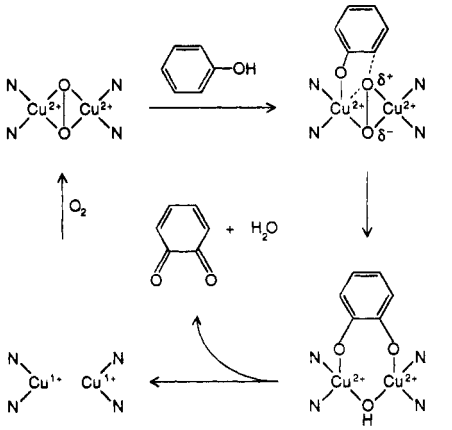

Figure 42. Proposed mechanism for oxygen activation in tyrosinase.

Spectral studies on oxytyrosinase have shown that the active site in this binuclear copper enzyme is extremely similar to hemocyanin and has the same oxy intermediate structure.[103] The electronic structure described in section II is thus also appropriate for this intermediate and can make an important contribution to the activation of dioxygen for the hydroxylation of phenolic substrates by this enzyme (Figure 42). The strong σ-donor interaction leads to a less negative peroxide, while the π acceptor interaction shifts electron density into the σ* orbital on peroxide which greatly weakens the O-O bond and activates it for cleavage. A major difference we have found between hemocyanin and tyrosinase is that the active site in tyrosinase is highly accessible to the substrate which coordinates directly to the copper center.[104] This would shift electron density into the LUMO in Figure 10A which is antibonding with respect to the O-O and Cu-O bonds and thus would initiate oxygen transfer to the ortho position of the phenol ring. For the multicopper oxidases we have shown[75] that a different peroxide level intermediate is present on the basis of strikingly different charge transfer spectral features relative to

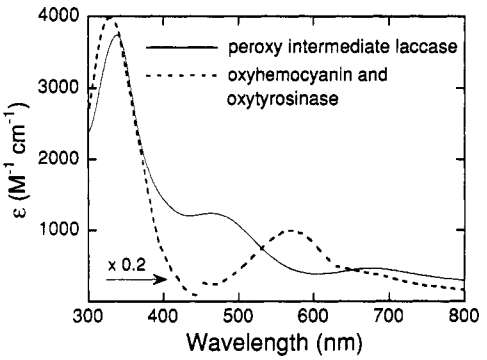

Figure 43. Comparison of the absorption spectra for the peroxy intermediate in laccase with that of oxyhemocyanin and oxytyrosinase. Note that the 350-nm band of oxyHc has been scaled down by a factor of 5.

oxyhemocyanin and oxytyrosinase (Figure 43). This difference in electronic and geometric structure is now being studied in detail as it appears to promote the further irreversible reduction of dioxygen to water at a trinuclear copper cluster site in the multicopper oxidases.

For oxyhemerythrin, the charge-transfer spectrum is quite different from the low-energy weak π, high-energy intense σ-charge-transfer transitions expected for peroxide end-on bound to a single Fe(III) center. The π- and σ-charge-transfer intensities appear to be mixed which derives from the additional protonation of the peroxide and its interaction with the oxo bridge. This protonation significantly changes the nature of the peroxide-bonding interaction with the Fe(III) making this ligand less likely to donate electron density back to the iron center. The hydrogen bond to the oxo bridge will further stabilize the oxy site from loss of hydrogen peroxide thus preventing the irreversible production of met hemerythrin. As emphasized in section VI the oxo bridge dominates the electronic structure of the binuclear ferric site in oxyhemerythrin. It is important to note that for the binuclear non-heme iron site in methane monooxygenase it now appears that this bridge is hydroxide when the site is at the binuclear ferric (met) level.[105,106] This major electronic structure difference can make a significant contribution to the reactivity of the methane monooxygenase site in activating dioxygen, apparently through a higher valent oxo–ferryl species.[107] Further spectral studies on these structure/function correlations are now underway.

Acknowledgments. E.I.S. wishes to express his sincere appreciation to all of his students and collaborators who are listed as co-authors in the literature cited for their commitment and major contributions to this science. This research has been supported by the NIH (DK3145) and the NSF (MCB-3916768). F.T. acknowledges DFG for a postdoctoral fellowship.

VIII. Abbreviations

BS-SCF-Xα-SW	broken symmetry–self-consistent field–Xα–scattered wave
CD	circular dichroism
CI	configuration interaction
CT	charge transfer
DCT	double charge transfer
en	ethylenediamine
EPR	electron paramagnetic resonance
ESAF	excited-state antiferromagnetism
EXAFS	extended X-ray absorption fine structure
GS	ground state
GSAF	ground-state antiferromagnetism
Hc	hemocyanin
Hr	hemerythrin
HEDTA	*N*-(hydroxyethyl)ethylenediaminetriacetic acid
HOMO	highest occupied molecular orbital
LF	ligand field
LMCT	ligand to metal charge transfer
LUMO	lowest unoccupied molecular orbital
Me_3TACN	*N,N′,N″*-trimethyl-1,4,7-triazocyclononane
MMCT	metal to metal charge transfer
rR	resonance Raman
SO	spin orbit
SPE	simultaneous pair excitation
TDVC	transition dipole vector coupling
UV/vis	ultraviolet/visible
VTMCD	variable-temperature magnetic circular dichroism

References

(1) Makinen, M. W.; Churg, A. K. In *Iron Porphyrins*; Lever, A. B. P., Gray, H. B., Eds.; Addison-Wesley Publishing Company: Reading, MA, 1983; Vol. 1, pp 141–235.
(2) Lever, A. B. P.; Gray, H. B. *Acc. Chem. Res.* **1978**, *11*, 348–355.
(3) Solomon, E. I.; Baldwin, M. J.; Lowery, M. D. *Chem. Rev.* **1992**, *92*, 521–542.
(4) Freedman, T. B.; Loehr, J. S.; Loehr, T. M. *J. Am. Chem. Soc.* **1976**, *98*, 2809–2815.
(5) Larrabee, J. A.; Spiro, T. G. *J. Am. Chem. Soc.* **1980**, *102*, 4217–4223.
(6) Eickman, N. C.; Solomon, E. I.; Larrabee, J. A.; Spiro, T. G.; Lerch, K. *J. Am. Chem. Soc.* **1978**, *100*, 6529–6531.
(7) Woolery, G. L.; Powers, L.; Winkler, M.; Solomon, E. I.; Spiro, T. G. *J. Am. Chem. Soc.* **1984**, *106*, 86–92.
(8) Co, M. S.; Hodgson, K. O. *J. Am. Chem. Soc.* **1981**, *103*, 3200–3201.
(9) Co, M. S.; Hodgson, K. O.; Eccles, T. K.; Lontie, R. *J. Am. Chem. Soc.* **1981**, *103*, 984–986.
(10) Ton-That, H.; Magnus, K. *J. Inorg. Biochem.* **1993**, *51*, 65.
(11) Kitajima, N.; Fujisawa, K.; Moro-oka, Y.; Toriumi, K. *J. Am. Chem. Soc.* **1989**, *111*, 8975–8976.
(12) Solomon, E. I.; Zhang, Y. *Acc. Chem. Res.* **1992**, *25*, 343–352.
(13) Shiemke, A. K.; Loehr, T. M.; Sanders-Loehr, J. *J. Am. Chem. Soc.* **1986**, *108*, 2437–2443.
(14) Schugar, H. J.; Rossman, G. R.; Barraclough, C. G.; Gray, H. B. *J. Am. Chem. Soc.* **1972**, *94*, 2683–2690.
(15) Holmes, M. A.; Trong, I. L.; Turley, S.; Sieker, L. C.; Stenkamp, R. E. *J. Mol. Biol.* **1991**, *218*, 583–593.
(16) Garbett, K.; Darnall, D. W.; Klotz, I. M.; Williams, R. J. P. *Arch. Biochem. Biophys.* **1969**, *135*, 419–434.
(17) Reem, R. C.; McCormick, J. M.; Richardson, D. E.; Devlin, F. J.; Stephens, P. J.; Musselman, R. L.; Solomon, E. I. *J. Am. Chem. Soc.* **1989**, *111*, 4688.
(18) Gay, R. R.; Solomon, E. I. *J. Am. Chem. Soc.* **1978**, *100*, 1972–1973.
(19) Larrabee, J. A.; Baumann, T. F.; Chisdes, S. J.; Lyons, T. J. *Inorg. Chem.* **1992**, *31*, 3630–3635.
(20) Zhang, J.-H.; Kurtz, D. M. *Proc. Natl. Acad. Sci. U.S.A.* **1992**, *89*, 7065–7069.
(21) Niederhoffer, E. C.; Timmons, J. H.; Martell, A. E. *Chem. Rev.* **1984**, *84*, 137.
(22) Solomon, E. I.; Lowery, M. D. *Science* **1993**, *259*, 1575–1581.
(23) Slater, J. C. *The Calculation of Molecular Orbitals*; John Wiley & Sons: New York, 1979, pp 104.
(24) Noodleman, L. *J. Chem. Phys.* **1981**, *74*, 5737–5743.
(25) Tuczek, F.; Solomon, E. I. *Inorg. Chem.* **1993**, *32*, 2850–2862.
(26) Tuczek, F.; Solomon, E. I. *Inorg. Chem.* **1992**, *31*, 944–953.
(27) Brown, C. A.; Musselman, R. L.; Solomon, E. I. Submitted to *J. Am. Chem. Soc.*, 1994.
(28) Solomon, E. I.; Lowery, M. D.; LaCroix, L. B.; Root, D. E. *Methods Enzymol.* **1993**, *226*, Part C, 1.
(29) Karlin, K. D.; Ghosh, P.; Cruse, R. W.; Farooq, A.; Gultneh, Y.; Jacobson, R. R.; Blackburn, N. J.; Strange, R. W.; Zubieta, J. *J. Am. Chem. Soc.* **1988**, *110*, 6769–6780.
(30) Kitajima, N.; Fujisawa, K.; Fujimoto, C.; Moro-oka, Y.; Hashimoto, S.; Kitagawa, T.; Toriumi, K.; Tatsumi, K.; Nakamura, A. *J. Am. Chem. Soc.* **1992**, *114*, 1277–1291.
(31) Karlin, K. D.; Cruse, R. W.; Gultneh, Y.; Farooq, A.; Hayes, J. C.; Zubieta, J. *J. Am. Chem. Soc.* **1987**, *109*, 2668–2679.

(32) Pate, J. E.; Cruse, R. W.; Karlin, K. D.; Solomon, E. I. *J. Am. Chem. Soc.* **1987**, *109*, 2624–2630.
(33) Mulliken, R. S. *J. Chem. Phys.* **1939**, *7*, 20–34.
(34) Blackburn, N. J.; Strange, R. W.; Cruse, R. W.; Karlin, K. D. *J. Am. Chem. Soc.* **1987**, *109*, 1235–1237.
(35) Ross, P. K.; Solomon, E. I. *J. Am. Chem. Soc.* **1991**, *113*, 3246–3259.
(36) Jacobson, R. R.; Tyeklar, Z.; Farooq, A.; Karlin, K. D.; Liu, S.; Zubieta, J. *J. Am. Chem. Soc.* **1988**, *110*, 3690–3692.
(37) Baldwin, M. J.; Ross, P. K.; Pate, J. E.; Tyeklar, Z.; Karlin, K. D.; Solomon, E. I. *J. Am. Chem. Soc.* **1991**, *113*, 8671–8679.
(38) Hay, P. J.; Thibeault, J. C.; Hoffman, R. J. *J. Am. Chem. Soc.* **1975**, *97*, 4884–4899.
(39) Eickman, N. C.; Himmelwright, R. S.; Solomon, E. I. *Proc. Natl. Acad. Sci. U.S.A.* **1979**, *76*, 2094–2098.
(40) Desjardins, S. R.; Wilcox, D. E.; Musselman, R. L.; Solomon, E. I. *Inorg. Chem.* **1987**, *26*, 288–300.
(41) Ross, P. K.; Allendorf, M. D.; Solomon, E. I. *J. Am. Chem. Soc.* **1989**, *111*, 4009–4021.
(42) Pate, J. E.; Ross, P. K.; Thamann, T. J.; Reed, C. A.; Karlin, K. D.; Sorrell, T. N.; Solomon, E. I. *J. Am. Chem. Soc.* **1989**, *111*, 5198–5209.
(43) Baldwin, M. J.; Root, D. E.; Pate, J. E.; Fujisawa, K.; Kitajima, N.; Solomon, E. I. *J. Am. Chem. Soc.* **1992**, *114*, 10421–10431.
(44) Larrabee, J. A.; Spiro, T. G.; Ferris, N. S.; Woodruff, W. H.; Maltese, W. A.; Kerr, M. S. *J. Am. Chem. Soc.* **1977**, *99*, 1979–1980.
(45) Ros, P.; Schuit, G. C. A. *Theor. Chim. Acta* **1966**, *4*, 1–12.
(46) van der Avoird, A.; Ros, P. *Theor. Chim. Acta* **1966**, *4*, 1321.
(47) Solomon, E. I. *Comments Inorg. Chem.* **1984**, *3*, 225–320.
(48) Clark, R. J. H.; Stewart, B. *Struct. Bonding* **1979**, *36*, 1–80.
(49) Tanabe, Y.; Aoyagi, K. In *Excitons*; Rashba, E. I., Sturge, M. D., Eds.; North-Holland: Amsterdam, The Netherlands, 1982.
(50) Craig, D. P.; Walmsley, S. H. *Excitons in Molecular Crystals*; W. A. Benjamin, Inc.: New York, 1968.
(51) Kasha, M.; Rawls, H. R.; El-Bayoumi, M. A. *Pure Appl. Chem.* **1965**, *11*, 371–392.
(52) El Sayed, M. A.; Robinson, G. W. *Mol. Phys.* **1961**, *4*, 273–286.
(53) Hansen, A. E.; Ballhausen, C. J. *Trans. Faraday Soc.* **1965**, *61*, 631–639.
(54) Tuczek, F.; Solomon, E. I. *J. Am. Chem. Soc.* **1993**, submitted for publication.
(55) Solomon, E. I. In *Metal Clusters in Proteins*, 372 ed.; Que, L., Jr., Ed.; American Chemical Society: Washington D.C., 1988.
(56) Didziulis, S. V.; Cohen, S. L.; Gewirth, A. A.; Solomon, E. I. *J. Am. Chem. Soc.* **1988**, *110*, 250–268.
(57) Jones, R. D.; Summerville, D. A.; Basolo, F. *Chem. Rev.* **1979**, *79*, 139–179.
(58) Pickens, S. R.; Martell, A. E. *Inorg. Chem.* **1980**, *19*, 15.
(59) McLendon, G.; Pickens, S. R.; Martell, A. E. *Inorg. Chem.* **1977**, *16*, 1551.
(60) Dexter, D. D.; Sutherby, C. N.; Grieb, M. W.; Beaumont, R. C. *Inorg. Chem.* **1984**, *86*, 19.
(61) Sasaki, Y.; Fujita, J.; Salto, K. *Bull. Chem. Soc. Jpn.* **1969**, *42*, 146.
(62) Sasaki, Y.; Fujita, J.; Saito, K. *Bull. Chem. Soc. Jpn.* **1970**, *43*, 3462.
(63) Sasaki, Y.; Fujita, J.; Saito, K. *Bull. Chem. Soc. Jpn.* **1971**, *44*, 3373.
(64) Bosnich, B.; Poon, C. K.; Tobe, M. L. *Inorg. Chem.* **1966**, *5*, 1514.
(65) Lever, A. P. B. *Inorganic Electronic Spectroscopy*; Elsevier: New York, 1984.
(66) Clark, R. J. H.; Mitchell, P. D. J. *Journal of Molecular Spectroscopy* **1974**, *51*, 458–474.
(67) Tang, J.; Albrecht, A. C. In *Raman Spectroscopy*; Szymanski, H., Ed.; Plenum: New York, 1970; Vol. 2, pp 33.
(68) Miskowski, V. *Comments Inorg. Chem.* **1987**, *6*, 193.
(69) Mäcke, H. R.; Williams, A. F. In *Photoinduced Electron Transfer*; Fox, M. A., Chanon, M., Eds.; Elsevier: Amsterdam, 1988; Vol. D, pp 28–46.
(70) Martell, A. E. *Acc. Chem. Res.* **1982**, *15*, 155–162.
(71) Gubelmann, M. H.; Williams, A. F. *Struct. Bonding* **1983**, *55*,
(72) Hoffman, A. B.; Taube, H. *Inorg. Chem.* **1968**, *7*, 1971.
(73) Davies, R.; Sykes, A. G. *J. Chem. Soc. A* **1968**, 2840.
(74) Davies, R.; Stevenson, M. B.; Sykes, A. G. *J. Chem. Soc. A* **1970**,
(75) Cole, J. L.; Ballou, D. P.; Solomon, E. I. *J. Am. Chem. Soc.* **1991**, *113*, 8544–8546.
(76) Sanders-Loehr, J. In *Iron Carriers and Iron Proteins*; Loehr, T. M., Ed.; VCH Press: New York, 1989; pp 373–466.
(77) Vincent, J. B.; Olivier-Lilley, G. L.; Averill, B. A. *Chem. Rev.* **1990**, *90*, 1447–1467.
(78) Que, L., Jr.; True, A. E. In *Prog. Inorg. Chem.*; Lippard, S. J., Ed.; John Wiley & Sons: New York, 1990; Vol. 38, pp 97–200.
(79) Kurtz, D. M. *Chem. Rev.* **1990**, *90*, 585–606.
(80) Stenkamp, R. E.; Sieker, L. C.; Jensen, L. H.; McCallum, J. D.; Sanders-Loehr, J. *Proc. Natl. Acad. Sci. U.S.A.* **1985**, *82*, 713–716.
(81) Brennan, B. A.; Qiuhao, C.; Juarez-Garcia, C.; True, A. E.; O'Connor, C. J.; Que, L. *Inorg. Chem.* **1991**, *30*, 1937–1943.
(82) Kitajima, N.; Hideno, F.; Moro-oka, Y.; Mizutani, Y.; Kitagawa, T. *J. Am. Chem. Soc.* **1990**, *112*, 6402–6403.
(83) Holt, S.; Dingle, R. *Acta Chem. Scand.* **1968**, *22*, 1091–1096.
(84) Beer, R. H.; Tolman, W. B.; Bott, S. G.; Lippard, S. J. *Inorg. Chem.* **1991**, *30*, 2082–2092.
(85) Norman, R. E.; Holz, R. C.; Ménage, S.; O'Connor, C. J.; Zhang, J. H.; Que, L., Jr. *Inorg. Chem.* **1990**, *29*, 4629–4637.
(86) Hartman, J. R.; Rardin, R. L.; Chaudhuri, P.; Pohl, K.; Wieghardt, K.; Nuber, B.; Weiss, J.; Papaefthymiou, G. C.; Frankel, R. B.; Lippard, S. J. *J. Am. Chem. Soc.* **1987**, *109*, 7387–7396.
(87) Lippard, S. J.; Schugar, H.; Walling, C. *Inorg. Chem.* **1967**, *6*, 1825–1831.
(88) Hirst, L. L.; Ray, T. *Proc. R. Soc. Lond. A* **1982**, *384*, 191–203.
(89) Tanabe, Y.; Sugano, S. *J. Phys. Soc. Jpn.* **1954**, *9*, 753–766.
(90) Briat, B.; Russel, M. F.; Rivoal, J. C.; Chapelle, J. P.; Kahn, O. *Mol. Phys.* **1977**, *34*, 1357–1389.
(91) McCarthy, P. J.; Güdel, H. U. *Coord. Chem. Rev.* **1988**, *88*, 69–131.
(92) Vala, M.; Rivoal, J. C.; Badoz, J. *Mol. Phys.* **1975**, *30*, 1325–1344.
(93) Gebhard, M. S.; Deaton, J. C.; Koch, S. A.; Millar, M.; Solomon, E. I. *J. Am. Chem. Soc.* **1990**, *112*, 2217–2231.
(94) Deaton, J. C.; Gebhard, M. S.; Solomon, E. I. *Inorg. Chem.* **1989**, *28*, 877–889.
(95) Ferguson, J.; Guggenheim, H. J.; Tanabe, Y. *J. Phys. Soc. Jpn.* **1966**, *21*, 692–704.
(96) Ferguson, J.; Güdel, H. U.; Krausz, E. R.; Guggenheim, H. J. *Mol. Phys.* **1974**, *28*, 893–904.
(97) Dunitz, J. D.; Orgel, L. E. *J. Chem. Soc.* **1959**, 2594–2596.
(98) Hotzelmann, R.; Wieghardt, K.; Flörke, U.; Haupt, H.-J.; Weatherburn, D. C.; Bonvoisin, J.; Blondin, G.; Girerd, J.-J. *J. Am. Chem. Soc.* **1992**, *114*, 1681–1696.
(99) Reem, R. C.; Solomon, E. I. *J. Am. Chem. Soc.* **1987**, *109*, 1216–1226.
(100) Shiemke, A. K.; Loehr, T. M.; Sanders-Loehr, J. *J. Am. Chem. Soc.* **1984**, *106*, 4951–4956.
(101) Dawson, J. W.; Gray, H. B.; Hoenig, H. E.; Rossman, G. R.; Schredder, J. M.; Wang, R.-H. *Biochemistry* **1972**, *11*, 461.
(102) Brown, C. A.; Solomon, E. I. Unpublished results, 1993.
(103) Himmelwright, R. S.; Eickman, N. C.; LuBien, C. D.; Lerch, K.; Solomon, E. I. *J. Am. Chem. Soc.* **1980**, *102*, 7339–7344.
(104) Wilcox, D. E.; Porras, A. G.; Hwang, Y. T.; Lerch, K.; Winkler, M. E.; Solomon, E. I. *J. Am. Chem. Soc.* **1985**, *107*, 4015–4027.
(105) DeRose, V. J.; Liu, K. E.; Kurtz, D. M.; Hoffman, B. M.; Lippard, S. J. *J. Am. Chem. Soc.* **1993**, *115*, 6440–6441.
(106) Thomann, H.; Bernardo, M.; McCormick, J. M.; Pulver, S.; Anderson, K. K.; Lipscomb, J. D.; Solomon, E. I. *J. Am. Chem. Soc.* **1993**, *115*, 8881–8882.
(107) Lee, S.; Fox, B. G.; Froland, W. A.; Lipscomb, J. D.; Münck, E. *J. Am. Chem. Soc.* **1993**, *115*, 6450–6451.